

EVALUATION OF GROUNDWATER RECHARGE IN THE SALT BASIN, NM/TX

by

Beth Ann Michelle Eberle

Submitted in Partial Fulfillment
of the Requirements for the Degree of
Master of Science in Hydrology



New Mexico Institute of Mining and Technology
Socorro, New Mexico
August, 2021

ACKNOWLEDGMENTS

I want to thank my advisor, Dr. Daniel Cadol, for guiding me through this project. I truly appreciate his calmness when I faced unexpected obstacles and his ability to break down overwhelming tasks into doable pieces.

Thanks to my committee members, Dr. Fred Phillips and Dr. Alex Rinehart, for helping me through all of the chemistry and reformatting, as well as serving on my committee. They both pushed me to explore a realm of possibilities that I never thought of.

A special thanks to Stacy Timmons and the rest of the Salt Basin project team from the New Mexico Bureau of Geology and Mineral Resources, New Mexico Institute of Mining and Technology, United States Geologic Survey, and S.S. Papadopoulos & Associates, Inc: Talon Newton (NMBGMR), Marissa Fichera (NMBGMR), Kitty Pokorny (NMBGMR), Laila Sturgis (NMBGMR), Shari Kelley (NMBGMR), Mark Person (NMT), Andre Ritchie (USGS), Jeff Pepin (USGS), Gilbert Barth (P&A), and Jessica Rogers (P&A).

My thanks to my project partner, Elizabeth Evenocheck, who was working on the groundwater model component of the Salt Basin project. Her encouragement helped me greatly throughout the project and graduate experiences.

And lastly, I want to thank my family, friends, and kittens. Their constant support has been phenomenal. I wouldn't have made it to the end if they weren't there making early draft edits, making me tea, and making me smile.

This thesis was typeset with \LaTeX ¹ by the author.

¹The \LaTeX document preparation system was developed by Leslie Lamport as a special version of Donald Knuth's $\text{T}_{\text{E}}\text{X}$ program for computer typesetting. $\text{T}_{\text{E}}\text{X}$ is a trademark of the American Mathematical Society. The \LaTeX macro package for the New Mexico Institute of Mining and Technology thesis format was written by John W. Shipman.

ABSTRACT

The Salt Basin, NM/TX is a semiarid, hydrologically closed basin that relies on potable groundwater to provide for domestic and agricultural needs. This groundwater source has been the basis of eleven previous hydrological studies, each of which estimated a groundwater recharge rate. These previous recharge estimates range from 6,000 to 240,000 acre-feet per year (7,000,000 to 300,000,000 m³/yr.). This wide range of recharge estimates makes it difficult to implement a sustainable water-budget plan for the basin. Therefore, the U.S. Bureau of Reclamation has funded this study and [1] in order to constrain the recharge estimates and create a more complete groundwater flow model, respectively.

This study utilized hydrochemical analyses, the chloride-mass-balance approach, and a New Mexico-specific soil-water-balance model, PyRANA. Hydrochemical analyses supported previous studies by identifying dedolomitization trends in the New Mexico portion of the Salt Basin. However, the Texas portion of the Salt Basin was found to be geologically and hydrologically more complex. Carbonate facies continue to be the primary aquifer units in the south, but there is also some influence of brines from the Salt Flats in the central basin and extensively fractured facies in the southwest basin. The brines mix with waters that otherwise follow a dedolomitization trend. Fractured carbonates create a two-water mixing system. Young, fresh waters recharge through the fractures and old, high-total-dissolved-solid waters reside in the carbonate matrix. Groundwater sampled from the 1980's showed evidence of mixing with water containing fallout from the 1950's and 1960's atmospheric nuclear weapons tests. Corrected radiocarbon ages support this mixing trend. The Fontes and Garnier method was used to make radiocarbon corrections, with limited certainty. An additional mixing trend between the young and old groundwaters of the southwestern Salt Basin was also explored to make radiocarbon corrections exclusively for the southwestern points. Using the mixing correction, the corrected groundwater ages ranged from 900 years to 26,000 years. Neither radiocarbon correction method resulted in a flow path of increasing age that could be used to get a groundwater flow velocity.

The chloride-mass-balance method was supplemented with chloride-to-bromide ratio measurements to differentiate atmospheric chloride from chloride derived from mineral dissolution in deep basin brines. A mixing curve correction factor was applied to the chloride-to-bromide ratio in groundwater samples to estimate the amount of chloride from atmospheric deposition versus deep basin brine. The atmospheric depositional chloride concentration was divided by the brine-corrected groundwater chloride concentration to determine the fraction of total precipitation remaining in recharged groundwater. Mapping of the resulting fraction of precipitation that becomes recharge facilitated the separation of the

overall Salt Basin into sub-watersheds with similar corrected fractions. For the lowland sub-watersheds, the runoff volume estimated by PyRANA was used in place of the total precipitation as the volume of water that could potentially become recharge, but it was assumed to have the same initial chloride concentration as precipitation. The lowland total recharge from the chloride-mass-balance method, in combination with PyRANA runoff estimate, was 5,000 acre-feet per year. In the more humid, mountainous sub-watersheds, the interception-corrected rainfall volume was used as the potential recharge water volume. The mountainous total recharge was 27,000 acre-feet per year. The resulting total corrected chloride-mass-balance method recharge rate for the Salt Basin was 32,000 acre-feet per year.

PyRANA used environmental and soil hydraulic parameters to create a soil-water-balance model that also produced an estimated recharge rate. The diffuse recharge estimated by PyRANA was 3,000 acre-feet per year, primarily occurring in the Sacramento Mountains. While the diffuse recharge is a function of precipitation, focused recharge is a function of runoff due to overland flow up-gradient and infiltration through arroyo and wash beds. The fraction of runoff that becomes recharge cannot be estimated by PyRANA and the model predicted zero diffuse recharge in the lowlands. Hence, the lowland total recharge was only predicted by the combined PyRANA runoff and chloride-based recharge fraction method described above: 5,00 acre-feet per year. The mountainous total recharge from PyRANA was found by summing the diffuse recharge and all estimated runoff into the perennial section of the Sacramento River, totaling 8,000 acre-feet per year. The resulting total PyRANA recharge rate for the Salt Basin was 13,000 acre-feet per year. The full range of new recharge estimates generated in this study is 13,000-32,000 acre-feet per year (16,000,000-40,000,000 m³/yr.), which is contained within the range of previous estimates.

Keywords: groundwater; recharge; chloride-mass-balance; PyRANA

CONTENTS

	Page
LIST OF TABLES	ix
LIST OF FIGURES	x
CHAPTER 1. INTRODUCTION	1
1.1 Background	1
1.2 Geography	3
1.3 Climate	5
1.4 Vegetation	5
1.5 Geology	6
1.6 Hydrology	10
1.6.1 Hydrological Sources	10
1.6.2 Major Flow Paths	12
1.6.3 Hydrology-Literature Review	12
1.6.4 Previous Hydrochemistry Analyses	17
CHAPTER 2. GROUNDWATER CHEMISTRY METHODS	26
2.1 Well Database	26
2.2 Differentiation of Flow Paths/Geological Provinces	26
2.3 Hydrochemical Evolution	27
2.3.1 Expected Hydrochemical Trends	28
2.3.2 Hydrogen and Oxygen Evolution	29
2.4 Han Plots– Carbon Analysis	30
2.4.1 Expected Han Plots Trends	31
2.5 Radiocarbon Corrections	32

CHAPTER 3. GROUNDWATER CHEMISTRY RESULTS	36
3.1 Basin-Wide	36
3.1.1 Basin-Wide– Hydrochemical Trends	37
3.1.2 Basin-Wide– Han Plots	39
3.1.3 Basin-Wide– Radiocarbon Analyses	40
3.2 New Mexico– Carbonates Province	42
3.2.1 NM Carbonates– Hydrochemical Trends	42
3.2.2 NM Carbonates– Han Plots	44
3.2.3 NM Carbonates– Radiocarbon Analyses	44
3.3 Texas– Cretaceous Province	45
3.3.1 TX Cretaceous– Hydrochemical Trends	45
3.3.2 TX Cretaceous– Han Plots	46
3.3.3 TX Cretaceous– Radiocarbon Analyses	46
3.4 Texas– Victorio Peak Province	47
3.4.1 TX Victorio Peak– Hydrochemical Trends	47
3.4.2 TX Victorio Peak– Han Plots	48
3.4.3 TX Victorio Peak– Radiocarbon Analyses	48
3.5 Texas– Capitan Reef Province	48
3.5.1 TX Capitan Reef– Hydrochemical Trends	49
3.5.2 TX Capitan Reef– Han Plots	49
3.5.3 TX Capitan Reef– Radiocarbon Analyses	49
3.6 New Mexico– Artesia Group Province	49
3.6.1 NM Artesia Group– Hydrochemical Trends	50
3.7 Dell City, TX– Bone Spring/Victorio Peak Province	50
3.7.1 Dell City, TX– Hydrochemical Trends	50
3.8 Texas– Salt Flats Province	51
3.8.1 TX Salt Flats– Hydrochemical Trends	51
3.8.2 TX Salt Flats– Han Plots	51
3.8.3 TX Salt Flats– Radiocarbon Analyses	51
CHAPTER 4. GROUNDWATER CHEMISTRY DISCUSSION	76
4.1 NM Carbonates Chemistry Trends	76
4.2 TX Cretaceous Chemistry Trends	77
4.3 TX Victorio Peak Chemistry Trends	79
4.4 TX Capitan Reef Chemistry Trends	80

4.5	NM Artesia Group Chemistry Trends	81
4.6	Dell City, TX Chemistry Trends	81
4.7	TX Salt Flats Chemistry Trends	82
CHAPTER 5.	WATER-BUDGET METHODS	98
5.1	NDVI Agricultural Evapotranspiration	98
5.2	Chloride-Mass-Balance Approach	102
5.3	Python Recharge Assessment for New Mexico Aquifers (PyRANA)	104
CHAPTER 6.	WATER-BUDGET RESULTS	110
6.1	Blaney-Criddle Consumptive Use	110
6.2	Chloride-Mass-Balance	110
6.3	PyRANA Runoff Recharge	113
CHAPTER 7.	WATER-BUDGET DISCUSSION	120
7.1	Water-Budget Assessment	120
CHAPTER 8.	CONCLUSION	124
REFERENCES		128
APPENDIX A.	HYDROCHEMISTRY DATABASE	135
A.1	Chemistry Data from the Assessment of Water Resources in the Salt Basin Region of New Mexico and Texas Data Summary Report (Open-File Report 608)	135
APPENDIX B.	GOOGLE EARTH ENGINE CODE FOR NDVI ACTIVE IRRIGATION ESTIMATE	136
B.1	Appendix B code is available electronically under supplementary material	136
APPENDIX C.	BLANEY-CRIDDLE TEMPERATURE AND REFERENCE CROP ET	137
C.1	Appendix C table is available electronically under supplementary material	137
APPENDIX D.	PERMISSIONS	138

LIST OF TABLES

Table	Page
2.1 Fontes and Garnier Radiocarbon Equation Input Variables	33
3.1 Fontes and Garnier Radiocarbon Corrections in the Salt Basin	54
3.2 Environmental parameters used in Fontes and Garnier radiocarbon correction	55
3.3 Mixing Radiocarbon Corrections in the Salt Basin	61
5.1 Blaney-Criddle Mean Daily Percentage of Annual Daytime Hours .	101
6.1 Blaney-Criddle Consumptive Use Estimates for Dell City, TX	116
6.2 Chloride-Mass-Balance: Areas, Runoff/Total Precipitation, Total RechargeS	118
6.3 PyRANA Total Recharge Estimates for the Salt Basin	118
7.1 Recharge for Polygons from Chloride-Mass-Balance and PyRANA .	122
7.2 All Recharge Estimates From This Project	123

LIST OF FIGURES

Figure	Page
Figure 1.1 Salt Basin Groundwater Divide and Defining Topography	4
Figure 1.2 Generalized Geologic Map of the Salt Basin	7
Figure 1.3 Generalized Geologic Diagrammatic Cross-Section of Salt Basin	8
Figure 1.4 Generalized Geologic Diagrammatic Cross-Section of Permian Basin and Guadalupe Mountains	9
Figure 1.5 Permian Structural Features of the Salt Basin	20
Figure 1.6 Laramide Structural Features of the Salt Basin	21
Figure 1.7 Cenozoic Structural Features of the Salt Basin	22
Figure 1.8 Salt Basin Observed Potentiometric Surface Map	23
Figure 1.9 Salt Basin Observed Potentiometric Map and HUC 10 Sub-Watersheds	24
Figure 1.10 Sigstedt, 2010– Salt Basin Piper Diagram with Dedolomitization	25
Figure 2.1 Salt Basin HUC 10, Observed Potentiometric Surface, and Hydrochemical Data	27
Figure 2.2 Surface Water Sub-basins within Salt Basin	28
Figure 2.3 Carbon Data Interpretation Graphs from [2]	35
Figure 3.1 Salt Basin Hydrochemistry Points by Flow Path	36
Figure 3.2 Salt Basin Hydrochemistry Points by Geologic Province	37
Figure 3.3 Map of Sulfate-to-Chloride Ratios	38
Figure 3.4 Map of Calcium-to-Magnesium Ratios	39
Figure 3.5 Map of Sodium-to-Magnesium Ratios	40
Figure 3.6 Deuterium and $\delta^{18}\text{O}$ of Salt Basin precipitation and ground- water	41
Figure 3.7 Map of $\delta^{18}\text{O}$	42
Figure 3.8 Salt Basin Overall Han Plots	52

Figure 3.9 Map of Measured Radiocarbon Activities	53
Figure 3.10 Map of $\delta^{13}\text{C}$ Concentrations	55
Figure 3.15 NM Carbonates– Han Plots	60
Figure 3.16 NM Carbonates– Sigstedt, 2010 Corrected Radiocarbon Ages	61
Figure 3.19 TX Cretaceous– Han Plots	64
Figure 3.20 Map of Mixing-Corrected Radiocarbon Ages	65
Figure 3.21 Mixing Corrected Ages with Calcium-to-Sodium and Radiocarbon	66
Figure 3.24 TX Victorio Peak– Han Plots	69
Figure 3.26 TX Capitan Reef– Han Plots	71
Figure 3.30 TX Salt Flats– Han Plots	75
 Figure 4.2 NM Carbonates Trends– Han Plots	85
Figure 4.3 NM Carbonates and Northern Dell City, TX Piper Diagram with Dedolomitization Trend	86
Figure 4.4 Shiloh Draw Piper Diagram with Dedolomitization and Cornudas Mountains Mixing Trend	87
Figure 4.5 Tritium Concentrations and F&G Corrected Radiocarbon Ages for Cretaceous	88
Figure 4.6 TX Cretaceous Trends– Han Plots	89
Figure 4.7 TX Cretaceous Piper Diagram with Dedolomitization Trend	90
Figure 4.8 TX Victorio Peak Trends– Han Plots	91
Figure 4.9 TX Victorio Peak Piper Diagram with Dedolomitization Trend	92
Figure 4.10 TX Capitan Reef Trends– Han Plots	93
Figure 4.11 TX Capitan Reef Piper Diagram with Dedolomitization Trend	94
Figure 4.12 NM Artesia Group Piper Diagram with Dedolomitization Trend	95
Figure 4.13 TX Salt Flats Trends– Han Plots	96
Figure 4.14 TX Salt Flats Piper Diagram with Halite Mixing Trend . . .	97
 Figure 5.1 Monthly Google Earth Engine Images of Active Agricultural Greenness: 2017	99
Figure 5.2 Monthly Google Earth Engine Images of Active Agricultural Greenness: 2011	106
Figure 5.3 Monthly Google Earth Engine Images of Active Agricultural Greenness: 2019	107
Figure 5.4 Google Earth Engine Greenness Threshold-defining Cell .	108

Figure 5.5 Chloride Mixing Curve for Chloride-Mass-Balance Approach	109
Figure 6.1 Aerial Extent of Active Agricultural Greenness from Google Earth Engine	111
Figure 6.2 Annual Consumptive Use for Dell City Irrigation District . .	112
Figure 6.3 Chloride Mixing Curve with Salt Basin Hydrochemistry Data	113
Figure 6.4 Map of Corrected Chloride Recharge Rates and Chloride-Mass-Balance Polygons	114
Figure 6.5 Chloride-Mass-Balance Recharge Fractions Comparison . .	117
Figure 6.6 Aerial Extent of Diffuse Recharge from PyRANA	119

This thesis is accepted on behalf of the faculty of the Institute by the following committee:

Daniel Cadol

Academic and Research Advisor

Fred Phillips

Alex Rinehart

I release this document to the New Mexico Institute of Mining and Technology.

Beth Ann Michelle Eberle

July 17, 2021

CHAPTER 1

INTRODUCTION

1.1 Background

Many semiarid regions are at extreme risk of water supply shortage over the next 30 years as the groundwater and surface water resources are expected to be dramatically reduced due to climate change [3]. These dryland regions account for 40% of Earth's land surface and contains a third of the Earth's population [4]. Agriculture in drylands requires a water resource to sustain the 2.5 billion living within these regions and millions more that rely on the agricultural products. The semiarid nature of the drylands amplifies the importance of groundwater in maintaining a potable and agricultural water source, since surface water is minimal and usually unpredictable [5]. Groundwater resource sustainability and thus dryland agriculture sustainability has become increasingly relevant to society as the world continues to grow and as climate change continues to strengthen.

The stability and quantity of groundwater available for societal use depends upon the incoming and outgoing water of the study basin. Incoming water refers to precipitation and groundwater or surface inflow from external basins. Water can leave a basin via evapotranspiration (ET), groundwater or surface outflow into external basins, or in the form of agricultural products. A water-budget can be calculated by subtracting all of the outgoing water from the incoming water, with the excess water that enters but does not leave the basin contributing to storage in a groundwater reserve for future use. It is that reserve that needs to be maintained and managed to sustain those who utilize the groundwater.

Climate change is becoming increasingly disruptive to management activities aimed at balancing the hydrological system because it can significantly decrease or increase the amount of water entering and leaving a basin depending upon location [6, 7]. In arid environments, climate change is increasing the average air temperature and typically decreasing the amount of precipitation [6]. These effects make evapotranspiration and droughts more prevalent. With less water entering the basin and more water exiting, there would be a negative impact upon the amount of water entering the groundwater reserve.

There are multiple techniques to assess groundwater resources, with one of the foremost being physics-based modeling. A finite-difference approach is common to produce a three-dimensional, steady-state and transient model in which complex systems are analyzed [8]. This modeling practice exemplifies a limitation

of physics-based modeling: they require extensive inputs and computational expenditure. Physics-based modeling is simplified in part by pre-developed codes, such as MODFLOW, that reduce the model construction time [1, 8–12]. Physics-based models function well to visually map the three-dimensional movement of the water in the study basin. Due to the nature of the estimated inputs, the resulting models can run simulations for different water-budgets at different temporal scales. Physics-based models are convenient when focusing on the quantity and movement of groundwater resources, but fails to qualify the types of water in the study basin.

Assessment of the quantity and quality of groundwater are important when attempting to evaluate the water for potable or agricultural use in a semiarid basin. The second overarching technique to assess the groundwater resource is geochemical analyses. This approach focuses on the geochemistry of the water in the basin, and in doing so, measures the water quality. The relative concentrations of major ions, minor ions, and stable isotopes within the water samples throughout the basin can designate the quality, evolution, age, and potential mixing of the water along the flow path [13–17]. Environmental tracers are a category of hydrochemical constituents, including many isotopes, that can be used to determine chemical evolution pathways throughout the water system. Stable isotope ratios are expressed in terms of delta values (δ) in units of per mil (‰). Delta values represent the relative concentration of a given isotope with respect to the concentration of most abundant base isotope in a sample versus the same ratio of given isotope to base isotope in a standard reference material, all multiplied by 1000 to facilitate comparisons between delta values. The delta value is given by

$$\delta^* X = \left(\frac{{}^*X_{\text{sample}} / X_{\text{sample}}}{{}^*X_{\text{standard}} / X_{\text{standard}}} - 1 \right) \times 1000 \quad (1.1)$$

For example, delta oxygen-18 is the concentration of oxygen-18 in the sample over the concentration of oxygen-16 in the sample over the same ratio of isotopes in Standard Mean Ocean Water (SMOW). This ratio of ratios is subtracted by one and multiplied by 1000. The relative delta value can change as the water undergoes fractionation, with an unequal exchange of a given isotope with respect to the abundant base isotope. With some modification and correction factors, geochemistry can be utilized to estimate groundwater recharge based on radioactive carbon-14 or radiocarbon concentrations, along with other chemical components and subsequent analyses [14, 17–22]. The major disadvantage of using the geochemical analyses technique is the necessity of chemical analyses from well water samples. This hindrance is negligible if the study basin has a well-established historic hydrochemistry database.

The water balance approach to evaluating groundwater resources ties closely to the hydrological budget of incoming and outgoing waters. The purpose of the water balance is to comprehensively quantify each inflow and outflow, as well as any missing components. Each sub-basin contributes a certain amount of water. A simplified version of the water balance evaluates the groundwater recovery in

water wells and assumes that the well recovery volume is equal to recharge [23]. The water balance method is often used to estimate groundwater recharge in hydrologically closed semiarid basins by determining the evapotranspiration leaving the hydrological system [24–28]. Despite the precisely estimated inputs used for the water balance, the results are similar to that of a physics-based model; the hydrological system is quantified, but there is no measure of water quality.

The water-budget of semiarid regions is vital to the continued prosperity of those regions where water is a limited resource. As growing urban water use competes with farming in semiarid regions, the groundwater usage needs to be regulated to ensure sustainability. Understanding the extent, quantity, and quality of a hydrological system helps facilitate the creation of a localized water management plan to accurately evaluate the amount of water available for irrigation pumping and potable water usage. The New Mexico Office of the State Engineer (OSE) Water Rights Division has established multiple water right rules, regulations, and guidelines that effectively limit the amount of groundwater pumping to maintain a sustainable water resource for multiple basins and sub-regions within each state [29]. The U.S. Bureau of Reclamation in the western United States funds research into the water-budget of watersheds in order to manage, develop, and protect the water resources within each watershed [30].

In realization of its mission statement and to quantify interstate transfer of waters, the U.S. Bureau of Reclamation has funded an assessment of water resources in the Salt Basin, NM/TX. This project is intended to evaluate the groundwater availability in the Salt Basin, help assess the local sustainability of current groundwater usage, and indicate the implications for future development [31]. The primary research goal of the water-budget component is to narrow the range of previous groundwater recharge estimates. There have been eleven prior estimates of groundwater recharge in the Salt Basin, ranging from 6,000 to 240,000 acre-feet per year, each of which will be explained in further detail later [31]. I hypothesize that the recharge in the Salt Basin is closer to the lower end of that range. By producing accurate and modernized groundwater recharge estimate, the overall water-budget will be enhanced, the most effective water resource management plan can be instituted, and the welfare of the semiarid basin can be sustained.

1.2 Geography

The Salt Basin is a 13,000 km² (5,000 mi²) hydrologically closed basin shared between southeastern New Mexico and northwestern Texas (Figure 1.1). The areal extent of the basin covers parts of Otero, Chaves, and Eddy counties in New Mexico and parts of Hudspeth and Culberson counties in Texas. There are approximately 1,000 residents within the Salt Basin across these five counties [32, 33]. The population centers of the Salt Basin are Timberon, NM, Piñon, NM, Cornudas, TX, and Dell City, TX. The New Mexican communities are located near the northern margin of the Salt Basin and contain approximately 300 and 100 people, respectively [14]. Cornudas and Dell City, TX are along the state-border

and account for approximately 400 for each city [32, 33]. The Salt Basin population is sparse. Many of the residents rely on dryland farming and ranching, though groundwater-supplied irrigated agriculture prevails near Dell City. Fort Bliss and the McGregor Range encompasses the eastern margin of the Salt Basin [34]).

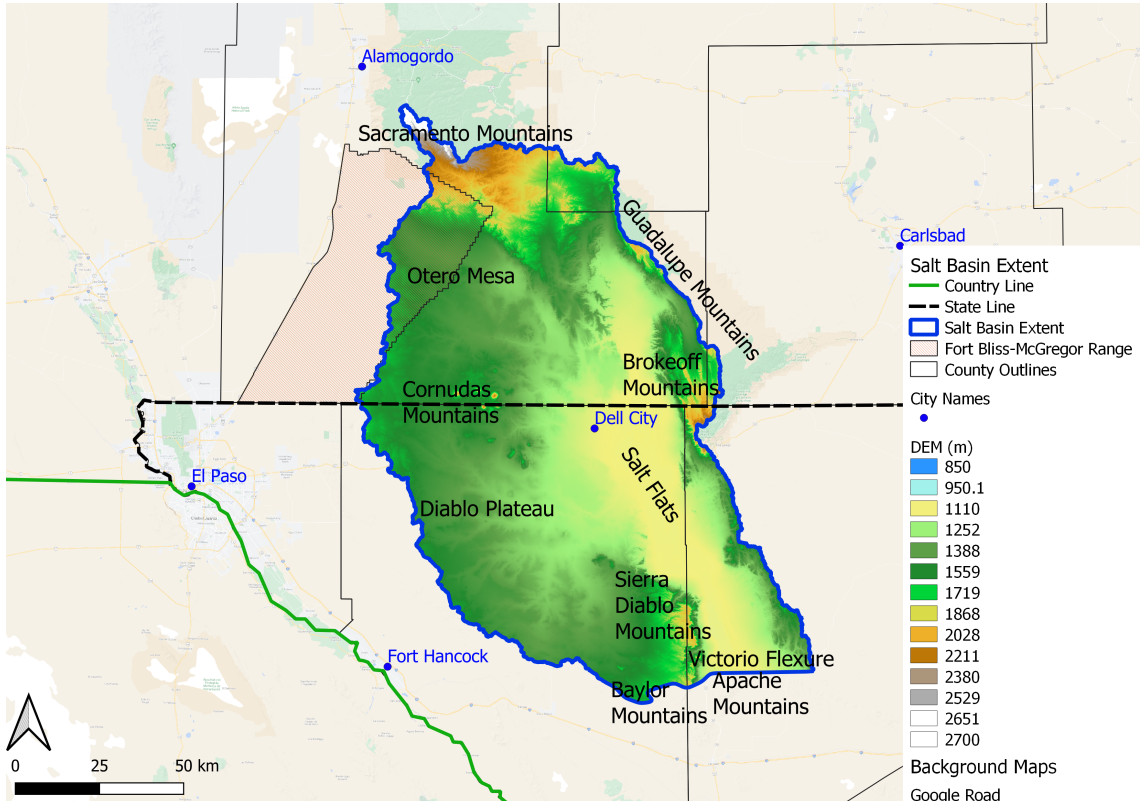


Figure 1.1: Salt Basin groundwater divide with defining topographic features labeled, cities are labeled and denoted with blue dot, state boundaries are dashed lines, country border is green, county borders are thin, black lines, and Fort Bliss-McGregor Range is highlighted in red crosshatching; Salt Basin colored by elevation with white being high elevation and green being lower elevation

Mountainous topography above 1,500 m in elevation comprises approximately 14% of the Salt Basin and is predominately concentrated along the northern and eastern margins. The highest point of the Salt Basin is approximately 2,900 m at Sacramento Peak in the Sacramento Mountains to the north. A majority of the Salt Basin, around 63% of the area, consists of low relief ‘lowlands’ that range from 1,200 to 1,500 m in elevation, with the high point being in the Otero Mesa/Diablo Plateau in the western Salt Basin. The Cornudas Mountains form an isolated group of peaks that climb steeply to 2,100 m in elevation [14]. The basin’s deepest portions, at about 1,000 m elevation, comprise the remaining 23% of the Salt Basin and form playas known as the Salt Flats near the eastern margin.

The hydrological boundary of the Salt Basin is designated by multiple features

that are the result of tectonic activity associated with the orogenic events of the Sacramento section of the Basin and Range province [12, 14]. The northern watershed divide is created by the southern Sacramento Mountains. The Guadalupe, Brokeoff, and Delaware Mountains form the eastern watershed divide of the Salt Basin. To the west, the Salt Basin hydrological boundary is formed on the edge of the Otero Mesa/Diablo Plateau uplift where it transitions into the Tularosa Basin further westward. The southern border of the Salt Basin, as defined by this study, is the groundwater divide created by the Victorio Flexure [35–37]. This flexure effectively restricts groundwater flow as it strikes NW-SE on the western portion, adjacent to the Baylor Mountains, and strikes E-W on the eastern portion that is adjacent to the Apache Mountains [35]. This southern boundary has been modified from the New Mexico Office of the State Engineer (OSE) designation of the Salt Basin that originally continued farther southward into Texas [14].

1.3 Climate

Southeastern New Mexico and far western Texas are semiarid with a wide range of temperatures. For Dell City, TX the maximum daily temperature ranges from 14 to 37°C (58 to 99°F) while the minimum daily temperature ranges from -4 to 18°C (24 to 64°F). The average daily temperature for the overall Salt Basin ranges from 5 to 28°C (41 to 82°F) [38]. The higher elevations have a naturally cooler climate, averaging between 6 and 10°C (43 to 50°F) [14]. According to NOAA's monthly average climatology for the United States, the Salt Basin receives between 180 to 340 mm per year in the lowlands and between 380 and 900 mm per year in the high elevations of the Sacramento Mountains [17, 39, 40]. Most of this precipitation falls as rain during the monsoon season from May to October [17, 40, 41].

1.4 Vegetation

Natural flora in the Salt Basin is elevation dependent and is differentiated based on the EPA's level IV designation [42]. This classification system divides the conterminous United States into more than 100 ecoregions based on similarities in topography, ecology, stratigraphy, hydrology, and other such classifications [42]. The higher elevations of the Salt Basin are similar to the Rocky Mountains conifer forests as they share ponderosa pine, Douglas-fir, and some oak species. Just to the south of the Sacramento Mountain ridges and extending east into the Guadalupe Mountains, the vegetation transitions into the Madrean Lower Montane Woodlands. In these foothills, there are mixed ponderosa pines, junipers and oak species, and mixed desert grasses. Moving further south and into the Salt Basin, the vegetation becomes characteristic of Chihuahuan Desert Slopes with mixed desert grasses and desert shrubs. The majority of the Salt Basin is flat lowlands that are designated Chihuahuan Desert Grasslands. These lowlands are vegetated by

mixed desert grasses, desert shrubs, and scattered desert brush. The Salt Flats and southern playas of the Salt Basin are sparsely vegetated around the margins of the playas with desert grasses and desert shrubs that compose the Chihuahuan Basins and Playas designation. Within the playas, there is a lack of vegetation. The last ecoregion of the study area is a small block along the southern margin of the Salt Basin around the Sierra Diablo mountains. This is the Chihuahuan Montane Woodlands that is comprised of a mix of evergreen conifers, oaks, junipers, ponderosa pine, Douglas-fir, and desert grasses.

Due to the relatively flat lowlands, frequent sunshine, mild winters, and, foremost, presence of abundant groundwater, there is agricultural activity in the central Salt Basin [14]. The agronomic flora is mostly isolated in Dell City, TX and are mostly alfalfa, chiles, and cotton [41, 43]. These crops are common in semiarid environments as they are capable of withstanding the harsh climate with centerpivot and flood irrigation [43]. The season for planting and production of alfalfa, chiles, and cotton ranges from April into December [44]. While the entirety of the Salt Basin extends beyond Otero County, NM and the county extends beyond the basin, the agriculture of this county should be representative of the agriculture of the Salt Basin. Livestock in Otero County is predominantly cattle and sheep [44]. Grazing livestock eat the desert grasses and drink the pumped groundwater.

1.5 Geology

The geology of the Salt Basin is complex, deformed, and spans many geologic time periods. Surficial geology ages range from Permian to Quaternary while the overall stratigraphic age of the Salt Basin ranges from Precambrian to Quaternary (Figure 1.2; [31]).

The most prominent surficial geology in the New Mexico portion of the Salt Basin are also the primary aquifers of the Salt Basin: Permian carbonates (Figure 1.2). These carbonates were deposited in a shelf and shelf-margin marine environment during a period of sea level change due to the evolution of the Delaware Basin during the Guadalupian epoch (Figure 1.3; [31]). The Yeso formation is in the western Salt Basin surficial geological unit. This formation is a heterogeneous stratigraphic unit from the Guadalupian/Leonardian time period that consists primarily of limestones and dolomites interbedded with gypsum, siltstone, and shale [14, 31, 45, 46]. The San Andres formation is mapped as 'Leonardian, undivided' in Figure 1.2 and comprises the remainder of the New Mexico surficial geology. This formation is primarily dolomite with intermixed shale beds and sandstones [14, 31, 46]. The Yeso and San Andres formations are equivalent to the Victorio Peak and Bone Spring limestone formations in the Texas portion of the basin [47]. The Victorio Peak limestone becomes the Bone Spring formation as the depositional environment changes from shelf-margin to basin [31, 48]. Both of these units are limestone and dolomite intermixed with siliceous shale and sandstone [23]. All of the carbonate aquifers within the Yeso,

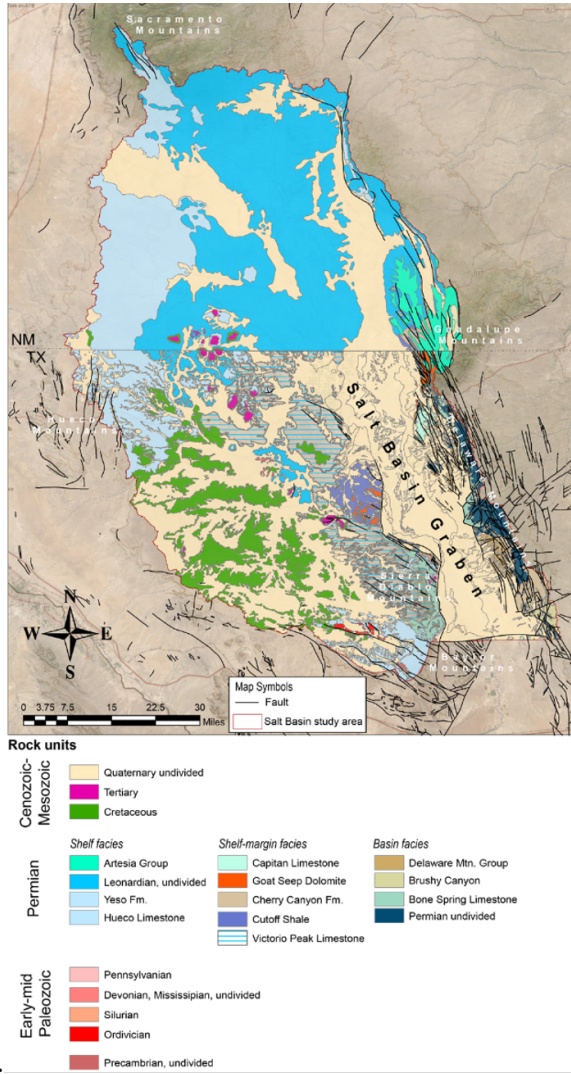


Figure 1.2: From [31]; Generalized geologic map of the Salt Basin area

San Andres, Victorio Peak, and Bone Spring formations are interconnected and contain characteristic karst that facilitate flow [10, 11, 23, 24, 41].

Along the state border in the southwestern Otero Mesa/northwestern Diablo Plateau, the Cornudas Mountains are exposed igneous intrusions with additional intrusions in the surrounding subsurface [50–52]. These intrusive laccoliths, sills, and dikes were created when Precambrian rocks were metamorphosed into phonolite and syenite and pushed through the subsurface [14, 31, 52, 53].

A secondary aquifer unit exists in the southwestern Salt Basin: the Finlay formation. This aquifer unit is a Cretaceous sea shelf limestone that was fractured with carbonate dissolution contributing to additional permeability [31, 54]. Kreitler (1986) [54] is the primary source for information about this Cretaceous unit and surrounding geology. The Finlay limestone has secondary permeabil-

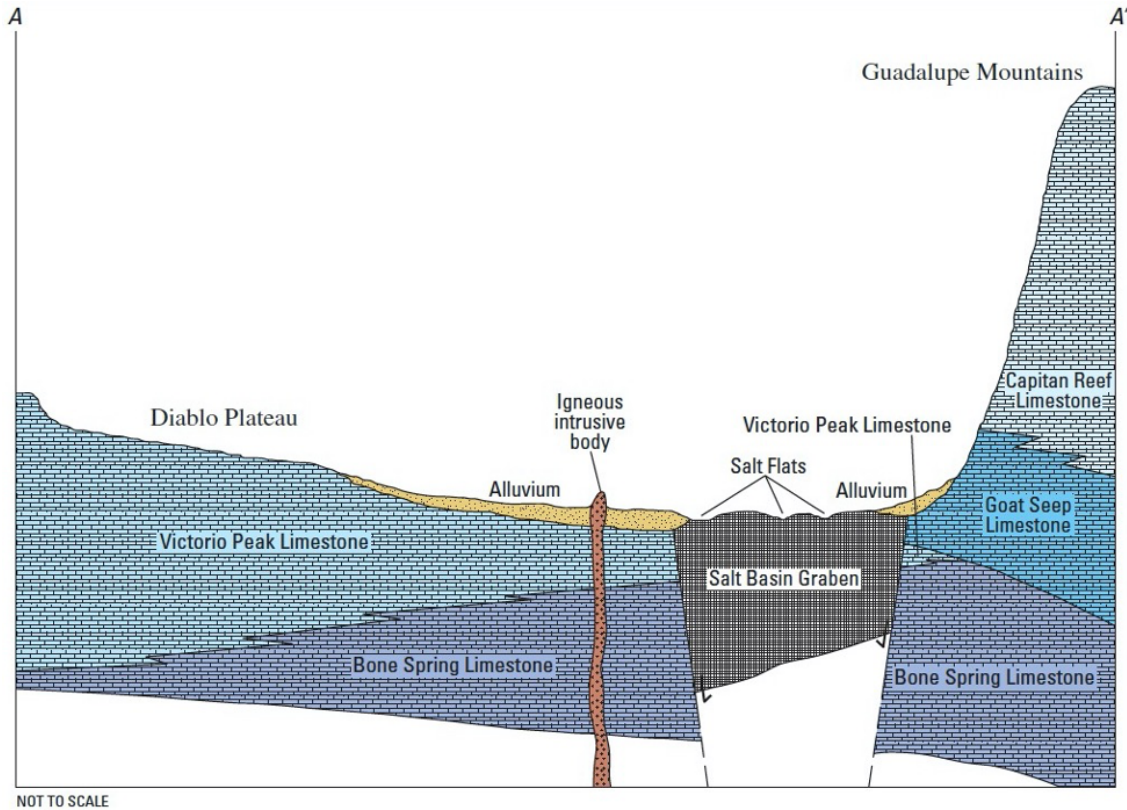


Figure 1.3: From [23], reproduced in [31, 49]; generalized geologic diagrammatic west-east cross section of the Salt Basin and Guadalupe Mountains showing shelf-margin and basin facies partially overlaid by alluvium

ity and large hydraulic conductivities due to carbonate dissolution and minor faulting. The Finlay limestone formation is juxtaposed with a coarsely fractured Precambrian rhyolite porphyry. Wasserburg et al. (1962) [55] found a rhyolite porphyry exposed at Pump Station Hills in Hudspeth County, TX that was dated to be 1 billion years old using rubidium-strontium dating. Since this age coincides with the Precambrian rhyolite porphyry from Kreitler (1986) [54], the unnamed rhyolite porphyry from Kreitler (1986) [54] will hence be referred to as the ‘Pump Station Hills rhyolite porphyry’. The Pump Station Hills rhyolite porphyry is heterogeneously fractured, with fractures striking in multiple directions and dips ranging from vertical to horizontal. These variable fractures are not sealed with any mineral precipitation. Kreitler (1986) [54] refers to the shallow aquifer in the Finlay limestone as HU1B and the deeper aquifer in the Pump Station Hills rhyolite as HU1A. The fractures in both aquifers are highly heterogeneous, are likely interconnected, and contribute to a variable flow system that is not fully fracture-controlled.

Along the eastern margin of the Salt Basin and within the Delaware Mountains, the Capitan Reef complex is the dominant carbonate shelf-margin facies.

This geological complex includes the western edge of the Capitan limestone, parts of the Goat Seep dolomite, and a few interbedded sandstones (Figure 1.2 and Figure 1.3; [31]. Both the Capitan limestone and Goat Seep dolomite are highly permeable with high groundwater transmissivities [31, 56]. The majority of gypsum and evaporite beds in the Capitan Reef complex have been removed over time due to erosion down the Guadalupe Mountain slope [56].

The Permian shelf facies, which are time-equivalent to the Capitan Reef complex, make up the Artesia Group in the Guadalupe Mountains (Figure 1.4; [31, 48, 57]. This group is comprised of five formations, each are dolomites interbedded with sandstones [46]. The oldest formation within the Artesia Group is the Grayburg. Subsequent formations are the Queen, Seven Rivers, Yates, and Tansill formations [31].

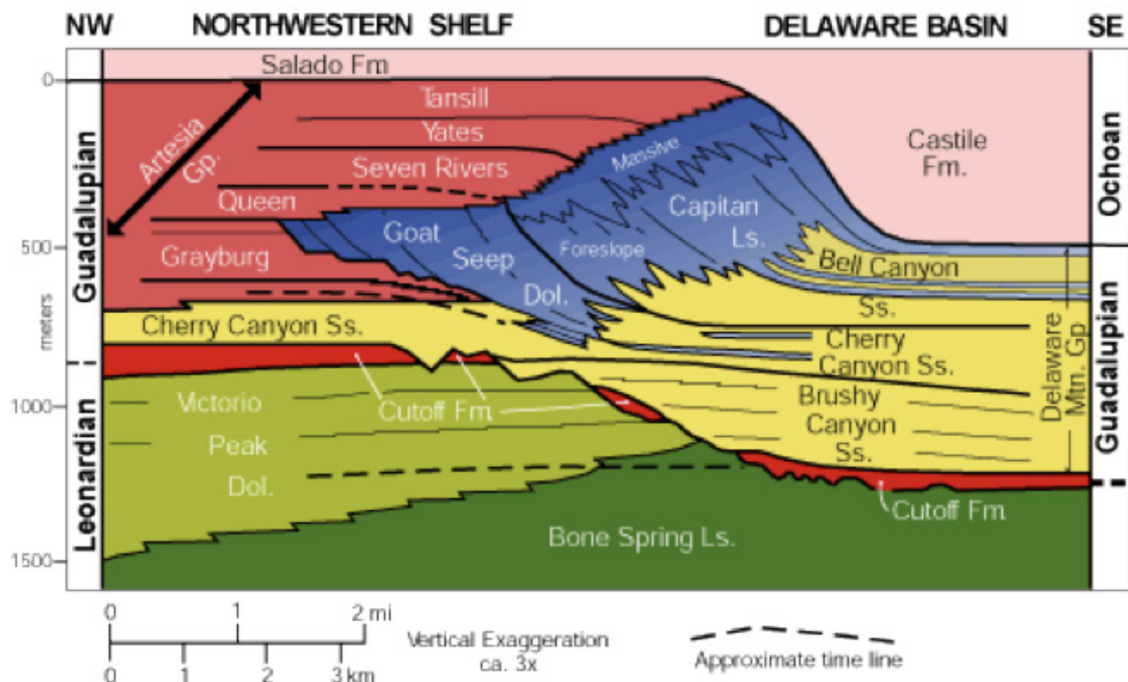


Figure 1.4: Reproduced in [31]; generalized geologic diagrammatic through Permian Basin and Guadalupe Mountains showing stratigraphic nomenclature of Permian strata in the Guadalupe Mountains

Denoted by the name of the basin, there are Quaternary to recent evaporites within the Salt Basin, concentrated in the Salt Flat playas in the southeastern portion of the basin. There are gypsum, halite, calcite, dolomite, and quartz sediments in the Salt Flat playas [25, 31, 58, 59]. These salt playas were the motivation behind the El Paso Salt War in the 1860s [60]. The Salt Flats have high evaporative potential and are effectively the discharge area for the Salt Basin groundwaters [13, 25].

Other secondary aquifer units are unconsolidated Neogene alluvial and bol-

son deposits (Figure 1.3; [23, 31, 49]). These bolson deposits are sediments eroded from exposed carbonates and moved along ancestral drainages [31, 37]. Alluvial and bolson deposits are combined with lacustrine fine-grained clays to form the basin fill that has accumulated in the central Salt Basin to a maximum thickness of 2,400 feet [31, 35]. Thinning of the basin fill near the basin margins is especially evident on the southern side of the Baylor Mountains due to the Victorio Flexure [31, 35]. Ephemeral channels of the Salt Basin are comprised of these alluvial deposits [61].

The Salt Basin is part of the overall Permian Basin that was formed during the Mississippian/Pennsylvanian collision of the North and South American plates [62]. Those original deposits have been subsequently deformed into the modern Salt Basin. Intensely faulted terrain was caused by three time periods of major tectonic activity: mid-to-late Permian, the Late Cretaceous–Paleogene Laramide orogeny, and Neogene Basin-and-Range tectonism [31]. During the mid to late Permian, the Otero fault, Babb and Victorio Flexure, and Bitterwell Break were created (Figure 1.5; [12, 63, 64]). The Otero fault cuts through the Otero Mesa / Diablo Plateau and continues towards the southeast, striking northwest and displacing down to the northeast. The monocline flexures cut through the basement blocks of the Salt Basin graben and trend northwest to southeast with a northeastward dip [64]. The Victorio Flexure has a more easterly trend as compared to the Babb Flexure [63]. The Bitterwell Break is a fault through the Salt Basin graben basement rocks trending northeastward from the Babb Flexure towards the Delaware Mountains. The Victorio Flexure and Babb Flexure deformed the Cretaceous Finlay formation and Precambrian Pump Station Hills rhyolite porphyry [54]. The Late Cretaceous Laramide orogeny produced folds, primarily in the New Mexico portion of the Salt Basin (Figure 1.6; [12]). A later structure, named the Otero Break, was added to the Salt Basin during the Neogene when west-oriented extension tilted previously northeast trending synclines, anticlines, and graben fault blocks into west dipping normal faults (Figure 1.7; [12, 40, 64]). This break extends to the southeast from the southern Sacramento Mountains near Timberon, NM. Additional faulting throughout the Sierra Diablo Mountains coincided with the Otero Break formation in the Neogene [12].

1.6 Hydrology

1.6.1 Hydrological Sources

Once precipitation enters the endorheic Salt Basin, the water either evaporates in the semiarid climate or infiltrates into the groundwater system. There is minimal surface water present in the Salt Basin [11, 14, 41, 65]. The majority of recharge into the Salt Basin originates as winter precipitation in high elevations of the Sacramento Mountains and infiltrates through fractures and permeable, coarse-grained alluvium before reaching the basin center near Dell City, TX [9, 11, 13, 14, 16, 17, 22, 24, 41, 65, 66]. The groundwater is internally drained

toward the center of the basin near Dell City, Texas (Figure 1.8). To clarify: water in the southwestern Salt Basin flows towards the northeast [10, 13, 23, 24, 35] and water in the northwestern Salt Basin flows towards the southeast along Otero Break fractures [11, 14, 23, 36, 40, 47, 64, 65, 67]. This interpretation is corroborated by ^{34}S analyses [16]. The relative isotopic abundance of ^{34}S increases from the Sacramento Mountain ridges to the mountain lowlands near Alamogordo, Tularosa, Peñasco, and Artesia and since the isotopic signature is consistent with Permian marine gypsum, the water appears to flow past and dissolve that gypsum before reaching the open plains [16]. Groundwater samples from the Otero Break are consistent with this interpretation, as those waters contain low TDS (approximately 500 mg/L) due to the high groundwater velocity from the recharge area in the Sacramento Mountains [14, 40]. The overall trend for the Salt Basin shows an increase in TDS moving toward the south. This pattern is consistent with the previously described flow paths, as there is more enrichment of TDS with both increased water-rock interactions and increased evaporation through the vadose zone during recharge.

The Salt Basin shares the Sacramento Mountain highlands with the Peñasco Basin to the northeast and the amount of cross-divide flow between the two basins is controversial. Groundwater inter-basin flow into the Salt Basin from the Peñasco Basin is explicitly quantified as 7,954 and 5,541 acre-feet per year by Finch (2002) [9] and Shomaker (2010) [11], respectively. The model domain used by Finch (2002) included adjacent parts of the Peñasco Basin since the groundwater elevation contours along the northern boundary of the Salt Basin showed the two basins being hydraulically connected, specifically between Timberon and Piñon, NM [9]. Shomaker (2010) used Darcy's Law calculations to estimate the groundwater inflow from the Peñasco Basin assuming most of the inflow went into the San Andres and Yeso Formations and assuming aquifer parameters for each unit [11]. Though not quantified, Sigstedt et al. (2016) [17] referred to a minor component of recharge moving southwards into the Piñon Creek sub-basin due to inter-basin subsurface drainage from the Peñasco Basin. As groundwater flow across the watershed boundary is not required to balance the hydrologic system, Mayer (1995) [40] suggested that the inflow is effectively negligible. Stating there is a lack of data to create a conclusive argument in either case, Hutchison (2008) [10] assumed there was negligible inter-basin groundwater inflow from the Peñasco Basin. In short, some previous researchers quantified groundwater inflow, some considered inter-basin groundwater flow to be negligible, and many ignored the possibility completely.

There is a component of aquifer recharge that is the result of infiltration of irrigation water that was itself originally pumped from the aquifer [23]. The irrigation returns by deep seepage ("return flow") draws down salts that build up in the evaporative layer and transports them into the aquifer [40, 41]. The quantity of irrigation return flow depends on the quantity of irrigation water required to sustain the crops and livestock in the given climatic conditions. Mayer (1995) [40] estimated that the return flow is between 30 and 50% of the irrigation volume applied to the surface. Since farmers strive to minimize costs associated with extraneous water usage, it is possible that there is less irrigation return flow to the

aquifer than Mayer (1995) [40] suggests. In most recharge estimation calculations, the return flow volumes of water are considered negligible or not included to simplify the recharge investigations to natural recharge.

1.6.2 Major Flow Paths

The major water flow paths follow the Sacramento River, Piñon Creek, and Shiloh Draw, while some of the minor flow paths follow Cornucopia Draw, Big Dog Canyon, Antelope Draw, South Well Draw, Capitan flow path, and the Salt Flats (Figure 1.9). These sub-watersheds are from the United States Geological Survey's (USGS) National Watershed Boundary Dataset (WBD) [68]. As further clarification, the sub-watersheds are classified under the USGS Hydrological Unit Code (HUC) as 10-digit watersheds within the Salt Basin subbasin within the Rio Grande Closed Basins basin and subregion within the overall Rio Grande region [69]. The Sacramento River has its headwaters in the high elevations of the Sacramento Mountains, but it is only perennial for a short distance before infiltrating back into the groundwater system. The water from the Sacramento River dominantly recharges the San Andres, Yeso, Bone Spring, and Victorio Peak fractured limestone aquifers through channel infiltration and subsequent underground lateral flow [13, 17, 35, 70]. Piñon Creek has its headwaters in the southeastern Sacramento Mountains where the Peñasco Basin contributes groundwater inflow before the creek follows the Salt Basin margin to the east and then southward to meet the Salt Flats. Like the Sacramento River, Piñon Creek recharges the limestone aquifers near the eastern margin of the Salt Basin. Shiloh Draw is a catchment on the Otero Mesa/Diablo Plateau that is dry outside of the monsoon season, during which there are ephemeral flows. This western catchment contributes to the limestone aquifers that predominate in the Salt Basin. Antelope Draw and South Well Draw are ephemeral channels that flow from the southwestern margin of the Salt Basin into the Salt Flats south of Dell City, TX. These draws flow through Cretaceous fractured limestone and rhyolites [54].

1.6.3 Hydrology-Literature Review

The water-budget of the Salt Basin includes: precipitation, groundwater inflow, pumping, evapotranspiration (ET), and groundwater recharge into the carbonate aquifer. Outgoing water excludes groundwater or surface water outflow because the Salt Basin is a hydrologically closed basin. All of the water in a closed basin is internally drained and the basin is effectively an isolated hydrological system (Fan, 1997). Most the components of the water-budget can be estimated independently with historic data, with the expectation of the groundwater recharge and the associated groundwater storage. As a result, the recharge is the primary estimate that is frequently modified in association with distinct research methods.

There have been twelve groundwater recharge estimates for the Salt Basin made since 1957 that estimate from 6,000 to 240,000 acre-feet per year.

Coinciding with the 1950's development of water resources within the Salt Basin, Bjorklund (1957) [41] was one of the first to make an estimate of recharge for the basin, speculating that it was less than 100,000 acre-feet per year. This loose estimate was made with inspection of well water fluctuation in response to irrigation pumping. When the pumping rate removed more than 100,000 acre-feet per year from the aquifer, there was noticeable downdraw in the irrigation wells. Bjorklund (1957) [41] proposed that a pumping rate less than or equal to the recharge rate would result in negligible drawdown. There were no supporting calculations; the estimate was based on observation of water levels [41]. Irrigation return flows and evaporation would complicate the groundwater flow system and likely decrease the recharge rate for the basin. Being the earliest recharge estimate for the Salt Basin, this simple recharge estimate from Bjorklund (1957) [41] does not account for the complexity of the groundwater system, modern precipitation rates, nor modern recharge rates.

Similar to Bjorklund's well water level fluctuation method, Ashworth (1995) [23] estimated that the recharge of the groundwater system of the Salt Basin would be 90,000 to 100,000 acre-feet per year. Ashworth (1995) [23] observed that pumping rates between 40,000 and 60,000 acre-feet per year resulted in a well water level rise, while pumping rates between 90,000 and 100,000 acre-feet per year resulted in no change to the water level. For a water balance, the discharge from the groundwater system in the form of irrigation consumptive use should be roughly equal to the recharge. It was assumed that this recharge estimate inherently contains potential recharge from lateral inflow from the Peñasco Basin to the northeast and irrigation return flow [23]. There were no supporting calculations for the groundwater recharge estimate nor exploration of recharge rates greater than 100,000 acre-feet per year made by Ashworth (1995) [23], so there is limited reliability in the estimate.

Mayer (1995) [40] estimated a recharge of 88,000 to 100,000 acre-feet per year. The source of recharge is split between irrigation return flow and distributed recharge from across the surface area of the Salt Basin, contributing 30,000-42,000 and 58,000 acre-feet per year, respectively. Multiple sources cite Mayer's 1995 recharge estimate as the distributed recharge value rather than the combined quantity [11, 25, 65]. The irrigation return flow has a range of values as it depended upon chosen soil permeability and climatic conditions. Distributed recharge is further broken into two components: high elevation recharge (57,400 acre-feet/year) and low elevation recharge (600 acre-feet/year). Mayer (1995) [40] used the Maxey-Eakin method to estimate high elevation recharge above 1,600 m. Maxey-Eakin recharge method was first established and applied to valleys within the Great Basin, Nevada in 1949. This method determines recharge coefficients based on the 'precipitation zone', or the average annual precipitation amount for each area. That coefficient is then applied to volumes of precipitation within a given area of a closed arid basin to ultimately estimate groundwater recharge [71, 72]. The Maxey-Eakin equation is given by

$$R = \sum_{i=1}^N \beta_i \bar{P}_i A_i \quad (1.2)$$

This equation calculates the recharge as the sum of a recharge coefficient (β), the average long-term precipitation within the area as the ‘precipitation zone’ (\bar{P}), and the aerial area of the specified area. The ‘N’ parameter in the equation denotes the number of precipitation zones within the overall study area [72]. In order to apply this method to the Salt Basin, Mayer (1995) [40] assumed there were similar climate conditions, geology, and lithology between the high elevations in the Salt Basin and the Great Basin, NV. While the higher elevations on average have more precipitation than evaporation, lower elevations are usually dominated by evaporation. The lower elevations recharge estimates are based on soil-chloride profiles from the Diablo Plateau [40]. By distinguishing the differences in precipitation and recharge relationships based on elevation, Mayer (1995) [40] produced a recharge estimate with a lower source of error than those estimates that upscaled across the entire basin regardless of elevation. Nonetheless, the recharge quantity that Mayer (1995) [40] estimated has limited reliability as the assumption that Nevada and the Salt Basin have similar climates is inaccurate; Nevada receives most of its precipitation in the winter and the Salt Basin receives most of its precipitation in the summer monsoon season [39]. This discrepancy most likely means that more of the Salt Basin precipitation is evaporated in the hot summer climate and less is truly being recharged, although the higher intensity of monsoon precipitation may lead to greater runoff volumes and therefore greater focused recharge.

Finch (2002) [9] estimated a recharge of 54,943 acre-feet per year for the entire Salt Basin. The majority of this recharge (35,000 acre-feet per year) originates in the New Mexico portion of the Salt Basin. This value was estimated using a surplus precipitation method. Assuming surplus of precipitation occurs during the winter months when evaporative potential is minimal, almost all of the winter-storm precipitation will runoff into the basin center with negligible infiltration or evaporation [9]. To corroborate the estimate for the northern portion of the Salt Basin, the highly fractured rock along the Otero Break is assumed to be a preferential recharge flow path that supports most of the 35,000 acre-feet per year of recharge. The total recharge estimate for the Salt Basin was determined using a three-dimensional steady state groundwater flow model water balance [9], and thus the recharge estimate depends strongly on the hydraulic conductivity distribution assumed for the model.

In 2004, Last Chance Water Company, in collaboration with Sandia National Laboratories, provided a recharge estimate for Salt Basin to be between 30,000 and 240,000 acre-feet per year [24]. This estimate is based on previous work done by Gates (1980) [35] and Ashworth (1995) [23] and carries the same potential errors. Chace and Roberts (2004) [24] cite the overall range of recharge, but emphasizes the possibility that recharge is towards the higher end of the range between 100,000 and 240,000 acre-feet per year. This inclination is the result of observations of monsoonal flow in sub-basins not included in previous estimates:

Cornucopia Draw, Shiloh Draw, and Fourmile Draw [24]. Although the draws appear to carry a large volume of water during high intensity precipitation events, subsequent researchers suggest that their contribution to recharge is negligible compared to the quantity of recharge from precipitation in the high-elevations of the Sacramento Mountains [14, 16]. There is no original data provided to support the claims of Chace and Roberts (2004) [24] and thus, their recharge estimate has limited value.

Hutchison (2008) [10] used the Maxey-Eakin method and transient groundwater budget model calibrations to estimate recharge for the Salt Basin of 71,531 acre-feet per year. Mayer (1995) [40] used the same method for part of their analysis. The models used by Hutchison (2008) [10] focused on distinct components of the groundwater-budget: structural geology, isotopic geochemistry, and a hybrid of the two. The structural geology model is based on work from Mayer (1995) [40] that postulates a preferential flow path along Otero Break from the Sacramento Mountains to Dell City, Texas [10]. Eastoe and Hibbs (2005) [73] was the basis of the isotopic geochemistry model suggesting that a significant portion of recharge in Dell City, Texas originated in the Diablo Plateau, west of the city [10]. The hybrid model combines the two likely sources of water for Dell City, Texas to estimate a groundwater-budget for the entire Salt Basin. This recharge estimate contains error associated with the Nevada-calibrated Maxey-Eakin method and intrinsic uncertainty of model calibration.

Calibrating and revising a groundwater flow model, Shomaker (2010) [11] estimated groundwater recharge in the Salt Basin to be 61,723 acre-feet per year. An initial recharge estimate of 58,482 acre-feet per year was based on a conceptual recharge model that combined groundwater inflow from the Peñasco Basin, areal recharge (also called diffuse recharge) from the highlands of the Sacramento Mountains, and stormwater runoff infiltration along the flow paths of ephemeral arroyos [11]. However, this initial estimate did not account for potential groundwater discharge and required modifications. Shomaker (2010) [11] calibrated a more inclusive groundwater flow model for the entire Salt Basin using historic data and transient conditions. The second attempt to estimate recharge resulted in a range of recharge rates between 35,000 and 90,000 acre-feet per year [11]. The ultimate recharge estimate from Shomaker (2010) [11] was from a calibrated steady state groundwater flow model that assumed 1.5 percent of precipitation becomes recharge. This estimate included 5,451 acre-feet per year groundwater inflow from the Peñasco Basin, 40,888 acre-feet per year areal recharge, and 15,384 acre-feet per year of stormwater runoff infiltration. While this recharge estimate separates different types of recharge, which helps constrain sources of error and facilitates comparisons with other estimates using different methods, it is limited by the chosen model parameters and calibrations.

Daniel B. Stephens and Associates [25, 65] conducted two studies to estimate groundwater recharge in the Salt Basin that independently estimated 37,000 to 82,000 acre-feet per year and 26,710 acre-feet per year, respectively. DBS&A (2010a) [65] used a distributed-parameter water-balance model that was developed by Sandia National Laboratory for use at Yucca Mountain, Nevada. This

model accounts for precipitation, evapotranspiration, overland flow, and soil water storage [65]. The range of recharge quantities are the result of multiple tests for below-average, average, and above-average precipitation years based on the precipitation data collected in Dell City, Texas and Cloudcroft, New Mexico [65]. Mayer (1995) [40] and Hutchison (2008) [10] also used Nevada as a surrogate site, as assumption implicit in their use of the Maxey-Eakin method, which was first developed using data from Nevada, and which potentially overestimates recharge due to winter precipitation in Nevada. In contrast, use of the Yuca Mountain model introduces the assumption that the hydrological processes in the Salt Basin are similar to those in Nevada, which is a less stringent assumption than for the use of Maxey-Eakin. The second recharge estimate from DBS&A (2010b) [25] assumed that recharge into the basin was equal to the discharge of water via evaporation on the playas of the Salt Flats prior to anthropogenic alteration of the flow system. This method used geological rates of salt accumulation on the playa surface, which was controlled by the evaporation rate to infer groundwater recharge rates [25]. Salt accumulation rates were determined by dating cores of the evaporative sediment collected from the playa and by assuming a concentration of gypsum-forming minerals in the Salt Basin groundwater [25]. The concentration of gypsum-forming minerals, i.e. calcium and sulfate, was assumed to be 500 mg/L based on groundwater concentrations upgradient before evaporation occurred [25]. To make the conversion between evaporite depositional rates to groundwater recharge rates, DBS&A (2010b) [25] assumed that there was no runoff from the playa surface, loss of water through a different outlet that did not deposit evaporates, nor loss of evaporites from the playa. However, this assumption is invalid because the salt playas of the Salt Basin were the basis of the 1860's El Paso Salt War, in which salt was removed from the playas [60]. Some evaporites were removed from the playas during the historic timeline of the study and thus the evaporite depositional rates would reflect a slower deposition. Hence, the recharge estimate from DBS&A (2010b) [25] is likely an underestimate for the recharge rate of the Salt Basin. Combining the two recharge estimates and conceding the potential inaccuracy of each method, the recharge estimate of DBS&A (2010a) [65] and DBS&A (2010b) [25] is between 26,710 and 82,000 acre-feet per year.

Tillery (2011) [61] used a mean-annual streamflow method to estimate a flow of 60,414 acre-feet per year that has the potential to recharge the carbonate aquifers from within four of the major Salt Basin sub-basins. The mean-annual streamflow for the Piñon Creek, Sacramento River, Big Dog Canyon, and Cornucopia Draw sub-basins were estimated using an active channel geometry and a basin area analysis method. The channel geometry-based estimation used the average width of channels as calibration points to estimate the average amount of flow as a function of channel geometry. The relationship between active-channel width and mean annual discharge was estimated from a regression of gauged mountain-front streams from throughout southern New Mexico, most of which were perennial. Due to the semiarid environment, virtually all of the surface water in the Salt Basin is ephemeral. This difference in water systems means that the active-channel width method likely leads to an over-estimate of the actual

mean-annual streamflow. Further, the active-channel geometry method was calibrated using channel widths ranging from 15 to 55 feet. Some of the channels in the Salt Basin were outside of this range [61]. Tillery (2011) [61] also used a basin-surface-area regression analysis and found estimates similar to that of the active channel geometry method. This analysis utilized a regression of sub-basin surface area and average precipitation rate for the elevation against mean annual discharge, trained using the same southern New Mexico mountain-front streams. Since the sub-basins analyzed were outside the effective range of the method, there was a loss of sensitivity, and a potential underestimate of mean-annual streamflow [61]. The standard error of the basin regression was 46% compared to 29% for the active-channel width regression, leading Tillery (2011) [61] to prefer the active-channel method.

Sigstedt et al. (2016) [17] estimated a total recharge of 6,000 to 12,000 acre-feet per year. Due to the correlation between the groundwater age and increase in TDS concentrations along the groundwater flow path, geochemical modeling of the radiometric age of distinct flow path in the Salt Basin can be used to calibrate all of the flow paths throughout the northern basin [17]. The groundwater age from the ^{14}C specific activity can be further utilized to determine the groundwater flow rate. The flow rate for a distinct groundwater flow path is upscaled to the entire Salt Basin drainage area to produce a recharge estimate. Upscaling across the basin naturally introduces additional error to the recharge estimates, but utilizing the isotopic concentrations along the groundwater flow path helps account for the spatial variation in recharge.

1.6.4 Previous Hydrochemistry Analyses

Groundwater chemistry parameters reported by previous geochemistry studies of the Salt Basin and surrounding areas are typical for a carbonate aquifer system. The pH of the groundwater in the area is slightly alkaline and is naturally buffered due to the high concentrations of the bicarbonate anion [41, 74]. The local geology controls the water chemistry in the Salt Basin groundwater system, as dissolution of minerals such as halite, gypsum, and dolomite donate common major ions in the Salt Basin water system, including magnesium, potassium, and calcium [11, 13, 14, 23, 25, 41, 74]. The longer the water interacts with the surfaces of the minerals composing the aquifer, the greater the concentrations that result from dissolution of the minerals until the solution reaches equilibrium with the present minerals. Consequently, many of the major cations within the water system increase in concentration moving down the flow system, such as magnesium, potassium, and calcium [14]. As the groundwater moves towards the central Salt Basin, the cations move toward an equimolar calcium-to-magnesium ratio [17].

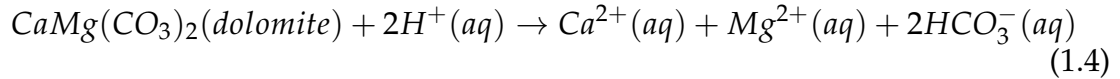
Specifically, the observed chemical changes are consistent with dedolomitization and gypsum dissolution as described in Back et al. (1983), Miller (1997),

Shomaker (2010), Sigstedt (2010) and Sigstedt et al., (2016) [11, 14, 17, 74, 75]. Meteoric water passing through a carbonate aquifer tends to dissolve calcite, dolomite, and gypsum. The rate of mineral dissolution depends on the geochemical dissolution kinetics of each mineral [17, 75]. Initially, gypsum, calcite, and dolomite dissolve congruently. Gypsum dissolves at a faster rate than calcite and dolomite, with the latter having the slowest dissolution rate. The dissolution of gypsum releases calcium ions into the water, which forces the incongruent precipitation of calcium carbonate in the form of calcite, which occurs at a faster rate than dolomite can precipitate. The rapid precipitation of calcite consumes carbonate, leading to undersaturation with respect to dolomite. This undersaturation with respect to dolomite was seen by Mayer (1995), Shomaker (2010), Sigstedt (2010), and Sigstedt et al. (2016) [11, 14, 17, 40] in groundwater samples from the high elevations of the Sacramento Mountains and into the Otero Break. That undersaturation of dolomite causes dolomite to dissolve, releasing magnesium and precipitating calcite; a process that is known as “dedolomitization”. Dedolomitization can be described with the following three chemical reactions and net reaction [75]:

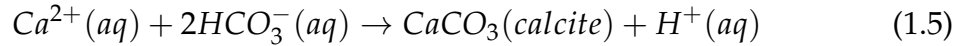
Gypsum dissolution and precipitation:



Dolomite dissolution:



Calcite precipitation:



Net dedolomitization reaction:



There is high potential for dedolomitization where there is a high magnesium-to-calcium ratio, as observed in the Salt Basin by Chapman (1984) [13]. The overall geochemical evolution of the groundwater results in an increase in sulfate from the gypsum and magnesium from the dolomite and a decrease in carbonate resulting from the incongruent precipitation of the calcite [17, 75]. This process also contributes to the alkaline pH of the carbonate waters (Miller, 1997). Sigstedt (2010) and Sigstedt et al. (2016) [14, 17, 74] observed a trend of dedolomitization in the groundwater samples moving from the northern Salt Basin towards the south (Figure 1.10; [12, 63, 64]). This figure only contains the well chemistry data from Sigstedt (2010) and Sigstedt et al. (2016) [14, 17] and is not fully representative of all geochemistry data for the Salt Basin.

Kreitler et al. (1986) [54] conducted a geological and hydrological study of the southwestern Salt Basin to determine a suitable potential location for an above-ground, low-level radioactive waste disposal facility. As previously mentioned,

the southwestern Salt Basin is the location of the Cretaceous Finlay limestone and Precambrian Pump Station Hills rhyolite porphyry. These geological units produced a unique chemistry. Kreitler et al. (1986) [54] found no trend in TDS distributions throughout the southwestern Salt Basin. Correspondingly, the chemical compositions of the groundwaters in this area were seemingly erratic and failed to show any chemical evolution moving down gradient. Further, there was no trend in tritium that could be used to identify recently recharged waters. Instead, there was tritium present in almost all groundwater samples, suggesting rapid recharge in the southwestern Salt Basin. The explanation for this anomalous chemistry from Kreitler et al. (1986) [54] referred to the coarsely and heterogeneously fractured geological facies. The fractures would produce an anisotropic fracture-controlled flow system that could contribute variable chemical constituents and support rapid recharge.

Due to the evaporative nature of the semiarid Salt Basin environment, the shallow aquifers and near-surface soils exhibit increased TDS concentrations as compared to the deeper alluvial-basin fill aquifers [13, 14, 40, 59, 74]. Water is pulled up from the saturated aquifer into the unsaturated vadose zone as a capillary fringe. Since there is a thick capillary fringe that is able to reach the surface in the area of the Salt Flats, there is a significant amount of water being delivered to the surface by capillarity and then evaporated [13]. This evaporation is effectively constant, with water continuously being pulled up through the vadose zone and evaporated away [13]. As the water moves through the subsurface, it transports solutes. Evaporation of the water near the surface causes an enrichment of ions and often mineral precipitation. Within the central basin, there is also an increase in chloride and sodium. The process adding the chloride and sodium to the groundwater is likely the back-mixing of evaporative brines, combining modern groundwater with brines that previously existed in the basin center that were enriched in chloride and sodium as a result of local halite dissolution [17].

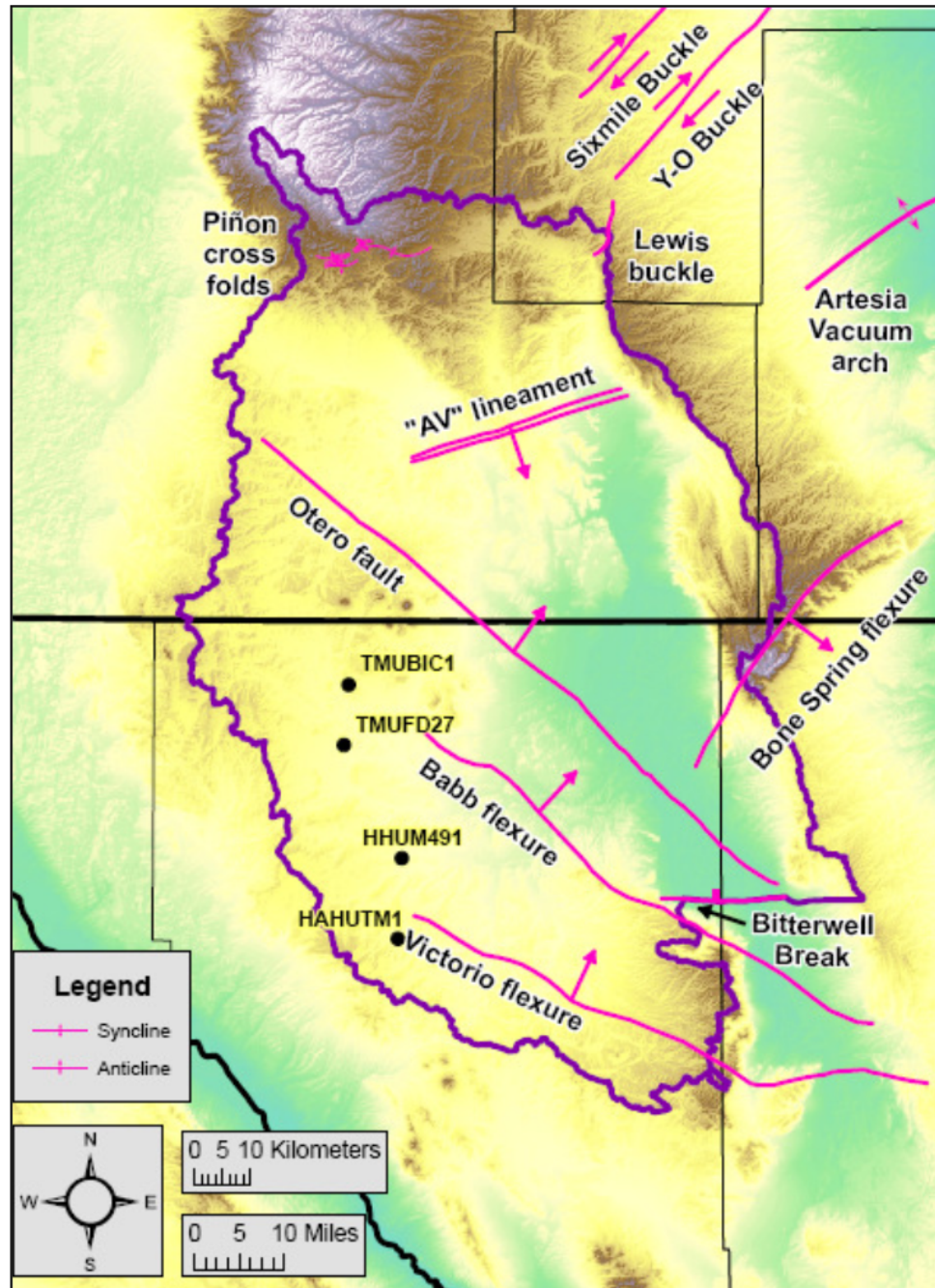


Figure 1.5: From [12]; Permian structural features; arrows indicate sense of displacement; bar on downthrown side of Bitterwell Break

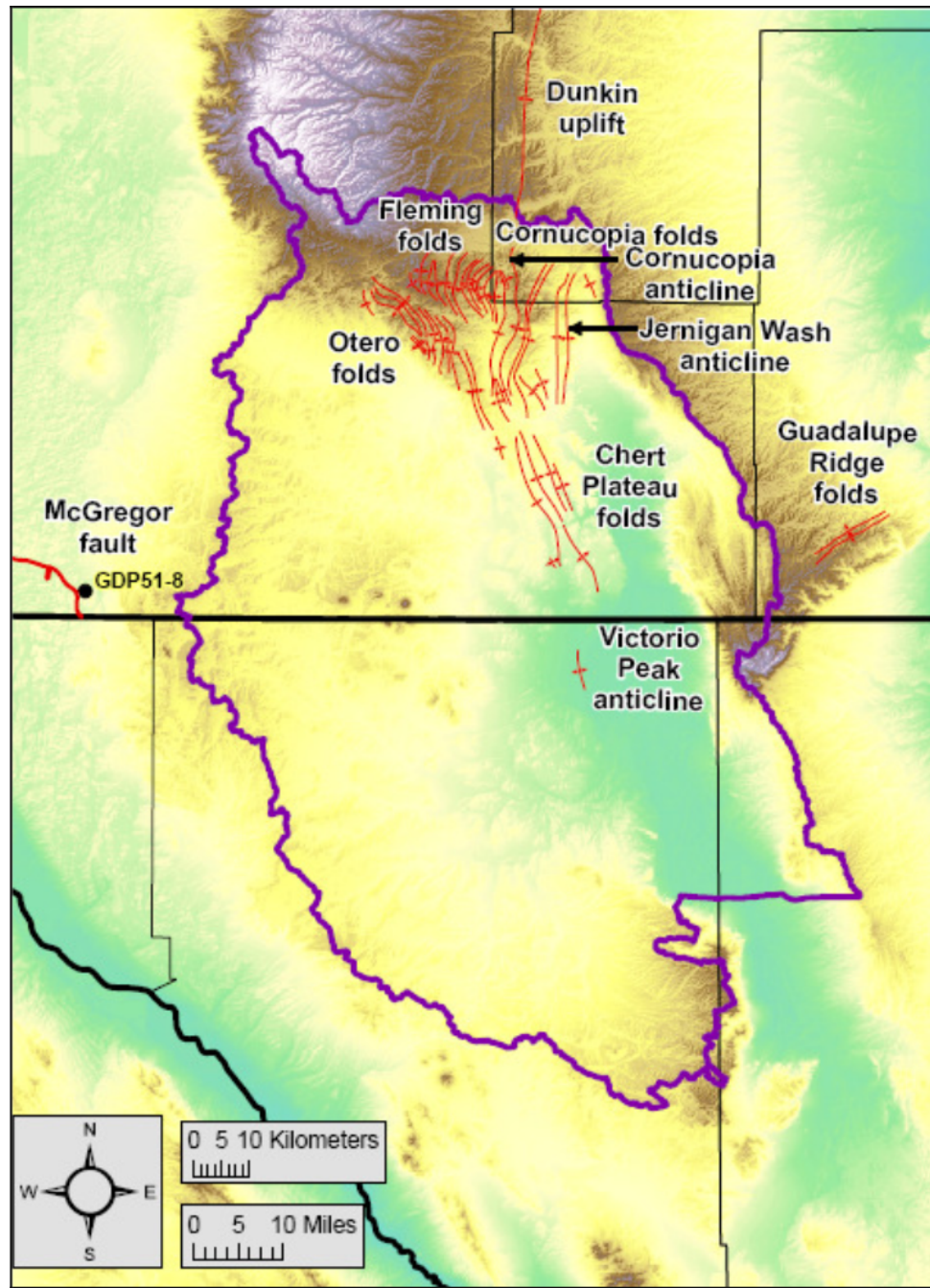


Figure 1.6: From [12]; Laramide structural features; bar on downthrown side of McGregor fault

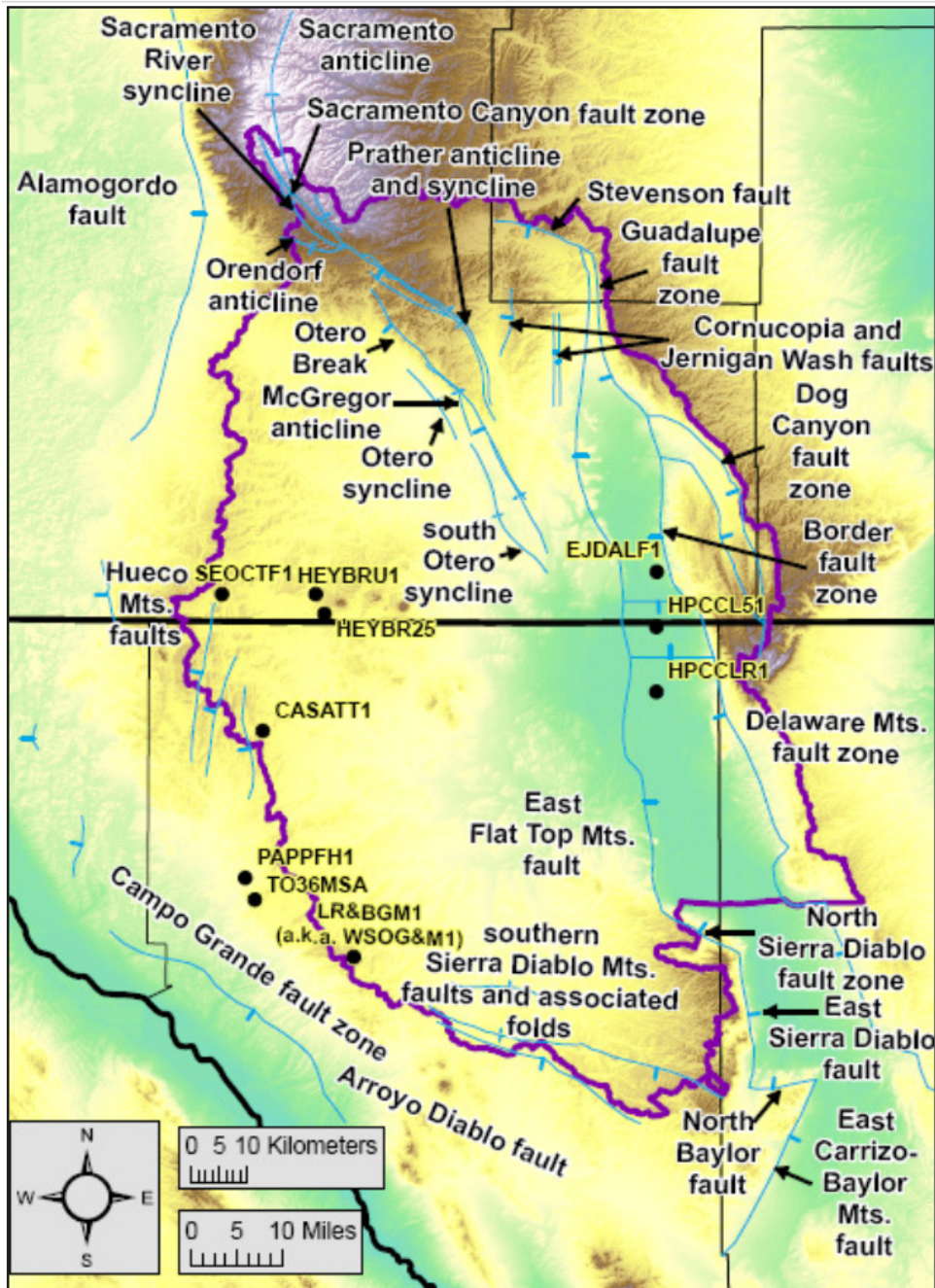


Figure 1.7: From [12]; Cenozoic structural features; bar on downthrown side of normal or high angle faults

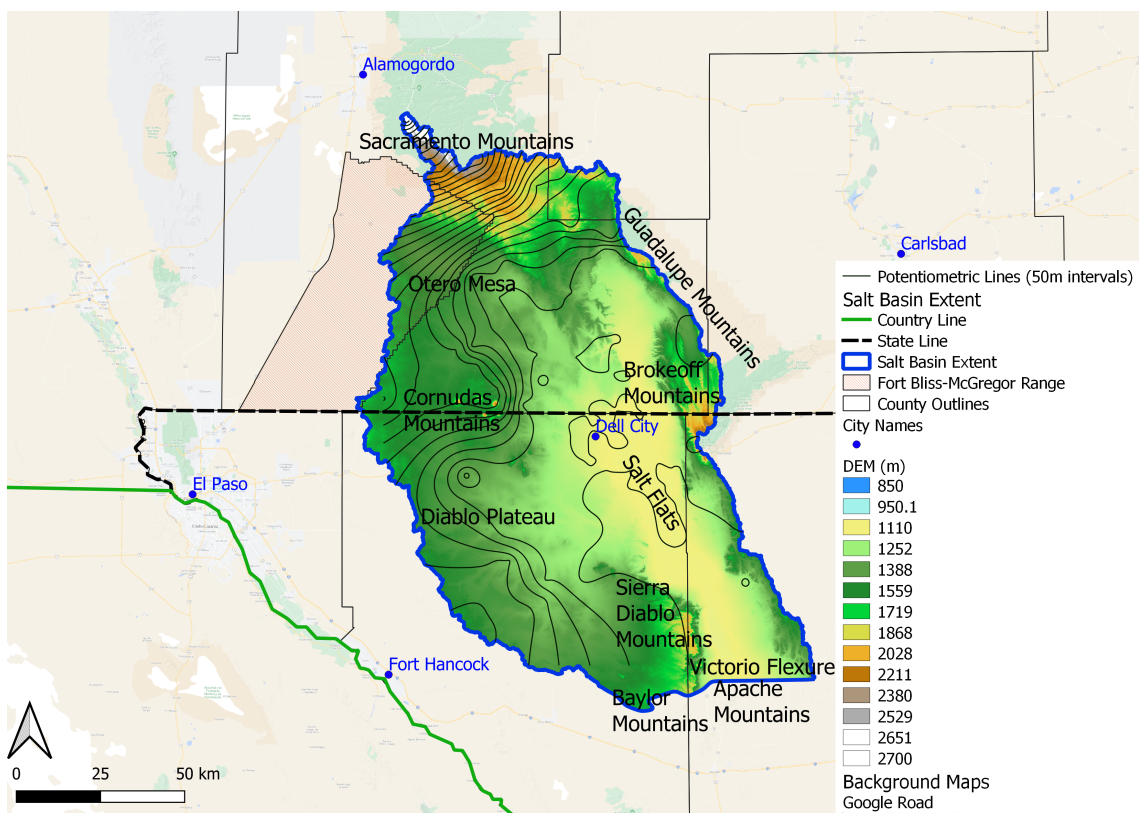


Figure 1.8: Observed potentiometric map of the salt Basin; lines are at 50m intervals

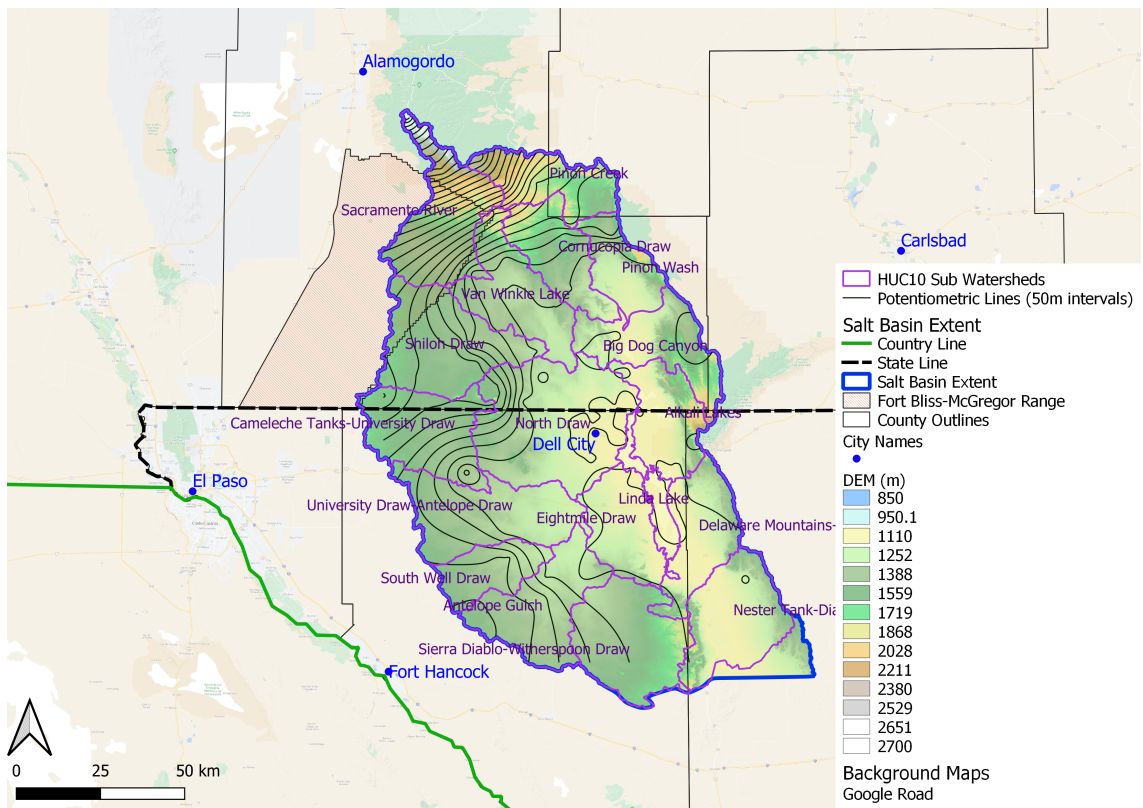


Figure 1.9: Salt Basin observed potentiometric surface map and HUC 10 sub-watersheds [68]; potentiometric intervals are 50m

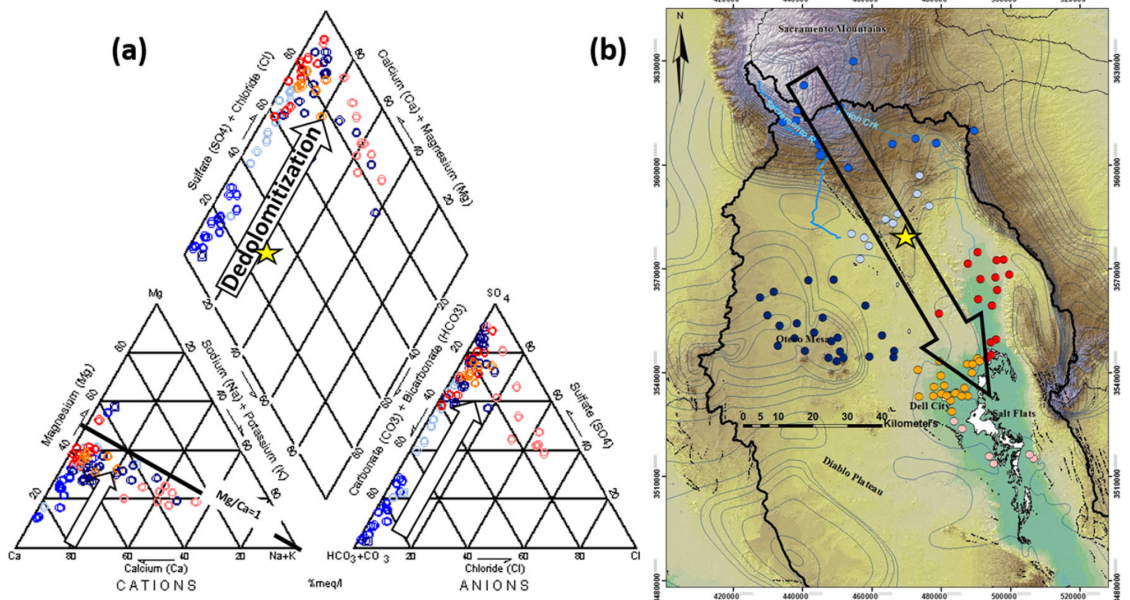


Figure 1.10: From [14, 17]; Reproduced in [31]; Piper diagram of Salt Basin chemistry from [14, 17] and spatial distribution of points along Piñon Creek; Piper diagram shows linear trend indicative of dedolomitization; star is an outlier point

CHAPTER 2

GROUNDWATER CHEMISTRY METHODS

2.1 Well Database

The scope of this project extends beyond a single field campaign. Consequently, historic hydrochemical data supplemented the data collected in conjunction with this study. Historic data came from multiple sources over more than 80 years. There are more than 800 groundwater samples from nearly 400 water wells throughout the Salt Basin that have been sampled and analyzed throughout the basin's history. These data are compiled in an open database through the New Mexico Bureau of Geology and Mineral Resources (NMBGMR; Aquifer Mapping Program) (Appendix A.1). The full data set was comprised of groundwater, spring, precipitation, and perennial stream water samples with major and minor elemental chemistry and environmental tracer analyses. The data included calcium, chloride, carbonate, bicarbonate, bromide, potassium, magnesium, sodium, sulfate, total dissolved solids, temperature, pH, $\delta^{13}\text{C}$, carbon-14, tritium, and oxygen-18. Figure 2.1 shows the spatial extent of the data within and around the Salt Basin.

2.2 Differentiation of Flow Paths/Geological Provinces

To better visualize the groundwater movement of the Salt Basin, the full hydrochemical dataset was separated by likely groundwater flow paths. These flow paths were based on surface water sub-watersheds and the observed groundwater potentiometric surface. Previous studies have delineated some New Mexican flow path watersheds (Sacramento River, Piñon Creek, Cornucopia Draw, and Big Dog Canyon) within the Salt Basin, as shown in Figure 2.2; [61]. The Sacramento River, Piñon Creek, and Cornucopia Draw flow paths were extended towards Dell City following the observed potentiometric surface. For the Texas portion of the Salt Basin, the flow paths were based on sub-watersheds and the observed potentiometric surface. For some chemical analyses, it was more convenient to separate the Salt Basin based on the dominant geology. The Salt Basin map (Figure 1.1) and surface geology map (Figure 1.2) were used to separate the geological provinces. The designation of flow paths and geological provinces allowed the massive data set to be condensed for more practical analyses. An additional benefit of the flow path separation is that it made it possible to make analogies between flow paths

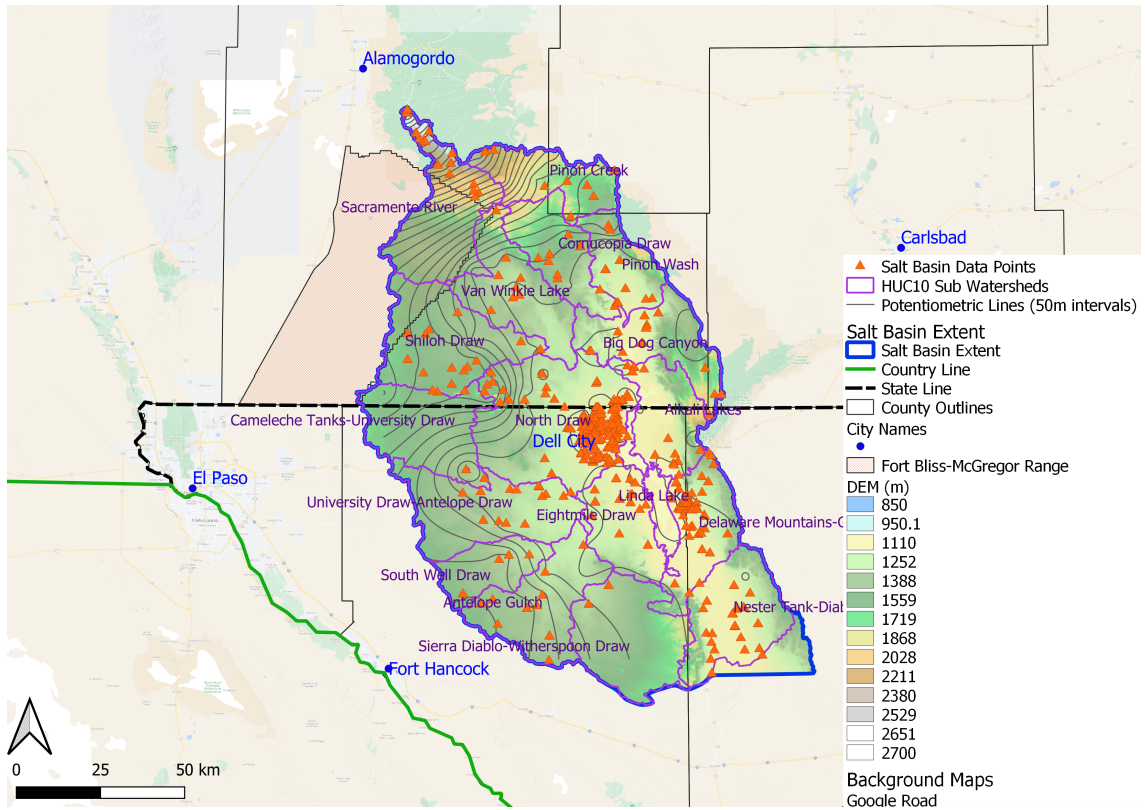


Figure 2.1: Salt Basin HUC 10 sub-watersheds, observed potentiometric surface map, and chemistry data points from Appendix A.1

with ample data to those with limited data. The geological provinces facilitated the comparison between chemical patterns and geological patterns.

2.3 Hydrochemical Evolution

Rarely are waters indistinguishable across landscapes. Commonly, waters gain constituents with distance from recharge areas due to mineral dissolution and confluence with other waters. This basic increase in constituent concentration along a flow path can be seen by plotting the given constituent or a ratio of two constituents on a map-view of the Salt Basin. From this aerial display, patterns of chemical evolution can be determined at a basin-wide scale. The level of chemical evolution between individual water sample points along a singular flow path can determine the effective processes of that flow path. In order to isolate that chemical evolution, a pair-wise matrix was created to plot every major constituent against one another. Trends between components suggest chemical connectivity and reactions. Chemical evolution was also evident in Piper diagrams. These diagrams are a graphical representation of major cations and anions within water

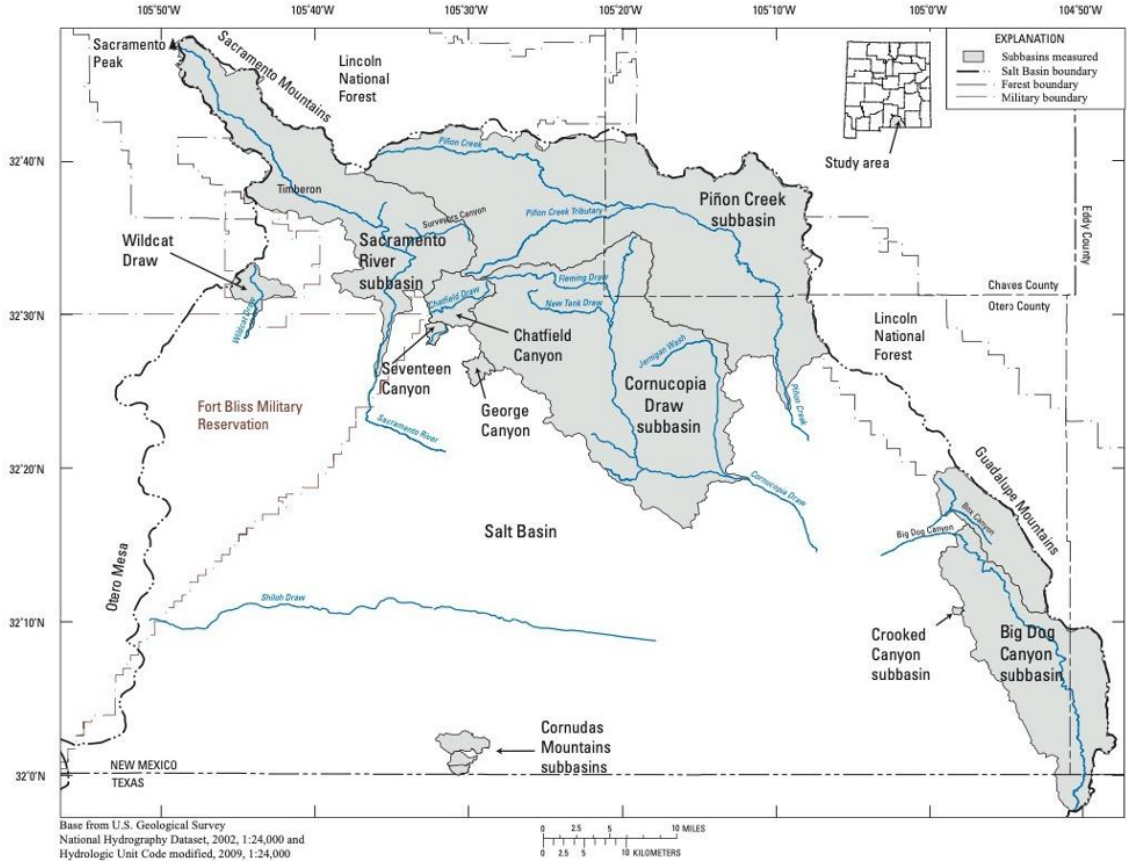


Figure 2.2: Salt Basin study area showing location of surface-water subbasins measured by Tillery (2011) [61]

samples. Each section of the diagram corresponds to a hydrochemical facies. Moving from facies to facies or staying within one facies has hydrochemical connotations.

It is important to understand the connection between the hydrochemistry and the underground geology that often sources additional constituents to the water. As limestones are the most common aquifer within the Salt Basin, it limits the chemical reactions that are probable. The majority of the groundwater will be neutral to slightly alkaline and likely have high total dissolved solids (TDS). Within this range of pH values, the majority of carbonate is in the form of bicarbonate.

2.3.1 Expected Hydrochemical Trends

Continuing an analysis of geological impacts on hydrochemical data, previous studies in the Salt Basin have found dedolomitization to be a dominant chemical evolution throughout the carbonate facies of the basin [11, 14, 17, 74].

This process is characterized by a dissolution of gypsum, calcite, and dolomite [75]. Referring to Figure 1.10, this chemical evolution appears in the Piper diagrams. Dedolomitization has a characteristic increase in sulfate and magnesium, a slight increase in calcium concentrations (moving towards a one-to-one ratio of calcium-to-magnesium), and a decrease in carbonate [17, 75]. These changes will be evident in the constituents' plot along the flow path. The one-to-one ratio of Ca/Mg will be evident in the ratio distribution map of Ca/Mg.

In the southwestern portion of the Salt Basin, Kreitler (1986) [54] noted a wide variability of chemical concentrations throughout Antelope Draw and South Well Draw. This range and lack of trends was contributed to highly fractured aquifers. It is expected that the lack of trend that Kreitler (1986) [54] found in the southwestern Salt Basin will be evident in the constituents' plot along the flow paths.

Brines mixing in from the Salt Flats/playas should contribute additional sodium and chloride to the groundwaters because the evaporites in the playas are primarily halite [25, 31, 58, 59]. This increase in sodium and chloride will be evident in the constituents' plot along the flow paths or with proximity to the playas. This change from a system dominated in sulfate to a system dominated in chloride will also be evident in the ratio distribution map of sulfate-to-chloride.

2.3.2 Hydrogen and Oxygen Evolution

Precipitation undergoes chemical evolution through different pathways as it becomes groundwater. Water is comprised on hydrogen and oxygen, but those elements have a range of isotopes. Hydrogen is usually found in the forms of hydrogen-1, usually shortened to hydrogen (H), or deuterium (D or ^2H). Oxygen is usually found in the forms of oxygen-16 (^{16}O) or oxygen-18 (^{18}O). The local meteoric water line (LMWL) is representative of the natural ranges of deuterium and oxygen-18 of local precipitation from summer to winter precipitation. Summer precipitation has waters characteristically enriched in deuterium and oxygen-18. Water containing hydrogen and oxygen-16 are preferentially evaporated with respect to waters with the heavier isotopes, deuterium and oxygen-18. However, warmer temperatures of summer cause more evaporation. Thus, waters with both the light and heavy isotopes of hydrogen and oxygen are added to the atmosphere to be rained out. In contrast, winter precipitation is characteristically depleted in deuterium and oxygen-18. Cooler temperatures produce less evaporation. With less evaporation, only the water with light isotopes, hydrogen and oxygen-16, are evaporated into the atmosphere to be rained out. This seasonal variability can be seen by plotting deuterium against oxygen-18 of the precipitation. Previous studies of the Salt Basin precipitation and groundwater show winter precipitation in the Sacramento Mountains being the source of the majority of recharge in the Salt Basin [9, 11, 13, 14, 16, 17, 24, 41, 65, 66].

Jasechko (2019) [76] discusses some of the major evolution pathways that affect deuterium and oxygen-18. Some of these pathways include evaporation,

mixing with fossil waters, or distal transport. In order to distinguish the different pathways of hydrological evolution, the delta concentrations of deuterium and oxygen in precipitation and groundwater are plotted and compared against the local meteoric water line. If there was no fractionation between precipitation and groundwater, the two data sets would be along the LMWL. Fractionation caused by evaporation will result in groundwaters with increased ^2H and further increased ^{18}O . Hence, the groundwater will be below the LMWL. Mixing with fossil waters that were precipitated under different climatic conditions will cause an increase of deuterium and an increase in oxygen-18 along the LMWL, but will be between the fossil water end member and the fresh precipitation end member. The LMWL trend is also shown with distal transport and the resulting water is between a distal end member and the fresh precipitation end member. The difference between the precipitation and groundwater delta values increasing as the process becomes more dominant.

2.4 Han Plots– Carbon Analysis

Dissolved inorganic carbon concentrations, carbon-13, and carbon-14 can be utilized as a tracer to determine dominant chemical evolution pathways. Han et al. (2012) [2] was used as the basis for carbon analysis. Hydrochemical data is plotted in three graphs, such as in Figure 2.3: i) $1/\text{DIC}$ versus $\delta^{13}\text{C}$, ii) $1/\text{DIC}$ versus ^{14}C , and iii) $\delta^{13}\text{C}$ versus ^{14}C . Dissolved inorganic carbon (DIC) in the form of bicarbonate was included in this analysis to differentiate source of carbon. The method described in Appendix A of Han et al. (2012) [2] was used to place the reference lines on these three plots to separate the carbon data into regions. The lines added to graph i and graph iii are dependent upon the measured soil carbon dioxide gas trapped in the groundwater when the system became closed [2]. The X and Z line represent process lines. The X line has constant $1/\text{DIC}$ in graph i and graph ii and constant $\delta^{13}\text{C}$ in graph iii, indicating radioactive decay of carbon-14 without exchanging inorganic carbon with another source, such as carbonates. The Z line follows geochemical evolutionary changes in radiocarbon, $\delta^{13}\text{C}$, and $1/\text{DIC}$ with no radiocarbon decay and assuming exchange with carbon-14 dead, solid carbonate minerals through time. The vertical line for $1/\text{DIC}$ and the diagonal “Z” line are estimated based on how the data plots within graph iii and assuming no additional reactions beyond inorganic carbon species changes have occurred within the closed system. The initial estimated value for the ^{14}C constant line is 50 percent modern carbon, assuming half of the radiocarbon has been released or decayed before the system closed. The initially estimated value for the $\delta^{13}\text{C}$ constant line is dependent upon the dominant vegetation type: between -30 and -20‰ for type C3 plants and between -20 and -15‰ for type C4 plants. These $\delta^{13}\text{C}$ concentrations are then divided in half to reflect the enrichment of $\delta^{13}\text{C}$ due to additional carbon introduced into groundwater system

with carbonate mineral dissolution and fractionation during the reactions from CO₂ gas to aqueous carbonate.

For the Han plots, the Salt Basin was divided into five groups corresponding to geologic provinces with carbon data. These geologic provinces are: NM Carbonates, TX Cretaceous, TX Victorio Peak, TX Capitan, and TX Salt Flats. The ¹⁴C and $\delta^{13}\text{C}$ of Salt Basin soil CO₂ was measured to be approximately 70 percent modern carbon and -22‰, respectively [20]. The $\delta^{13}\text{C}$ value was halved to adjust for carbonate dissolution, resulting in a constant $\delta^{13}\text{C}$ line of -11‰. Hence, the lines perpendicular to the appropriate axis was drawn at -11‰ for $\delta^{13}\text{C}$ and at 70 percent modern carbon for carbon-14. The $\delta^{13}\text{C}$ value was determined for the Sacramento Mountains. Assuming the majority of recharge occurs within these high elevations, the measured -11‰ for $\delta^{13}\text{C}$ is used for all of the flow paths/geological provinces. The southern Salt Basin did not have a measured soil CO₂ carbon-14. For this region and associated flow paths/geological provinces, the initially estimated value of 50 pmC was used for the constant ¹⁴C line. For the combination of the TX Cretaceous and TX Victorio Peak, an average value of 60 pmC was used for the constant carbon-14 line.

2.4.1 Expected Han Plots Trends

Each region and combination of regions of the three carbon graphs are associated to different fractionation pathways that can modify the relative concentrations of carbon.

Region 2 is representative of dedolomitization. This process is associated with low radiocarbon activities, low dissolved inorganic carbon, and enriched $\delta^{13}\text{C}$. As the gypsum and dolomite dissolve, the bicarbonate released enriches the solution in $\delta^{13}\text{C}$. The calcite precipitation preferentially incorporates the lighter dissolved inorganic carbon. Throughout this process, the radiocarbon decays and results in a low radiocarbon groundwater.

The overall process of incongruent dissolution is associated with the X(b) lines on graphs i and ii. Dedolomitization is an example of incongruent dissolution, where one mineral is dissolved into solution and another mineral is precipitated out. The X(b) line is also associated with isotopic exchange between water and carbonates. This reaction does not change the 1/DIC. The reaction exchanges radiocarbon and/or carbon-13 for carbon-12, which changes the percent modern carbon of radiocarbon and $\delta^{13}\text{C}$ in the groundwaters.

Region 6 is not specifically connected with any one process. Instead, region 6 is representative of multiple processes, including incongruent dissolution, isotopic exchange, radiocarbon decay, and mixing. Interpretation of data points within this region depend upon where the points are on graph i and graph ii.

Points that are not along process lines or have a distribution within a shaded region are likely caused by mixing processes and multiple water sources. A full

summary of these regions, lines, and combined regions, as well as the associated reactions, can be found in Han et al. (2012)[2].

2.5 Radiocarbon Corrections

The radioactive decay of radiocarbon (carbon-14 or ^{14}C) can be utilized to estimate the average subsurface residence time of the groundwater. In order to convert from measured and initial carbon-14 activities to groundwater age in years, the following equation was used

$$t = \frac{-5730}{\ln(2)} \ln\left(\frac{^{14}\text{C}_{initial}}{^{14}\text{C}_{measured}}\right) \quad (2.1)$$

Generally, older waters have lower radiocarbon activities. However, this age-dating requires knowledge of the ^{14}C initial activity. The initial concentration of radiocarbon can vary depending upon physical and chemical processes [2]. Depending upon the dominant processes, there are some potential corrections that can be applied to the measured activity. Referring to Figure 2.3 and Han et al. (2012) [2], it is possible to determine the dominant pathways and correct for those changes.

As mentioned previously, dedolomitization is likely a dominant alteration process in the Salt Basin [11, 14, 17, 74]. This process corresponds to Region 2 of Figure 2.3. Sigstedt (2010) [14] performed a radiocarbon correction for dedolomitization along the Piñon Creek flow path. Those results will be discussed in further detail later.

A general correction model, the Fontes and Garnier model, was applied to all of the carbon data points within the Salt Basin [18]. The Fontes and Garnier model adds an isotopic exchange correction factor onto the Tamers radiocarbon equation. Using sample pH to determine the amount of carbon-14 within the total dissolved carbon content, the Tamers equation is

$$A_{o,Tamers} = \frac{2(10^{-pH}) + 10^{-6.3}}{2(10^{-pH} + 10^{-6.3} + 10^{-10.3+pH-6.3})} \times 100 \quad (2.2)$$

Adding the correction term onto this, the Fontes and Garnier full equation is given as

$$A_{o,F&G} = A_{o,Tamers} + (A_g - 0.2\epsilon - A_M) \frac{\delta_T - \frac{C_M}{C_T} \delta_M - (1 - \frac{C_M}{C_T}) \delta_g}{\delta_g - \epsilon - \delta_M} \quad (2.3)$$

The radiocarbon activity of the soil gas (A_g) and the average radiocarbon activity of dissolving carbonate minerals (A_M) are given in percent modern carbon

(pmC). The additive fractionation factor (ϵ), the total $\delta^{13}\text{C}$ of the sample (δ_T), the $\delta^{13}\text{C}$ of the carbonate minerals (δ_M), and the $\delta^{13}\text{C}$ of the soil gas (δ_g) are given in per mil. Lastly, the concentration of carbon from carbonate mineral dissolution (C_M) and the concentration of total DIC in the groundwater sample (C_T) are given in mmol/L. Table 2.1 has a summary of these variables. The corrected initial activity of carbon-14 is dependent upon the sample pH, measured ^{14}C activity, and the concentrations of DIC and $\delta^{13}\text{C}$ in the sample, soil gas, and carbonate minerals. This corrected initial activity was used in the radiocarbon age equation to get a groundwater age that has been corrected to pH and isotopic exchange. Since this correction was not specific to any geological province or chemical process beyond isotopic exchange, there is limited reliability in these corrected radiocarbon ages, specifically where there is dedolomitization occurring.

Variable	Definition	Units
A_g	radiocarbon activity of CO_2 gas in soil	pmC
ϵ	additive fractionation factor	per mil, ‰
A_M	average radiocarbon activity of dissolving carbonate mineral	pmC
δ_T	total $\delta^{13}\text{C}$ of sample	per mil, ‰
C_M	concentration of carbon from carbonate mineral dissolution	mmol/L
C_T	concentration of total DIC in groundwater sample	mmol/L
δ_M	$\delta^{13}\text{C}$ of carbonate minerals	per mil, ‰
δ_g	$\delta^{13}\text{C}$ of soil CO_2 gas	per mil, ‰

Table 2.1: Fontes and Garnier radiocarbon full equation variables [18]

There is a possibility that the heterogeneous fractures of the southwestern Salt Basin cause a mixing of young and old waters and thus would effectively negate the use of the Fontes and Garnier radiocarbon correction [18]. Hence, a simple mixing model between a young and an old end member could better represent this heterogeneous flow system. An equation to represent this mixing is

$$A_{o,mixing} = \frac{^{14}\text{C}_{measured} - ^{14}\text{C}_{old}(1-f)}{f} \quad (2.4)$$

where

$$f = \frac{\left(\frac{Ca}{Na}\right)_{measured} - \left(\frac{Ca}{Na}\right)_{old}}{\left(\frac{Ca}{Na}\right)_{young} - \left(\frac{Ca}{Na}\right)_{old}} \quad (2.5)$$

With the correction factor (f), the corrected initial radiocarbon activity is calculated from the measured radiocarbon activity. The correction factor in this mixing model utilized calcium to sodium ratios of waters with high and low concentrations of measured radiocarbon activities. These ratios of calcium to sodium would also designate fresh and recently recharged precipitation versus saline and old waters. Just as the Fontes and Garnier corrected initial activity was put into the radiocarbon age equation to calculate a corrected groundwater age, the corrected initial activity from this mixing model was used to calculate a corrected groundwater age for the southwestern Salt Basin.

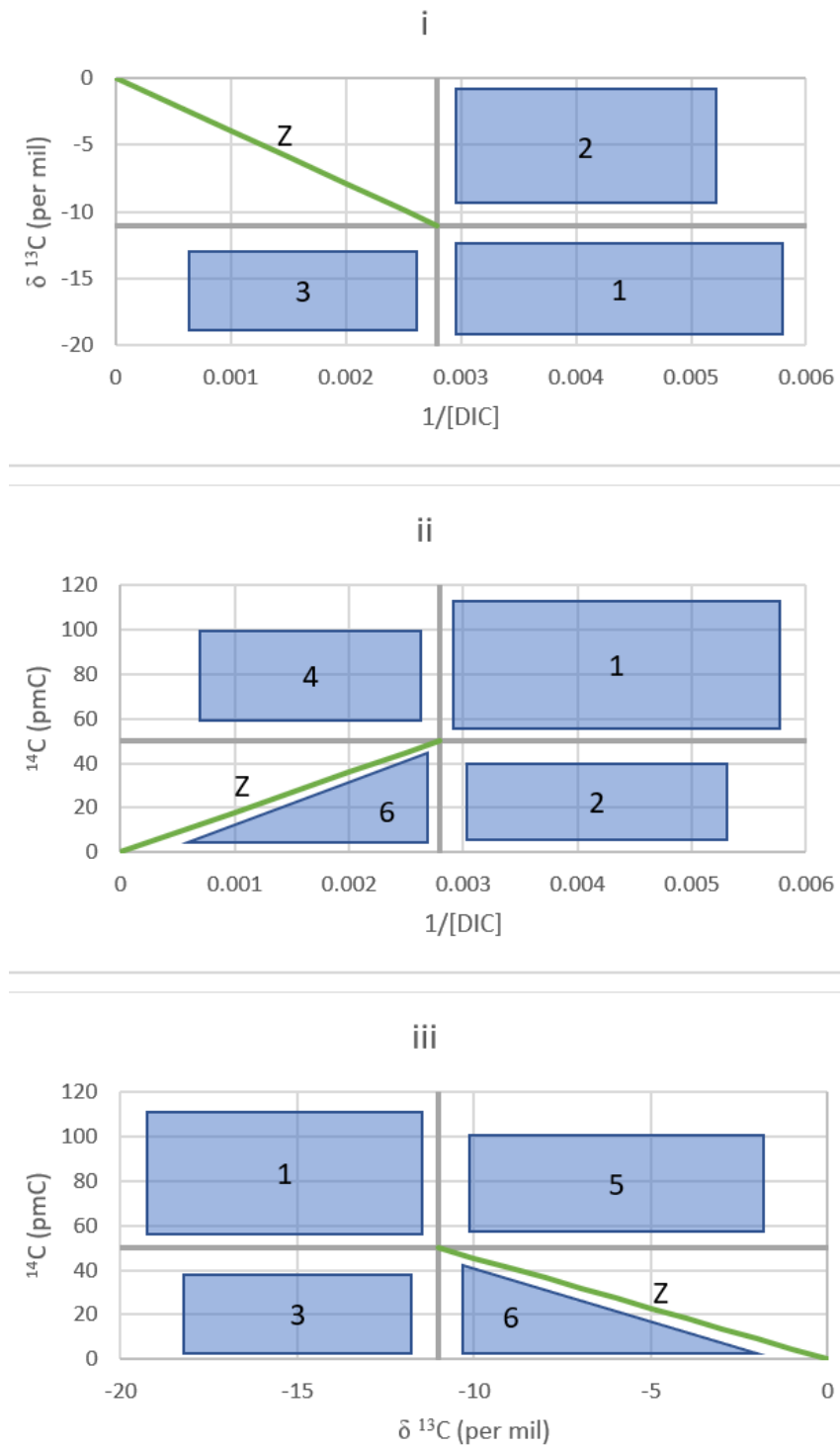


Figure 2.3: Recreated from [2]; Three graphical constructs to interpret carbon data (regions are highlighted and labeled based on dominant processes associated with each region, refer to [2] for further explanation

CHAPTER 3

GROUNDWATER CHEMISTRY RESULTS

3.1 Basin-Wide

The delineation of groundwater flow paths in the Salt Basin closely followed the sub-watersheds and groundwater potentiometric surface and resulted in ten major flow paths (Figure 3.1). Geological provinces were separated into seven provinces to group similar geologic facies with adjacent flow paths (Figure 3.2). While individual flow paths and geological provinces were closely analyzed independently, the overall Salt Basin chemistry was also reviewed to determine if there were any basin-wide dominant chemical evolution processes.

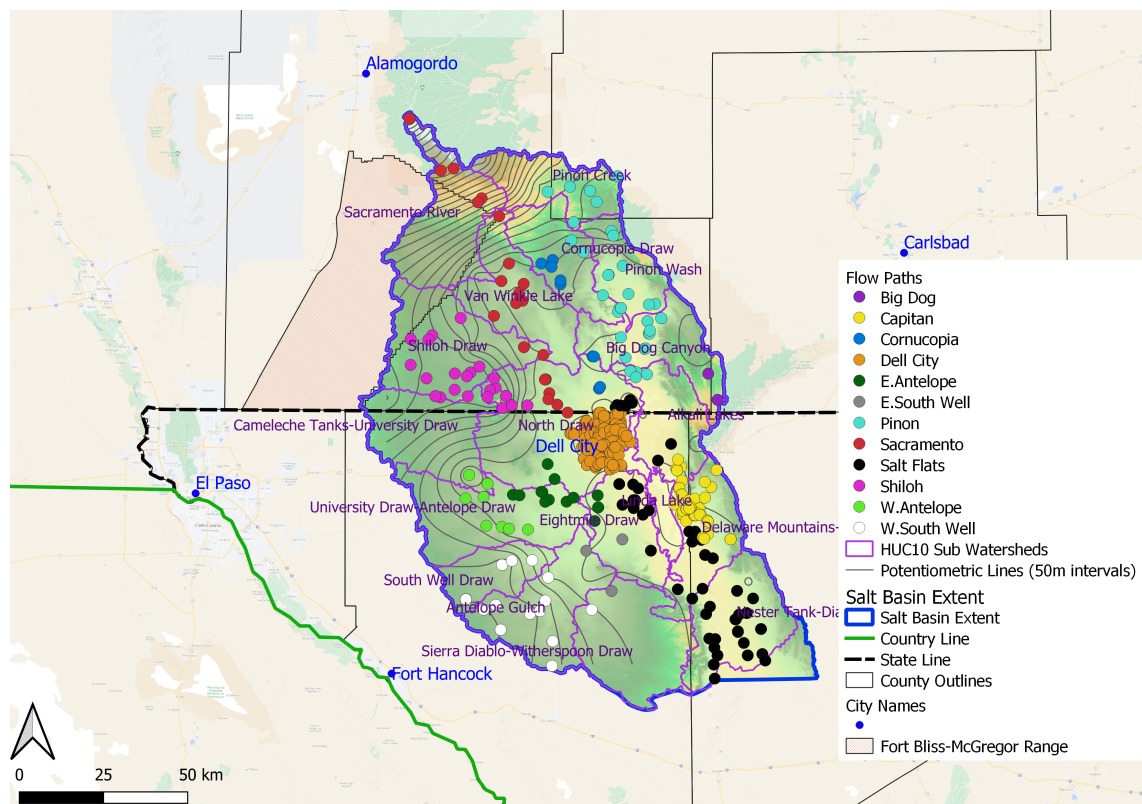


Figure 3.1: Salt Basin hydrochemistry points, color-coded by flow path

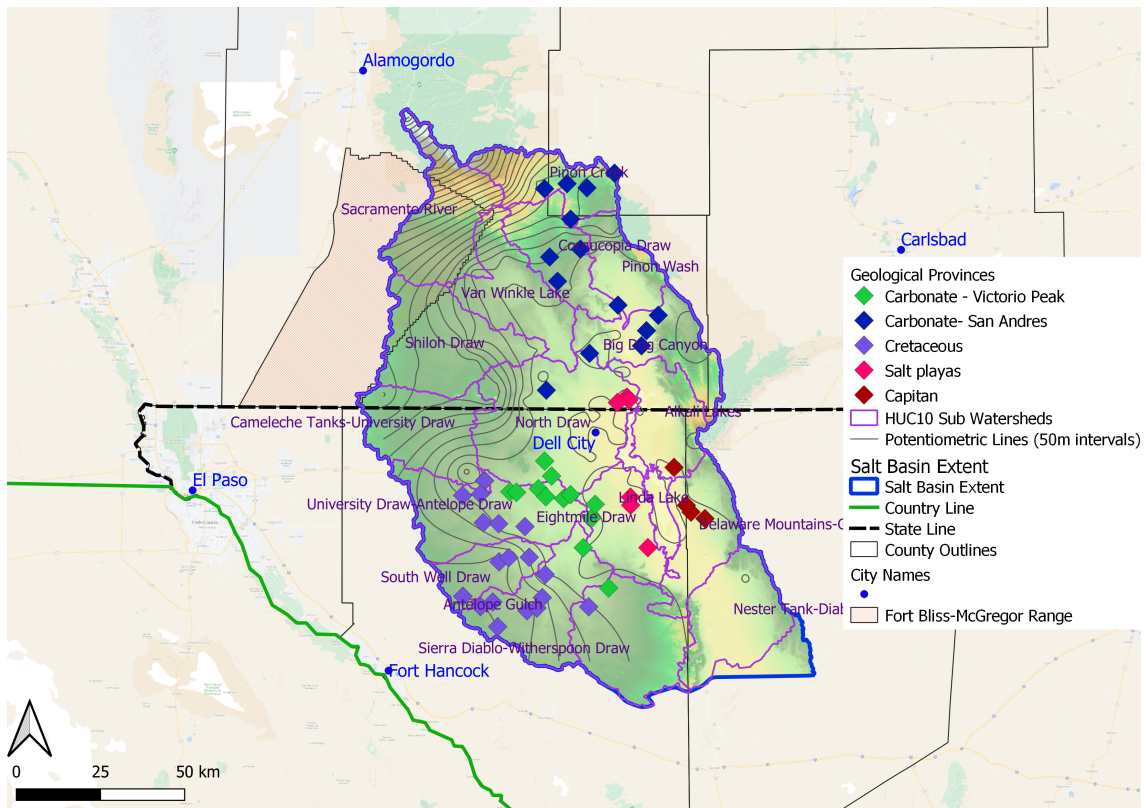


Figure 3.2: Salt Basin hydrochemistry points, color-coded by geologic province

3.1.1 Basin-Wide– Hydrochemical Trends

To encompass the major ions that are expected in this primarily carbonate system, the mapped chemical ratios of mmol/L to mmol/L were sulfate-to-chloride, calcium-to-magnesium and sodium-to-magnesium. The sulfate-to-chloride ratio shows sulfate dominance in the northern Salt Basin (Figure 3.3). Chloride generally becomes increasingly prevalent moving southwards. There is an anomalously high chloride dominated groundwater sample in the high elevations of the Sacramento Mountains. Dell City, TX has a clear transition from sulfate-dominated groundwaters to chloride-dominated groundwaters moving southwards. There are a few areas in the southern Salt Basin that still contain high ratios of sulfate-to-chloride, most evidently along the Salt Flats along the southern Salt Basin margin. Antelope Draw and South Well Draw also contain intermediate sulfate-to-chloride ratios

A trend in calcium-to-magnesium ratios is less prominent, but still shows a general increase in calcium moving southwards (Figure 3.4). The high elevations of the Sacramento Mountains are calcium dominated. Shiloh Draw, Dell City, and the Salt Flats each show a mixture of calcium-to-magnesium ratios, calcium-rich ratios, and magnesium-rich ratios. The Sacramento River, Piñon Creek, and Cornucopia

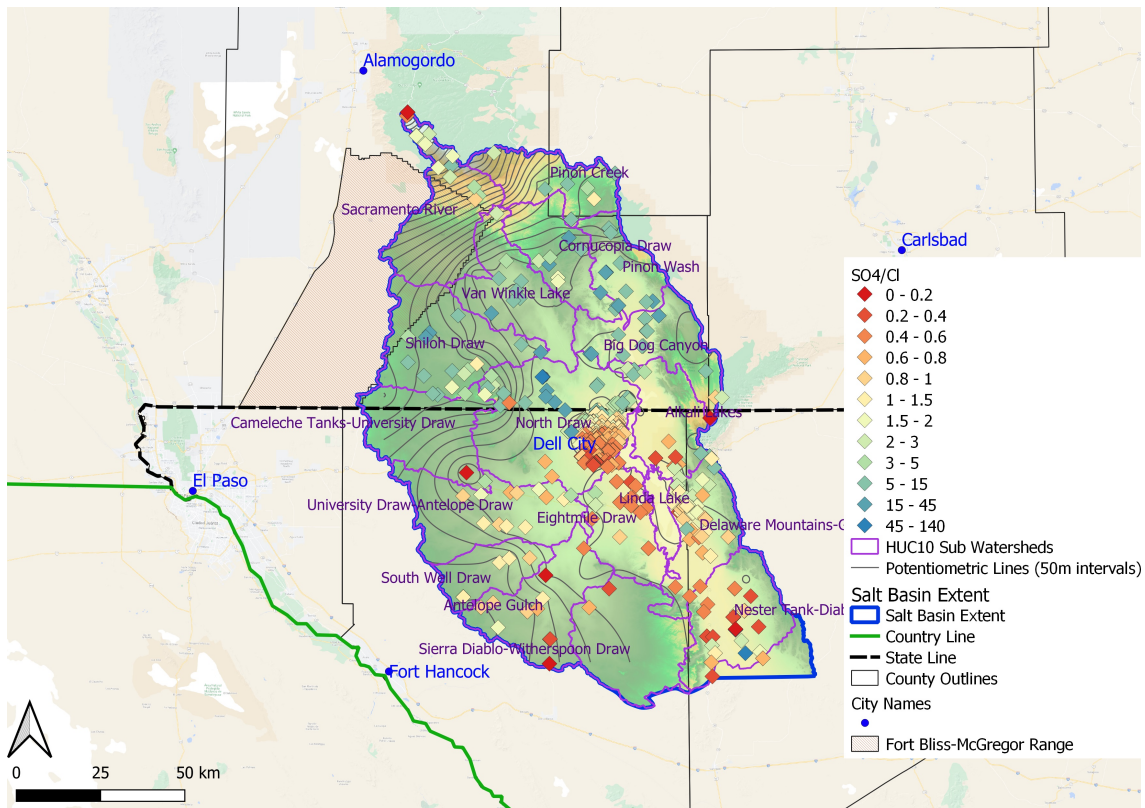


Figure 3.3: Salt Basin hydrochemistry points, color-coded by sulfate-to-chloride ratios of mmol/L:mmol/L; points dominated by chloride are more red

Draw flow paths tend to be higher in calcium, compared to the Antelope Draw and South Well Draw flow paths.

Sodium-to-magnesium ratios follow the same trend as sulfate-to-chloride, with a general increase in sodium moving southwards (Figure 3.5). The New Mexico portion of the Salt Basin is dominated by high magnesium. There are a few points with high sodium around the Cornudas Mountains within Shiloh Draw. Another area with high magnesium appears around the Capitan flow path along the eastern Salt Basin margin. Like with the sulfate-to-chloride ratio, Dell City, TX shows a clear transition between magnesium-dominated groundwaters changing to sodium-dominated groundwaters moving southwards.

Groundwater and precipitation deuterium and oxygen-18 isotopic compositions from the Salt Basin are plotted together to visualize the transition between the two waters (Figure 3.6). Average precipitation is around -70‰ δD and -11‰ δ¹⁸O. Average groundwater is around -60‰ δD and -9‰ δ¹⁸O. There is a wide distribution of precipitation values. Groundwaters are more concentrated around the average. Overall, the groundwater is more enriched than the precipitation. Due to additional oxygen-18, the groundwater average is below the precipitation LMWL. Figure 3.7 shows the distribution of the groundwater points and the corre-

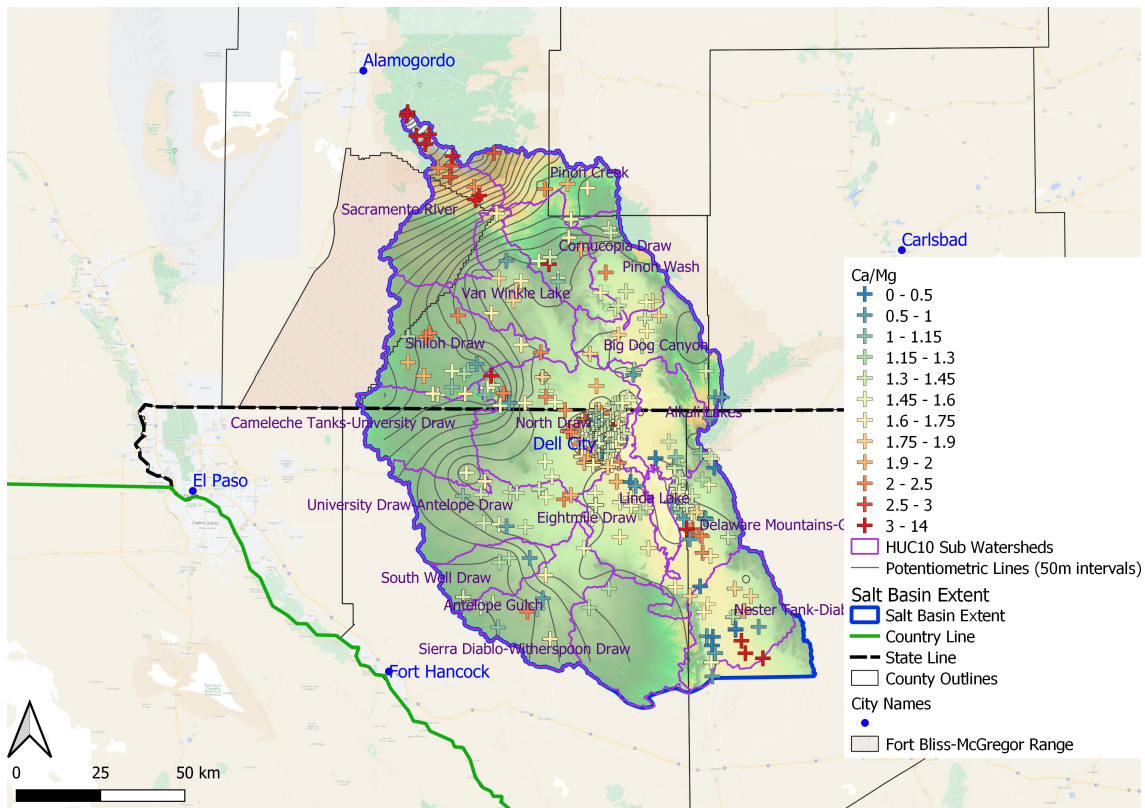


Figure 3.4: Salt Basin hydrochemistry points, color-coded by calcium-to-magnesium ratios of mmol/L:mmol/L; points dominated by calcium are more red

sponding $\delta^{18}\text{O}$. Spatially, there are no clear trends in $\delta^{18}\text{O}$. If there were continuous evaporation along flow paths, the result would be increasing values moving from the headwaters toward the Salt Flats. Flow paths with constant $\delta^{18}\text{O}$ values are indicative of limited or no isotopic fractionation within the aquifer. Where local recharge occurs, for example focused recharge from arroyo bed infiltration, the groundwater may gain the signature of the infiltrating summer monsoon stormwater. But this precipitated water may have a wide range of $\delta^{18}\text{O}$ values (Figure 3.6). There are few, if any, clear patterns in Figure 3.7, though the low $\delta^{18}\text{O}$ values in the Sacramento Mountains are consistent with snowmelt-derived recharge in that mountain range.

3.1.2 Basin-Wide– Han Plots

Plotting all of the Salt Basin carbon data onto one set of Han plots can be used to highlight the major basin-wide processes (Figure 3.8). The carbon points are primarily within Region 2 and Region 6, with a few points in Region 4 and Region

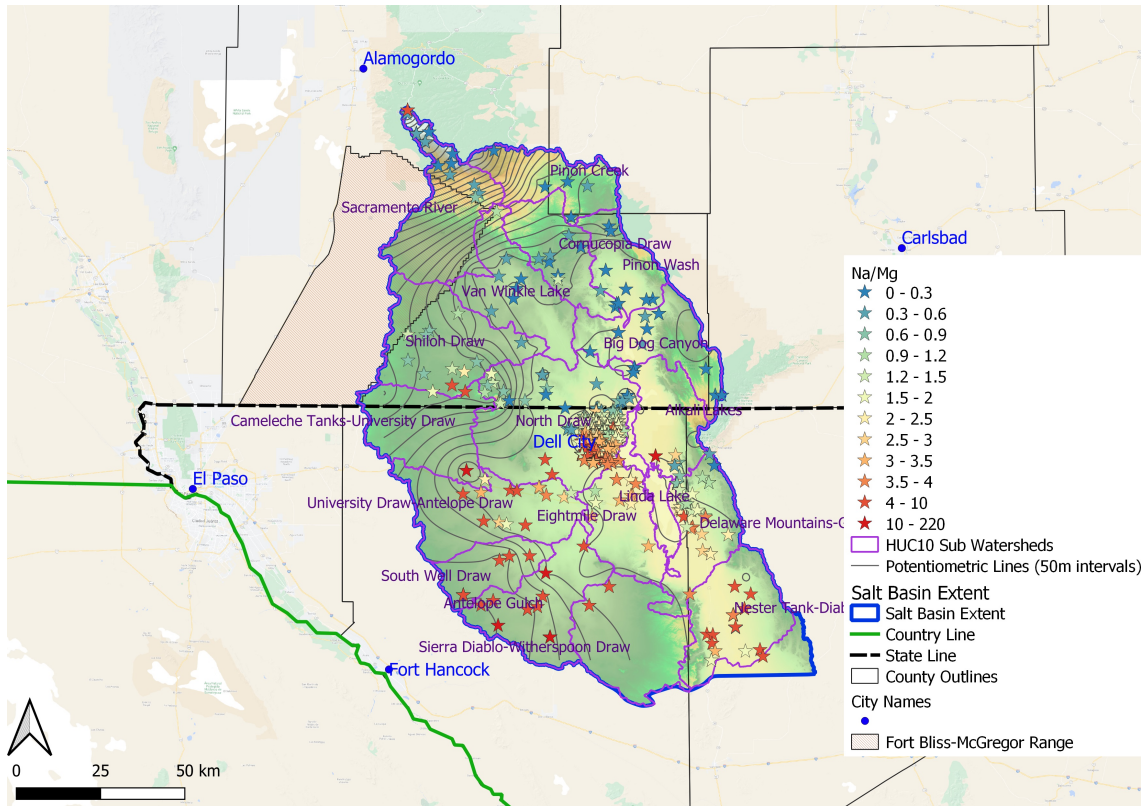


Figure 3.5: Salt Basin hydrochemistry points, color-coded by sodium-to-magnesium ratios of mmol/L:mmol/L; points dominated by sodium are more red

1. Region 2 and Region 6 are associated with dedolomitization, incongruent dissolution, isotopic exchange, radiocarbon decay, and mixing [2]. Region 4 and Region 1 are associated with methanogenesis and degassing, respectively [2]). However, upon further inspection and realignment of the constant lines based on hydrogeologic region-specific data, the point in Region 4 is relocated into Region 6. The point in Region 1 is given an alternative explanation for its positioning. Nonetheless, the basin-wide Han plots make it difficult to see where and why each process is occurring. Hence, the Han plots are separated by geological province to give spatial context to each of the processes.

3.1.3 Basin-Wide– Radiocarbon Analyses

The Fontes and Garnier correction method was applied to the basin-wide carbon data points to correct for isotopic exchange (Table 3.1). Table 3.2 shows the values used for the environmental parameters in the Fontes and Garnier equation and from Table 2.1. The radiocarbon value for soil gas was set to 100 percent

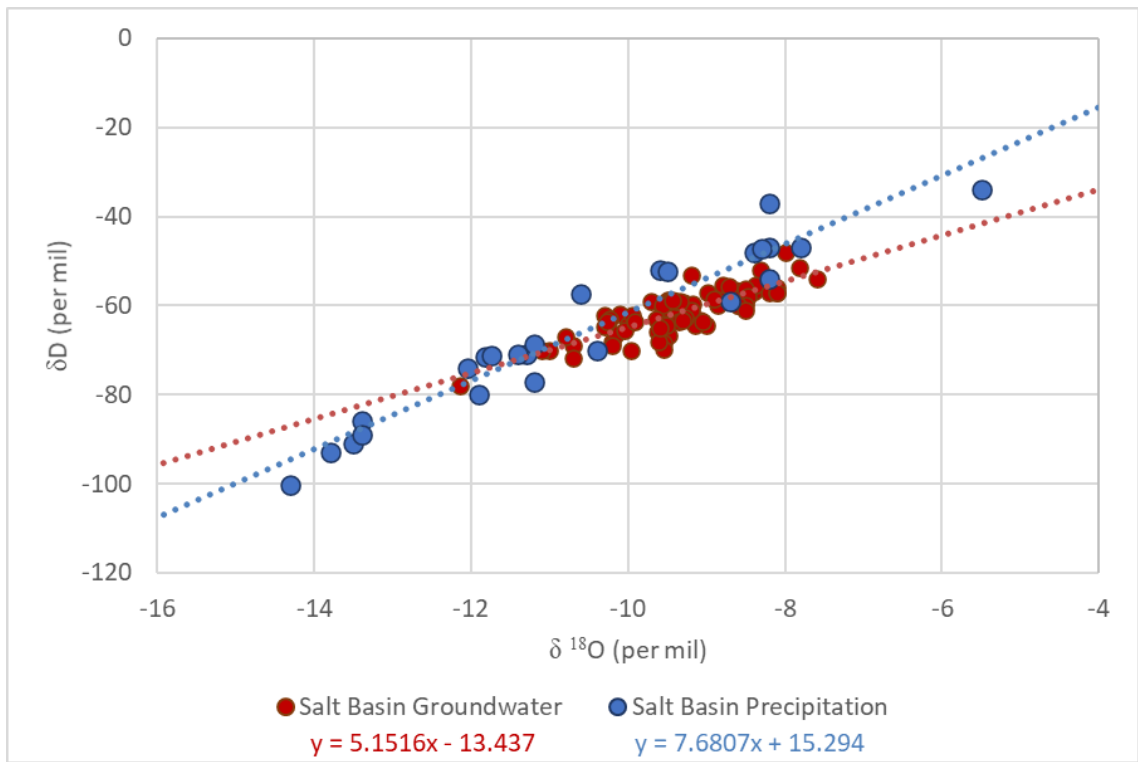


Figure 3.6: Salt Basin precipitation and groundwater deuterium and $\delta^{18}\text{O}$ values; trend line equations are provided in respective colors beneath the legend

modern carbon. The radiocarbon value for the dissolving carbonate minerals was set to 0 percent modern carbon. The additive fraction factor was set to -10 per mil. From Sigstedt (2010) [14], the $\delta^{13}\text{C}$ of the carbonate minerals was set to 5.7 per mil. From Morse (2010) [20], the $\delta^{13}\text{C}$ of the soil gas was set to -22 per mil.

However, this general correction method and the resulting groundwater ages lack geological and spatial connection. Instead of the F&G corrected radiocarbon ages, the measured radiocarbon activities were used as a basis for general age trends. Figure 3.9 shows the basin-wide measured radiocarbon activities in percent modern carbon. Subsequent geologic provinces will have province-specific corrected groundwater ages. There is an overall trend of decreasing radiocarbon activities moving southwards through the Salt Basin, which usually correspond to older waters. Radiocarbon activities are listed in Appendix A.1. There is a general trend towards older corrected ages with lower measured radiocarbon activities and lighter $\delta^{13}\text{C}$ (Figure 3.10). $\delta^{13}\text{C}$ ranges from -10.7 to -2.7‰ (Table 3.2).

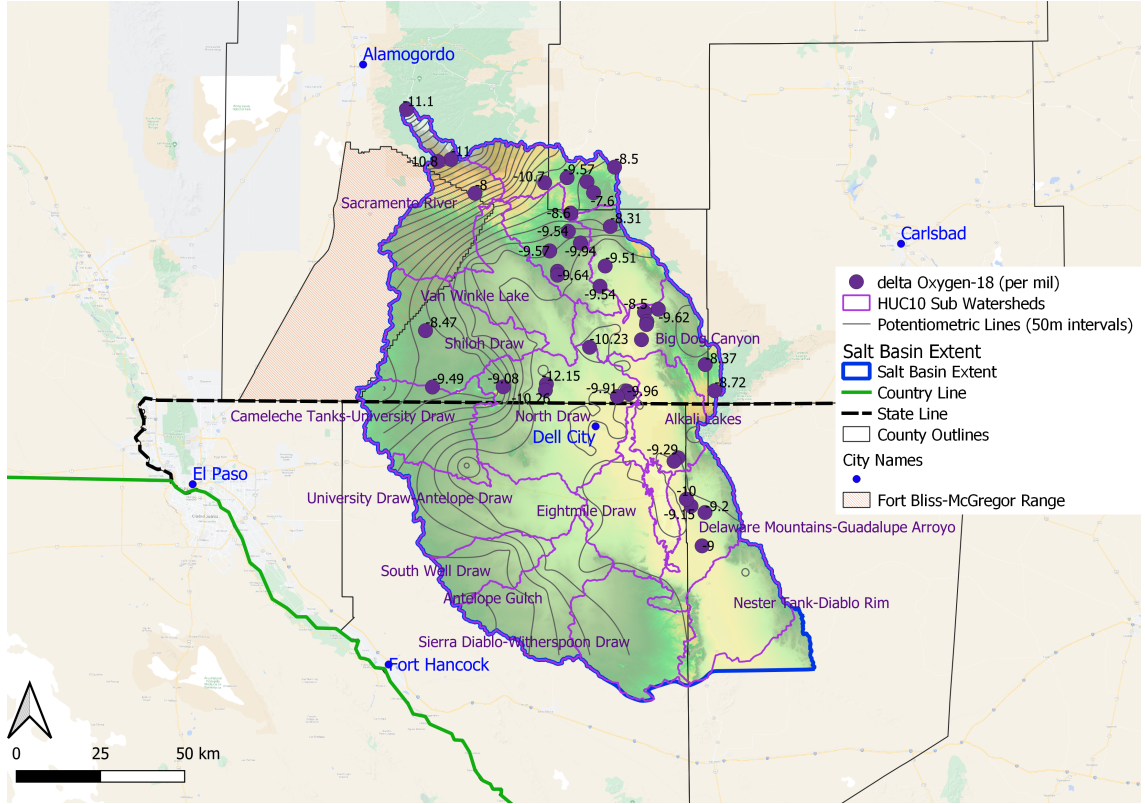


Figure 3.7: Salt Basin $\delta^{18}\text{O}$ points (per mil)

3.2 New Mexico– Carbonates Province

The New Mexico carbonate province contains the Yeso and San Andres carbonates. The Yeso formation is characterized as limestone and dolomite interbedded with gypsum, siltstone, and shale [14, 31, 45, 46]. The San Andres formation is characterized as dolomites interbedded with shale and sandstone [14, 31, 46]. Within this geological province, there are four major flow paths: Piñon Creek, Cornucopia Draw, Sacramento River, and Shiloh Draw. The Cornudas Mountains igneous intrusion is also contained within Shiloh Draw. These flow paths flow through the New Mexico Carbonate province before moving through Dell City, TX and discharging into the Salt Flats province. These connections will be discussed in further detail later.

3.2.1 NM Carbonates– Hydrochemical Trends

The Piñon Creek is dominated by calcium and sulfate, both showing an increase along the flow path (Figure 3.11a). Counter to a slight increase in magnesium, there is a slight decrease in bicarbonate. There is some variability in

the constituents moving southwards, but there is a general trend towards higher constituent concentrations in the south. There is minimal sodium and potassium throughout the Piñon Creek. On the Piper diagram, the flow direction is designated by the red arrows. The beginning of the Piñon Creek flow path has high bicarbonate, low chloride, low sulfate, a mixture between calcium and magnesium, and low sodium and potassium. The end of the flow path has low bicarbonate, low chloride, high sulfate, a mixture between calcium and magnesium, and low sodium and potassium. The average calcium-to-magnesium ratio is approximately one-to-one.

The Sacramento River is also dominated by calcium and sulfate, both showing an increase along the flow path (Figure 3.12a). While the remainder of the constituents increase, there is a decrease in bicarbonate moving towards the south. There is minimal sodium and potassium throughout the entire flow regime. A third of the way along the flow path, there is a slight decrease in constituents. This deficit is replenished and compounded further southwards. The arrows on the Piper diagrams designate flow from north to south. The beginning of the Sacramento River flow path has high bicarbonate, low chloride, low sulfate, with intermediate concentrations of calcium and magnesium and low concentrations of sodium and potassium. Similar to the Piñon Creek flow path, the end point of the Sacramento River has low path has low bicarbonate, low chloride, high sulfate, a mixture between calcium and magnesium, and low sodium and potassium. The calcium-to-magnesium ratio is maintained at a one-to-one ratio.

The Cornucopia Draw is in-between the Sacramento River and Piñon Creek, and also shares a similar chemistry (Figure 3.13a). This draw is dominated by calcium and sulfate, both showing a slight increase along the flow path. There is a spike in constituents towards the beginning of the flow path. Nonetheless, there is an increase in most constituents, with the exception of bicarbonate and sodium. The former has a slight decrease, while the latter is minimal throughout the entire Cornucopia Draw. The arrows on the Piper diagram designate the flow direction along the Cornucopia Draw from north to south. From the beginning point to the end point, there is not much change in cation concentrations. The anions start with high bicarbonate, low chloride, and low sulfate. The end point has decreased bicarbonate, unchanged chloride, and increased sulfate concentrations. On the Piper diagram, the calcium-to-magnesium ratio is approximately one-to-one.

Shiloh Draw flows in a different direction from the rest of the New Mexico flow paths, from west to east, and still flows towards Dell City, TX. The majority of Shiloh Draw is dominated by sulfate and calcium (Figure 3.14a). Bicarbonate and magnesium are secondary anions and cations, respectively. There is a spike in sodium a third of the way along the Shiloh Draw flow path, but this high concentration is not sustained along the remainder of the flow path. There is not a consistent trend on the Piper diagram, but the graph suggests a slight increase in constituents moving along the flow path. The arrows designate the flow path from west to east.. The anions show a decrease in bicarbonate and an increase in sulfate while the chloride concentration remains low. On the cation triangle, there is an increase in calcium with an increase in magnesium and decrease in sodium and potassium while maintaining a calcium-to-magnesium one-to-one

ratio. However, there is high variability in constituent concentrations, so there is high uncertainty in any trends from Shiloh Draw data.

3.2.2 NM Carbonates– Han Plots

The Han plots, based on Han et al. (2012) [2], for the carbonates within the New Mexico portion of the Salt Basin are shown in Figure 3.15. All three of the graphs show a trend of enriching $\delta^{13}\text{C}$, decreasing radiocarbon percent modern carbon, and a decrease in dissolved inorganic carbon (an increase in 1/DIC). Hence, there must be a source of enriched $\delta^{13}\text{C}$ that contributes to the DIC as the radiocarbon is removed from the groundwater or decays from the system. In each graph, the trend continues on either side of the Z diagonal line. This departure from a singular region means there is likely mixing of multiple carbon sources, but this mixing has minimal affect as shown by the general grouping of the carbon points. Graph i and graph ii show the majority of the Salt Basin carbon data on the right side of the vertical axis. Graph iii shows the majority of the points beneath the Z diagonal line.

3.2.3 NM Carbonates– Radiocarbon Analyses

Fontes and Garnier radiocarbon corrections were applied to the carbon data in the NM Carbonates geologic province (Table 3.1). However, this method corrected for isotopic exchange, and it does not account for radiocarbon activity changes due to incongruent dissolution, such as dedolomitization. Measured radiocarbon activities in the NM Carbonates range from 8.19 to 67.7 pmC (Figure 3.9).

Since this method corrected for isotopic exchange, it does account for radiocarbon activities due to incongruent dissolution, such as dedolomitization. Sigstedt (2010) [14] conducted a detailed chemical analysis of Piñon Creek. During which, it was concluded that dedolomitization was a dominant process along this flow path. A dedolomitization-specific radiocarbon correction method was applied using the NETPATH model. NETPATH is an inverse, mass balance model that uses hydrochemical data to perform mass transfer reactions, Raleigh distillation calculations, and model comparisons [14, 19]. Further, it is possible to specify processes within the overall NETPATH model. In Sigstedt (2010) [14], dedolomitization was included in the model by having gypsum and dolomite dissolution and calcite precipitation. The radiocarbon corrections in NETPATH also included specified input values for the carbonate aquifer of $\delta^{13}\text{C}$ equal to 5.7‰ [14]. For more detail regarding this correction, refer to Sigstedt (2010) [14]. The NETPATH-corrected radiocarbon ages from Sigstedt (2010) [14] are shown in Figure 3.16. Like the Fontes and Garnier corrections, there is a trend of increasing residence time moving southwards. The range of ages from Sigstedt (2010) [14] is 3,500 to 16,600 years.

3.3 Texas– Cretaceous Province

The Texas Cretaceous province contains the Finlay limestone and Pump Station Hills rhyolite porphyry. The Finlay formation is characterized as a Cretaceous limestone with secondary permeability due to carbonate dissolution and minor faulting. The Pump Station Hills rhyolite porphyry is characterized as a coarsely and heterogeneously fractured Precambrian unit. Within this geological province, there are two major flow paths: W.Antelope Draw and W.South Well Draw. These flow paths begin in the Cretaceous province, but later flow through the Victorio Peak province as E.Antelope and E.South Well before discharging into the Salt Flats province. These connections will be discussed in further detail later.

3.3.1 TX Cretaceous– Hydrochemical Trends

The W.Antelope Draw flows parallel to the Shiloh Draw, but resides in the Texas portion of the Salt Basin. The chemistry of W.Antelope Draw is shown in Figure 3.17a. The constituents graph shows an initial peak in concentrations towards the headwaters of this flow path with a decrease in components further along the flow path towards the Salt Flats. The W.Antelope Draw Piper diagram shows intermediate anions, low calcium, high magnesium, and high sodium and potassium. There is one point of high chloride in W.Antelope Draw. Due to the lack of supporting evidence to suggest a simple flow path through this draw, there are no arrows showing flow direction on the Piper diagram. Instead, there is a line to designate chemical trends. The chemical trend of W.Antelope Draw highlights an increase in calcium, increase in magnesium, and a decrease in sodium and potassium that produces a calcium-to-magnesium ratio of one-to-one.

The W.South Well Draw parallels the W.Antelope Draw in the southwestern Salt Basin. The chemical constituents' graph and Piper diagram for this draw are shown in Figure 3.18a. This flow path is characterized by increasing constituents moving towards the Salt Flats to the east. The majority of these constituents are added to the groundwater two-thirds of the way along the W.South Well Draw flow path. The Piper diagram shows a range of bicarbonate, a range of chloride, and consistently low sulfate concentrations. The general trend of increasing chloride with decreasing bicarbonate and unchanging sulfate is designated by the line within the anion triangle. The cations are mostly low calcium, low magnesium, and high sodium and potassium. Since there is one point that shows increasing calcium, increasing magnesium, and decreasing sodium and potassium trend, there is a trend line added to the cation triangle. This trend line is approximately a one-to-one ratio of calcium-to-magnesium. The overall trend of anions and cations appears on the ternary diamond and is highlighted with a line.

3.3.2 TX Cretaceous– Han Plots

The carbon data from W.Antelope Draw and W.South Well Draw are shown in the Han plots in Figure 3.19. The points are separated by color based on the points position with respect to the vertical axis in the first graph (red = right, higher 1/DIC, blue = left, lower 1/DIC). For the red points, there is a trend of enriching $\delta^{13}\text{C}$, decreasing radiocarbon percent modern carbon, and a decrease in dissolved inorganic carbon (an increase in 1/DIC). This is the same trend as the NM Carbonates. There is also an anomalous point with high radiocarbon (>90 pmC) that suggests an influential source of radiocarbon or recently recharged waters. The blue points are generally clustered around low radiocarbon activities, but have a range of $\delta^{13}\text{C}$ and 1/DIC. This range of $\delta^{13}\text{C}$ and 1/DIC parallels the Z diagonal line in graph i. Graph i and graph ii show the majority of the blue Salt Basin carbon data on the left side of the vertical axis, but still above or below the Z line, respectively. Graph iii shows the majority of the points beneath the Z diagonal line.

3.3.3 TX Cretaceous– Radiocarbon Analyses

A general groundwater residence time for the groundwaters in the Texas Cretaceous was determined using the Fontes & Garnier radiocarbon age correction method. The results from this correction are included in Table 3.1. There is a lack of trend in these corrected radiocarbon ages and a lack of trend in measured radiocarbon activities; young waters and juxtaposed with old waters (Figure 3.9). Further, there are younger waters further along the flow path with older waters near the Salt Basin margin. The overall radiocarbon activity range is from 4.34 to 90.77 pmC.

Since there was no clear radiocarbon age trend from the general Fontes and Garnier correction method, a mixing of young and old waters resulted in another correction factor for the initial radiocarbon activities. Figure 3.20 shows the resulting mixing corrected radiocarbon ages that were extended down the length of Antelope Draw and South Well Draw. This spatial extension included the possibility of the two-waters mixing system of the Cretaceous geologic province continuing beneath and contributing to the Victorio Peak geologic province.

Using a young calcium to sodium ratio of 10 and an old ratio of 0.1, the corrected ages are listed in Table 3.3. The corrected ages range from 542 years to 26,000 years. The negative corrected ages were removed because the negative corrected age suggests the mixing correction equation was invalid for those points. There is a trend towards higher carbon to sodium ratios and lower measured radiocarbon activities for the older points (Figure 3.21). This trend suggests dedolomitization is occurring within the old waters in the aquifer matrix, but not within the young waters moving through the fractures and mixing in the two-waters mixing system. Even with this mixing correction, there is not a clear

trend of increasing or decreasing corrected radiocarbon groundwater age within the Cretaceous geologic province.

3.4 Texas– Victorio Peak Province

The Texas Victorio Peak province contains the Victorio Peak. This formation is characterized as limestone and dolomite interbedded with siliceous shale and sandstone [23]. Within this geological province, there are two major flow paths: E.Antelope Draw and E.South Well Draw. These flow paths begin in the Cretaceous province as W.Antelope and W.South Well Draw, but later flow through the Victorio Peak province before discharging into the Salt Flats province. These connections will be discussed in further detail later.

3.4.1 TX Victorio Peak– Hydrochemical Trends

The E.Antelope Draw flows begins when the W.Antelope Draw flow path leaves the Cretaceous geologic province and enters the Victorio Peak carbonate. This transition zone is between the two red vertical lines on the components plot. There is a slight increase in TDS and an early spike in chloride, but the rest of the components remain relatively unchanged in the second half of the flow system, within the Victorio Peak geologic province. The Piper diagram in Figure 3.22a contains both the W.Antelope Draw and E.Antelope Draw data in light green and dark green, respectively. The two halves of the flow path have similar chemistry, but the E.Antelope Draw has overall less bicarbonate, more chloride, more sulfate, more calcium, more magnesium, and less sodium and potassium. Due to the lack of supporting evidence to suggest a simple flow path through this draw, there are no arrows showing flow direction on the Piper diagram. Instead, there is a line to designate chemical trends. The chemical trend of E.Antelope Draw highlights a trend of increasing calcium with increasing magnesium and decreasing sodium and potassium with a calcium-to-magnesium ratio of one-to-one that is shared in the W.Antelope Draw Piper diagram.

The total of South Well Draw is primarily within W.South Well Draw, but there are a few additional points from within E.South Well Draw (Figure 3.23a). Shortly before entering the Victorio Peak carbonate, the South Well Draw has a decrease in components. This decreasing trend is continued within E.South Well Draw. As before, the transition zone between the Cretaceous geologic province and the Victorio Peak carbonate province is designated with the two red vertical lines in the components plot. The Piper diagram is also separated into two colors: white with gray outline is W.South Well Draw, just gray is E.South Well Draw. The trend lines on the Piper diagram designate the increase in chloride with decreasing bicarbonate and unchanging sulfate and the one-to-one ratio of calcium-to-magnesium. With the increasing calcium, the trend line shows the increase in

magnesium and decrease in sodium and potassium. The overall trend of anions and cations appears on the ternary diamond and is highlighted with a line. The E.South Well data plots within the W.South Well data on the Piper diagram and does not have any additional aspects.

3.4.2 TX Victorio Peak– Han Plots

The carbon data from Antelope Draw and South Well Draw are shown in the Han plots in Figure 3.24. The points are separated by color based on the geologic province: red = eastern flow paths in Victorio Peak, blue = western flow paths in Cretaceous. The red points are the focus of this section, but require the blue points for context. There is a trend of enriching $\delta^{13}\text{C}$, near constant radiocarbon percent modern carbon, and a decrease in dissolved inorganic carbon (an increase in 1/DIC). This trend is similar to that of the NM Carbonates and TX Cretaceous. However, the Victorio Peak carbon points tend to have higher 1/DIC, or lower DIC, and lower radiocarbon activities. Hence, there must be a source of enriched $\delta^{13}\text{C}$ that contributes to the DIC. Further, the groundwaters likely have long residence times and dispersed water sources to produce the consistently low radiocarbon activity. The majority of the red Victorio Peak carbon data points are within Region 2 and Region 6 on the Han plots.

3.4.3 TX Victorio Peak– Radiocarbon Analyses

The Fontes and Garnier method corrected radiocarbon activities along the E.Antelope and E.South Well to produce a corrected radiocarbon age (Table 3.1). Within the measured radiocarbon activities, there is a slight trend of younger waters towards the east. However, this trend is counter to the expected trend of older waters further along the flow path. The overall range of radiocarbon activities is 5.36 to 49.5 pmC.

The mixing radiocarbon corrections were extended into the Victorio Peak geologic province from the Cretaceous geologic province, and those results were presented previously.

3.5 Texas– Capitan Reef Province

The Texas Capitan Reef province contains the Capitan Reef complex. This complex is characterized as high permeability limestone and dolomite interbedded with sandstone [31, 56]. Within this geological province, there is one major flow path: Capitan flow path. This flow path begins in the Capitan Reef province, but discharges into the Salt Flats province. These connections will be discussed in further detail later.

3.5.1 TX Capitan Reef– Hydrochemical Trends

The chemistry of the Capitan flow path is shown in Figure 3.25a. There are a few spikes of high TDS, sodium, and chloride moving from north to south. A slight overall decrease in bicarbonate counters a slight overall increase in sulfate. Generally, the concentrations of the components do not have an increasing or decreasing trend throughout the Capitan flow path. The Piper diagram of Capitan data points has an anion and cation trend, but no diamond ternary trend. The anions show an increase of chloride with decreasing concentrations of bicarbonate and unchanging sulfate. For the cations, there is a trend of increasing calcium with increasing magnesium and decreasing sodium to potassium, producing an overall calcium-to-magnesium ratio of one-to-one.

3.5.2 TX Capitan Reef– Han Plots

While there are only four carbon data points within the Capitan geologic province, the Han plots can help determine the dominant processes occurring within this geologic province. Figure 3.26 shows the three Han plots for the Capitan geologic province. All of the carbon points are within Region 2 or Region 6. There is minimal range between the $1/\text{DIC}$, $\delta^{13}\text{C}$, and radiocarbon values. There is a slight trend of enriching $\delta^{13}\text{C}$, near constant radiocarbon percent modern carbon, and a decrease in dissolved inorganic carbon (an increase in $1/\text{DIC}$). This trend is similar to that of the NM Carbonates, TX Cretaceous, and TX Victorio Peak.

3.5.3 TX Capitan Reef– Radiocarbon Analyses

The four carbon points in the Capitan geologic province show a general increase in age moving southwards (Figure 3.9). These activities align with the trend from Fontes and Garnier radiocarbon corrections listed in Table 3.1. The overall range of radiocarbon activities from 12.1 to 24.2 pmC for the Capitan geologic province.

3.6 New Mexico– Artesia Group Province

The New Mexico Artesia Group province contains the Artesia Group complex. This complex is characterized as dolomite interbedded with sandstone [31, 46]. Within this geological province, there is one major flow path: Big Dog Canyon. This flow path begins in the Artesia Group province, but is redirected towards the west and discharges into the Salt Flats province. These connections will be discussed in further detail later. There are no carbon data in the Artesia Group geologic province. Hence, there are no Han plots or radiocarbon analyses.

3.6.1 NM Artesia Group– Hydrochemical Trends

Big Dog Canyon has two data points. Consequently, there is limited chemical evolutionary trends to be seen. Figure 3.27a shows the chemical composition of these two points as they would change moving along the flow path from south to north. There is an increase in the majority of the constituents, with the exception of a decrease in bicarbonate concentration. The Piper diagram for Big Dog/Artesia group shows a two-point trend towards increasing TDS, decreasing bicarbonate, constant chloride, increasing sulfate, increasing calcium, decreasing magnesium, and constant sodium and potassium.

3.7 Dell City, TX– Bone Spring/Victorio Peak Province

The Dell City, TX Bone Spring/Victorio Peak province contains the Bone Spring and Victorio Peak carbonates. The Bone Spring formation and Victorio Peak formation are characterized as limestone and dolomite interbedded with siliceous shale and sandstone [23]. Within this geological province, there is one major flow path: Dell City, TX. This flow path is a combination of the Piñon Creek, Cornucopia Draw, Sacramento River, and Shiloh Draw waters before the ground-water discharges into the Salt Flats province. These connections will be discussed in further detail later. There is no carbon data in the Bone Spring/Victorio Peak geologic province. Hence, there are no Han plots or radiocarbon analyses

3.7.1 Dell City, TX– Hydrochemical Trends

Dell City, TX has a significant amount of chemistry data points, likely due to agriculture and population. Figure 3.28a shows the chemistry of Dell City. The graph of constituents is complicated by the multitude of points. Regardless, there is a slight decrease in most constituents moving southwards through Dell City. The increasing components are chloride and sodium. Average TDS remains constant moving southwards through Dell City. On the Piper diagram, the Dell City points are focused along the low bicarbonate side of the anion triangle and in the center of the cation triangle. There is a range of sulfate for the consistently low bicarbonate and range of chloride concentrations. The trend shows an increase in chloride with a decrease in sulfate. The calcium-to-magnesium ratio is maintained at a one-to-one ratio. The cation triangle shows an increase in calcium with an increase in magnesium and a decrease in sodium and potassium. The two trends are also seen on the diamond ternary plot with high chloride and sulfate concentrations corresponding to a range of calcium and magnesium.

3.8 Texas– Salt Flats Province

The Texas Salt Flats province contains the Salt Flats and playas. These playas are characterized as gypsum, halite, calcite, dolomite, and quartz sediments with high evaporative potential [13, 25, 31, 58, 59]. This flow path is the terminus path of all of the Salt Basin groundwater as it is evaporated from the playa surface [13, 25]. The Salt Flats groundwater flows from the playas to the northeast of Dell City, through Dell City, and towards the southern margin of the Salt Basin. These connections will be discussed in further detail later.

3.8.1 TX Salt Flats– Hydrochemical Trends

The Salt Flats have a chemical signature similar to the rest of the Salt Basin. The chemistry of the Salt Flats is shown in Figure 3.29a. There is variability in the concentrations of constituents. Due to an early peak of chloride and sodium, there is a slight decrease in the concentration of these components further southwards. There are also a few spikes of chloride, sodium, and potassium throughout the remainder of the Salt Flats flow path. The Piper diagram shows a range of anions with a calcium-to-magnesium ratio of one-to-one throughout. Increasing calcium trends with increasing magnesium and decreasing sodium and potassium. There is a slight trend of increasing bicarbonate with decreasing chloride and increasing sulfate. Overall, the Salt Flats chemistry points are spread throughout the diamond ternary plot, showing slight preference towards higher chloride and sulfate

3.8.2 TX Salt Flats– Han Plots

The six carbon data points for the Salt Flats geologic province are plotted onto the Han plots shown in Figure 3.30. All of the carbon points are within Region 2, Region 6, or along the vertical axis. There is minimal range between the $1/\text{DIC}$, $\delta^{13}\text{C}$, and radiocarbon values. There is a slight trend of enriching $\delta^{13}\text{C}$, near constant radiocarbon percent modern carbon, and a decrease in dissolved inorganic carbon (an increase in $1/\text{DIC}$). This trend is similar to that of the rest of the Salt Basin carbon data. Compared to the Capitan geologic province, the Salt Flats geologic province is more enriched in $\delta^{13}\text{C}$.

3.8.3 TX Salt Flats– Radiocarbon Analyses

Starting in the playas to the northeast of Dell City and moving southwards through the Salt Flats, the radiocarbon activities decrease in value, which suggests older waters. Radiocarbon activities range from 13.5 to 26.1 pmC for the Salt Flats geologic province. Fontes and Garnier radiocarbon corrections also suggest an increasing age trend moving southwards (Table 3.1).

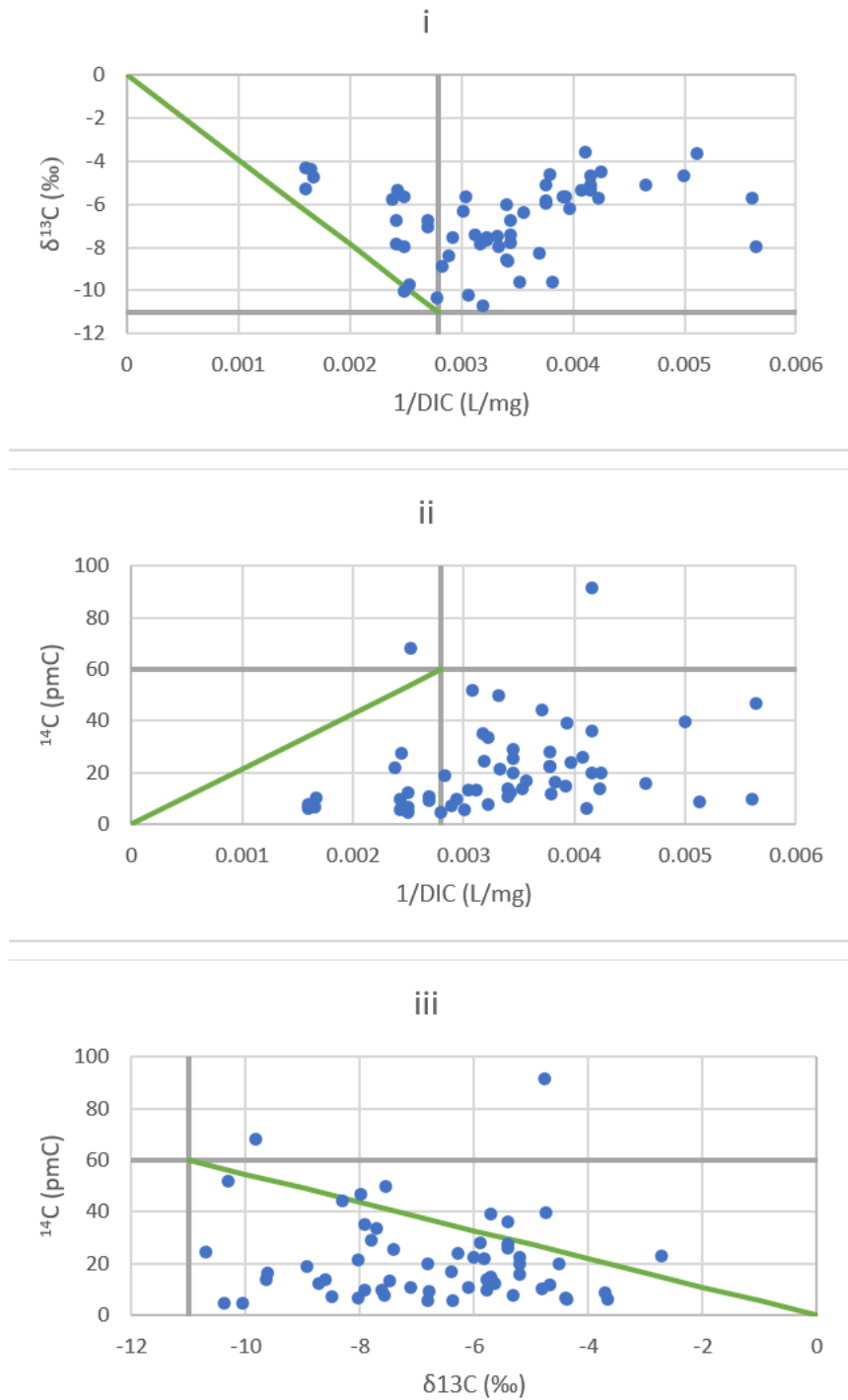


Figure 3.8: Overall Salt Basin carbon data plotted onto three carbon data interpretation graphs, created to match Han et al., 2012 [2]

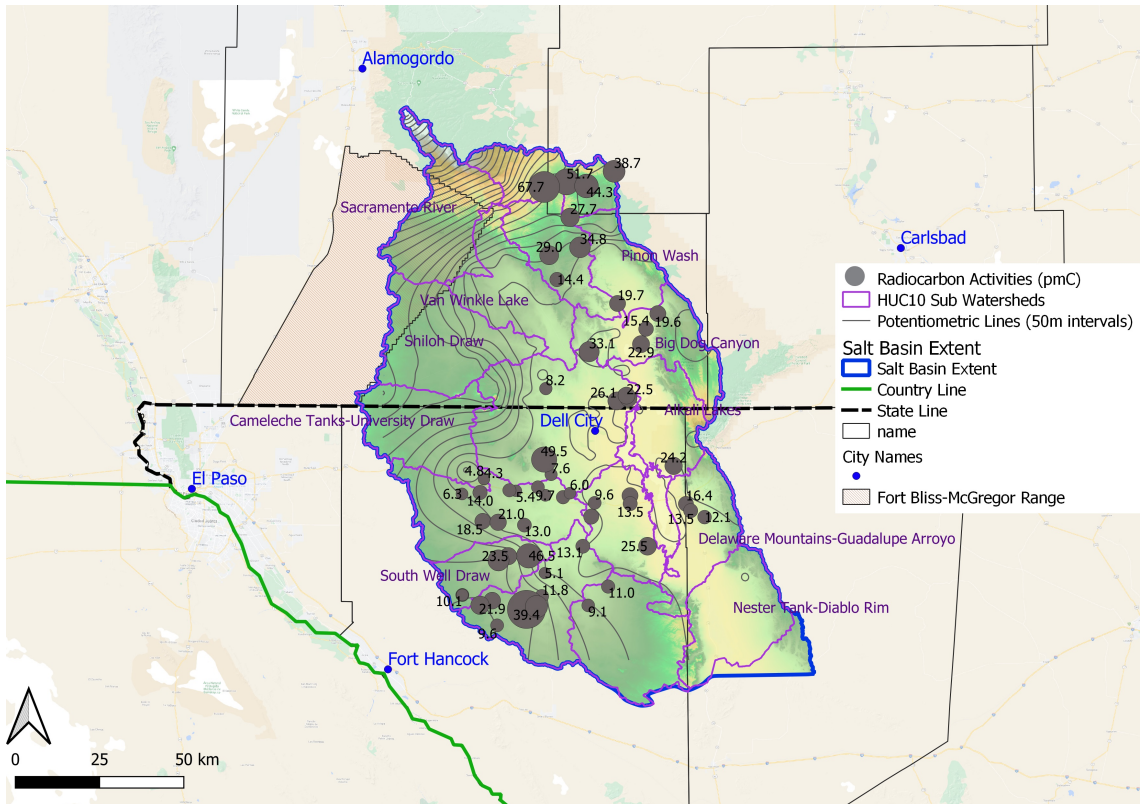


Figure 3.9: Salt Basin measured radiocarbon activities in percent modern carbon; size of the point is dependent upon the measured activity (larger points equal larger percent modern carbon)

A_g (pmC)	A_M (pmC)	ϵ	δ_M	δ_g
100	0	-10	5.7	-22

Table 3.2: Environmental parameters used in Fontes and Garnier radiocarbon correction equation with Salt Basin carbon points to get results in Table 3.1; A_g is the ^{14}C value of soil CO_2 gas; A_M is the average value of dissolving carbonate mineral; ϵ is the additive fractionation factor; δ_M is the $\delta^{13}\text{C}$ of the carbonate minerals [14]; δ_g is the $\delta^{13}\text{C}$ of the soil gas [20]

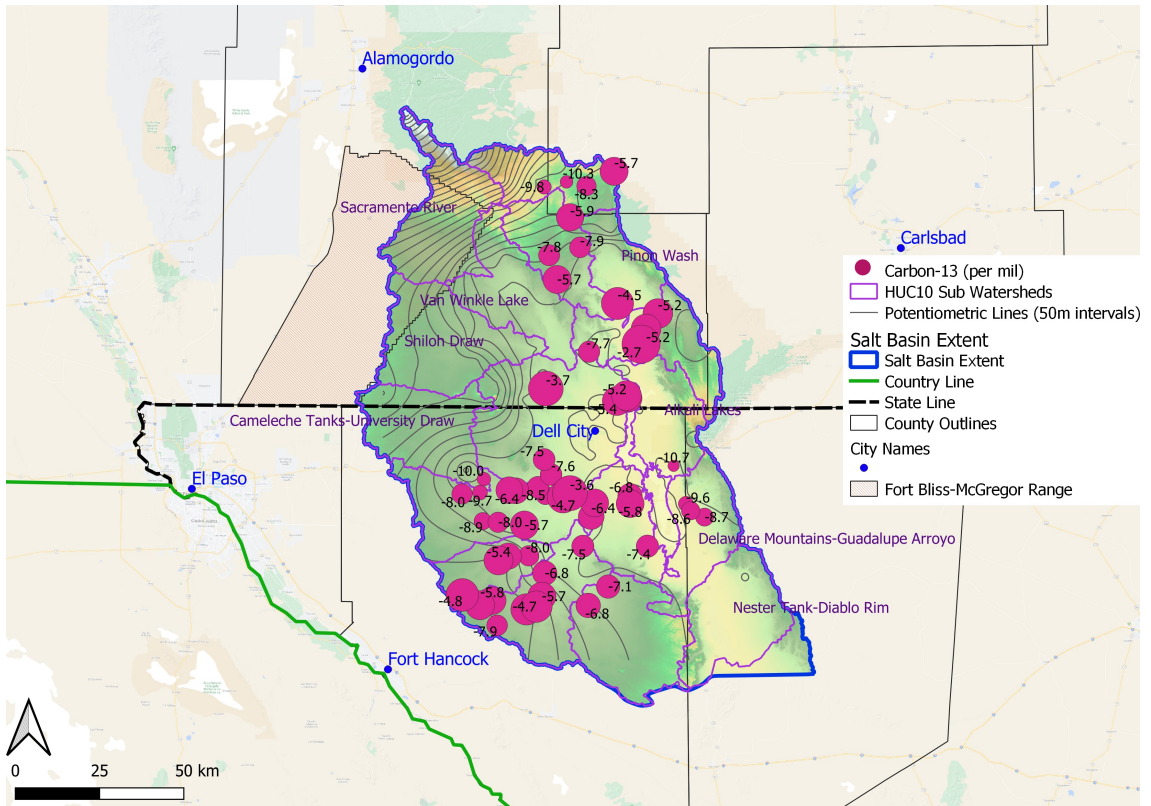
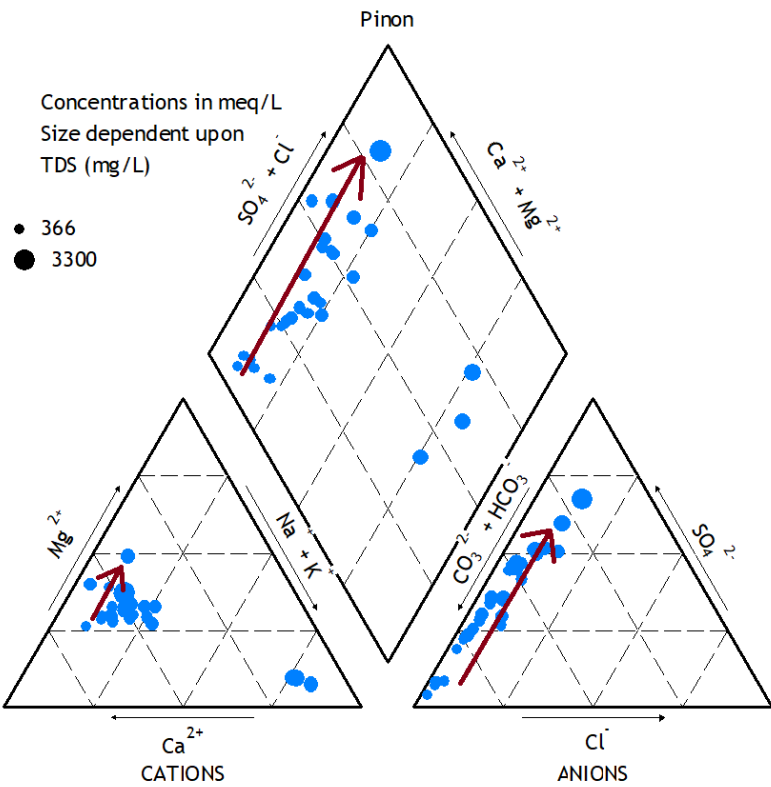
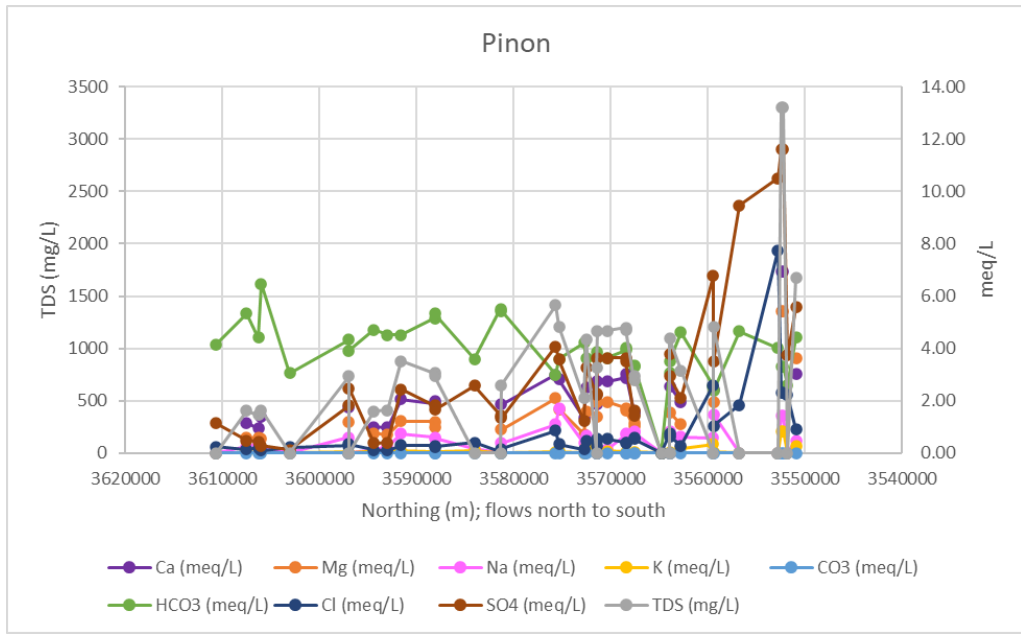
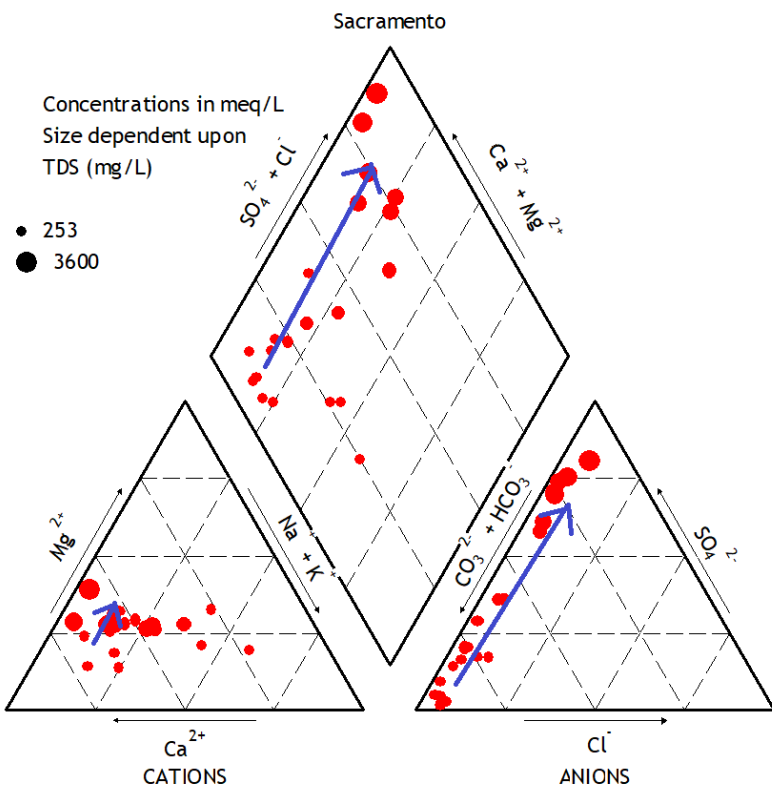
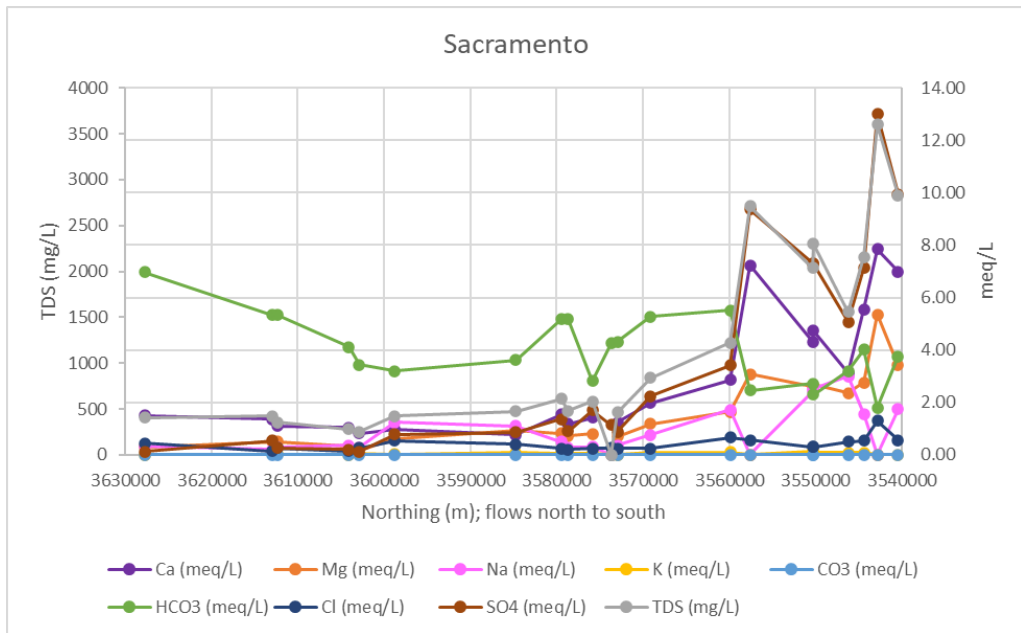


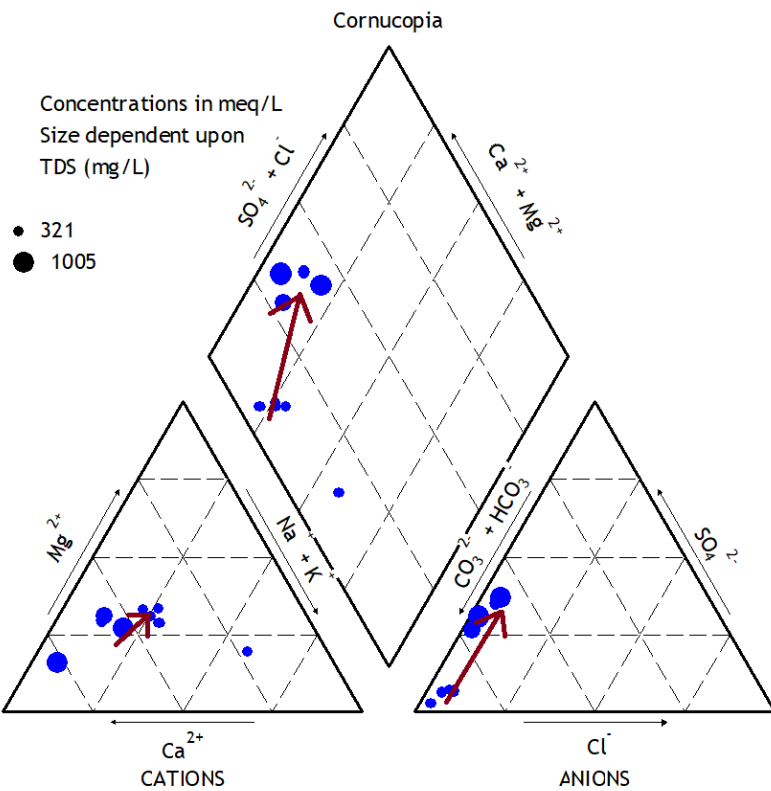
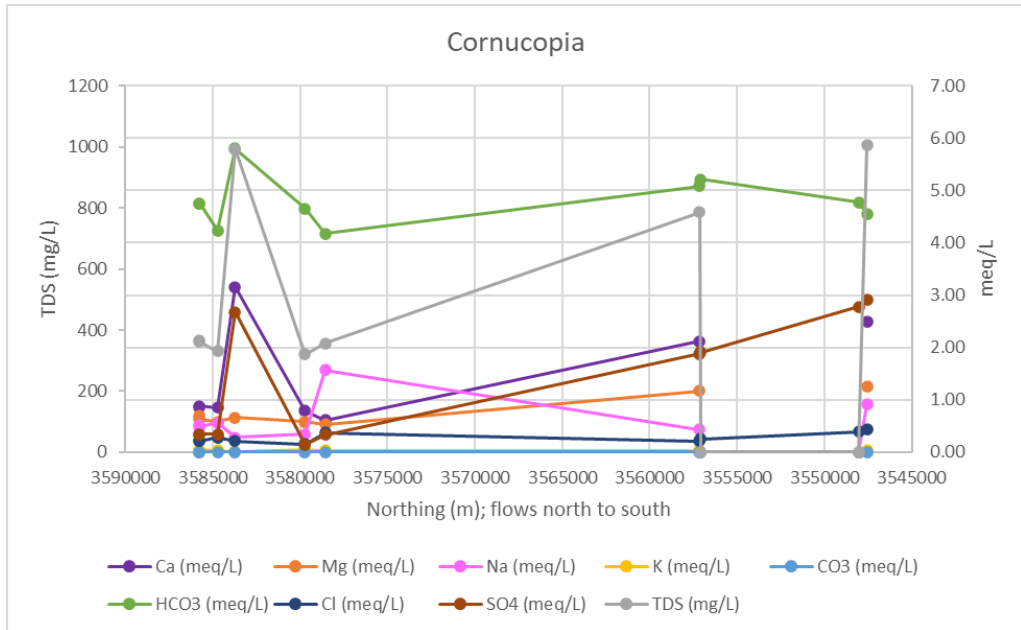
Figure 3.10: Salt Basin $\delta^{13}\text{C}$ concentrations (per mil); size of the point is dependent upon the concentration (larger points correspond to less negative values)



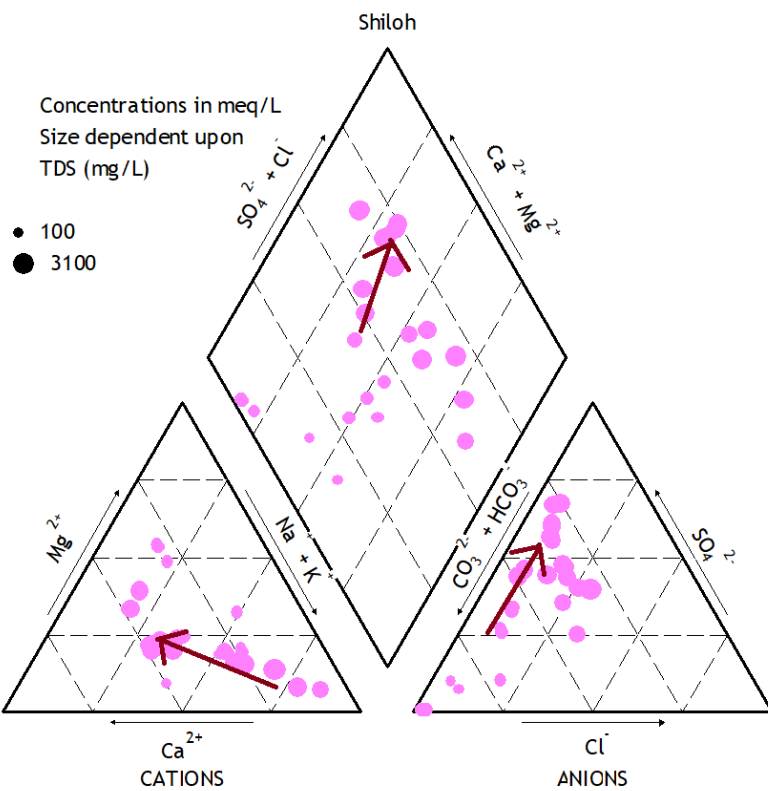
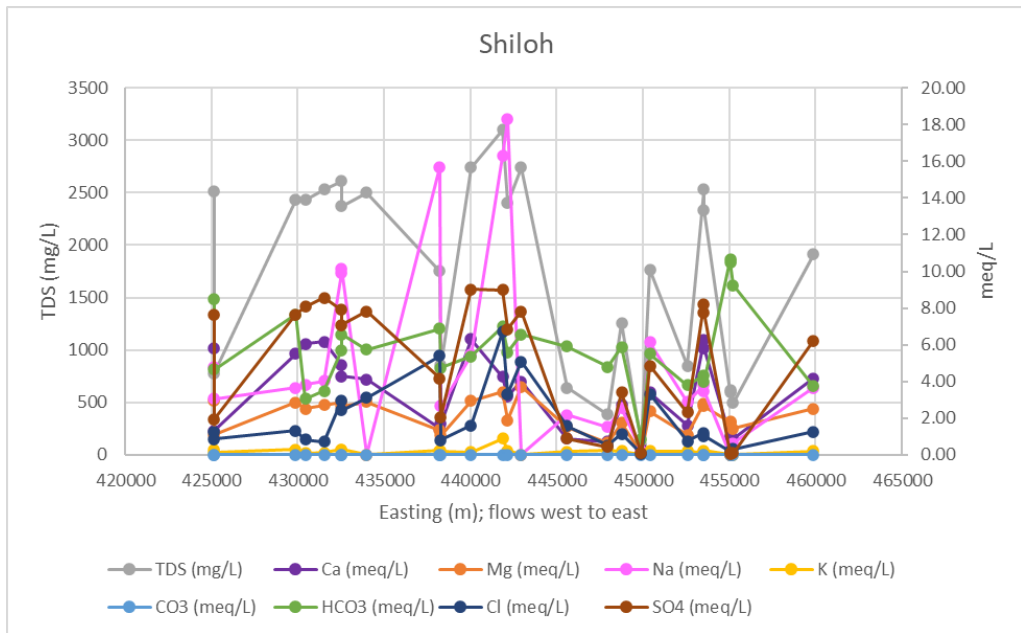
(a) Figure 3.11a Piñon Creek: Chemistry changes along flow path from north to south and corresponding Piper diagram; all concentrations are in meq/L, with the exception of TDS (mg/L); points on the Piper diagram are sized by TDS; arrows on Piper diagram designate flow direction from north to south



(a) Figure 3.12a Sacramento River: Chemistry changes along flow path from north to south and corresponding Piper diagram; all concentrations are in meq/L, with the exception of TDS (mg/L); points on the Piper diagram are sized by TDS; arrows on Piper diagram designate flow direction from north to south



(a) 3.13a Cornucopia Draw: Chemistry changes along flow path from north to south and corresponding Piper diagram; all concentrations are in meq/L, with the exception of TDS (mg/L); points on the Piper diagram are sized by TDS; arrows on Piper diagram designate flow direction from north to south



(a) Figure 3.14a Shiloh Draw: Chemistry changes along flow path from west to east and corresponding Piper diagram; all concentrations are in meq/L, with the exception of TDS (mg/L); points on the Piper diagram are sized by TDS; arrows on Piper diagram designate flow direction from west to east

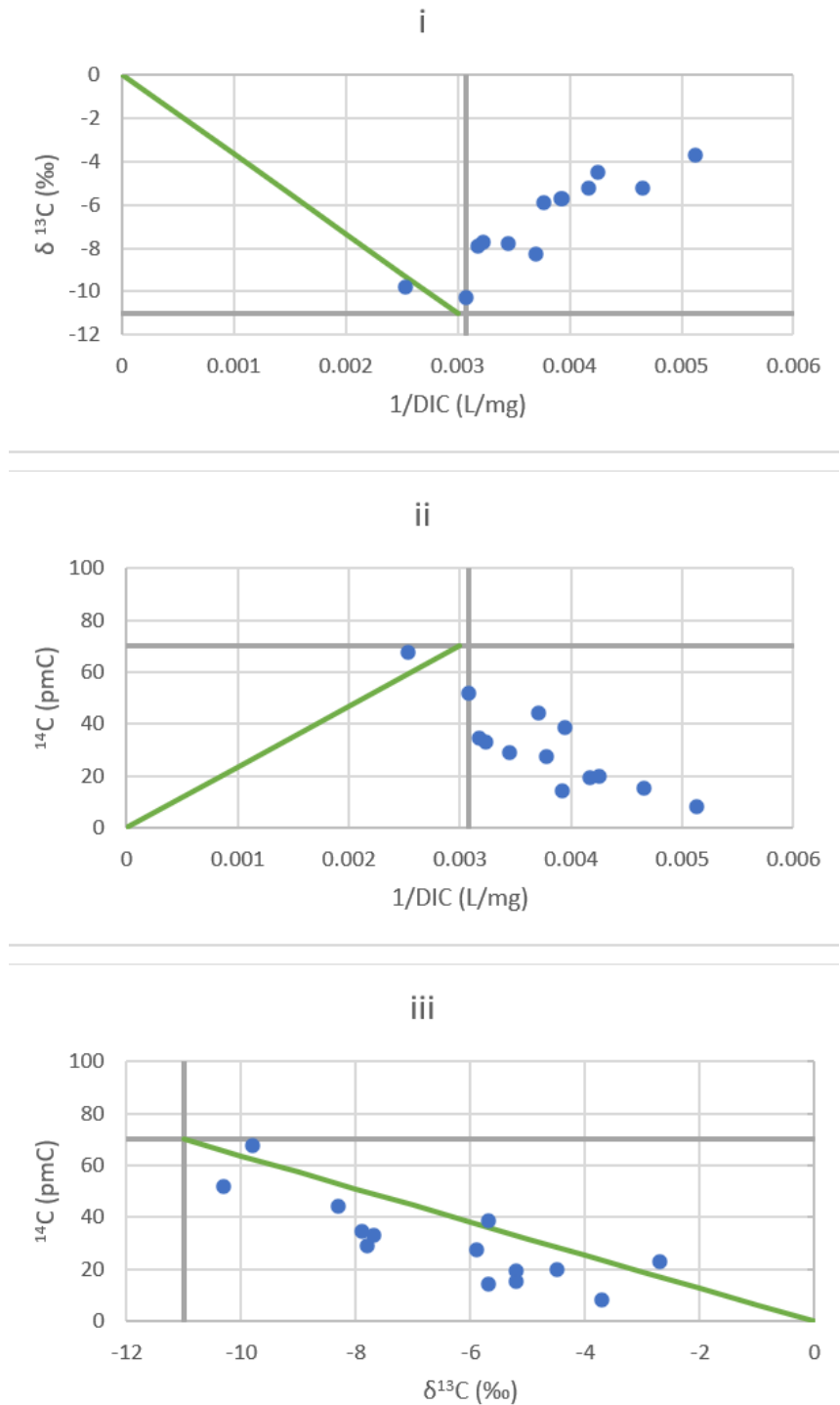


Figure 3.15: NM Carbonates carbon data plotted onto three carbon data interpretation graphs, to match Han et al., 2012 [2]

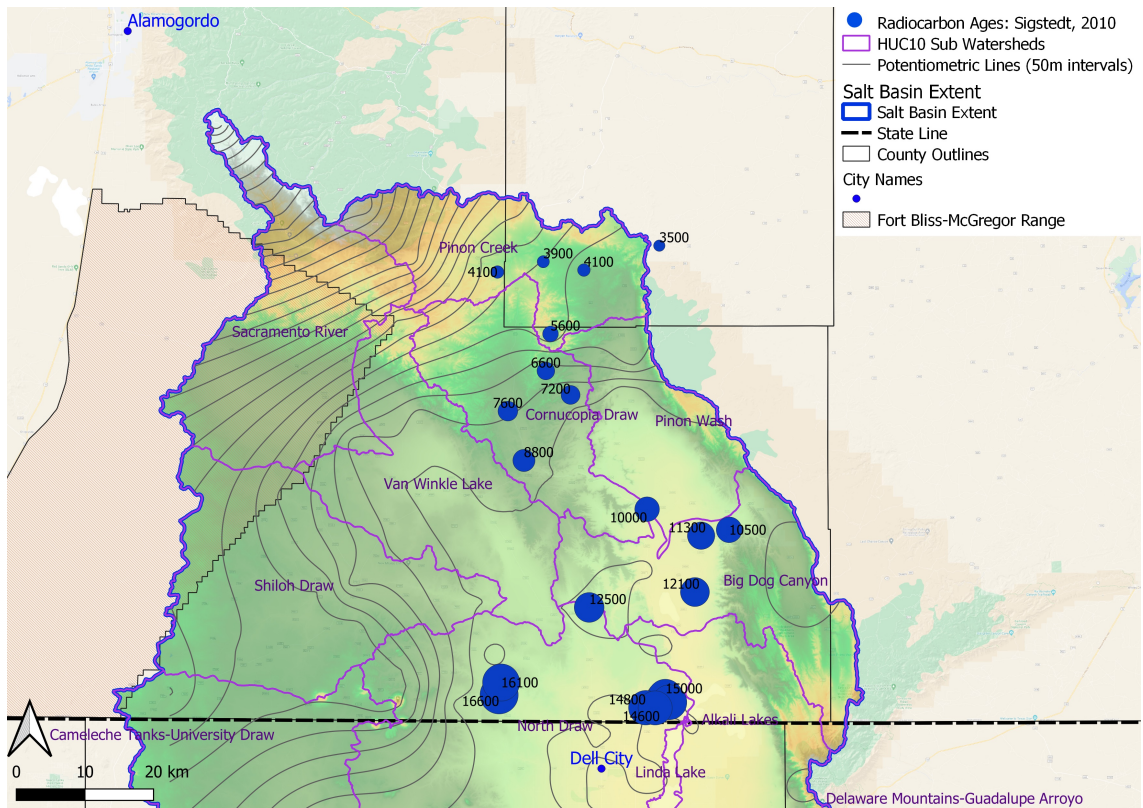
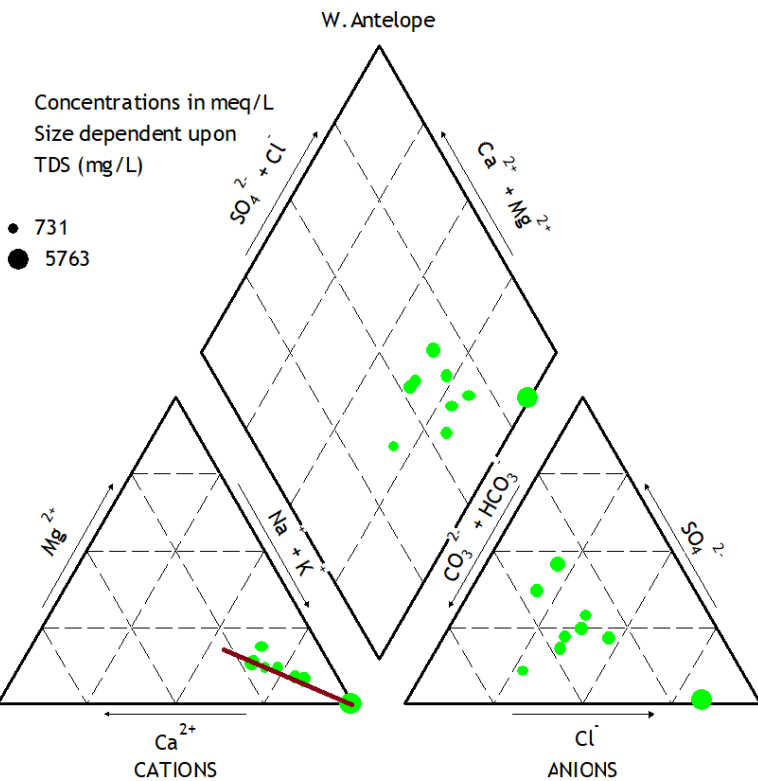
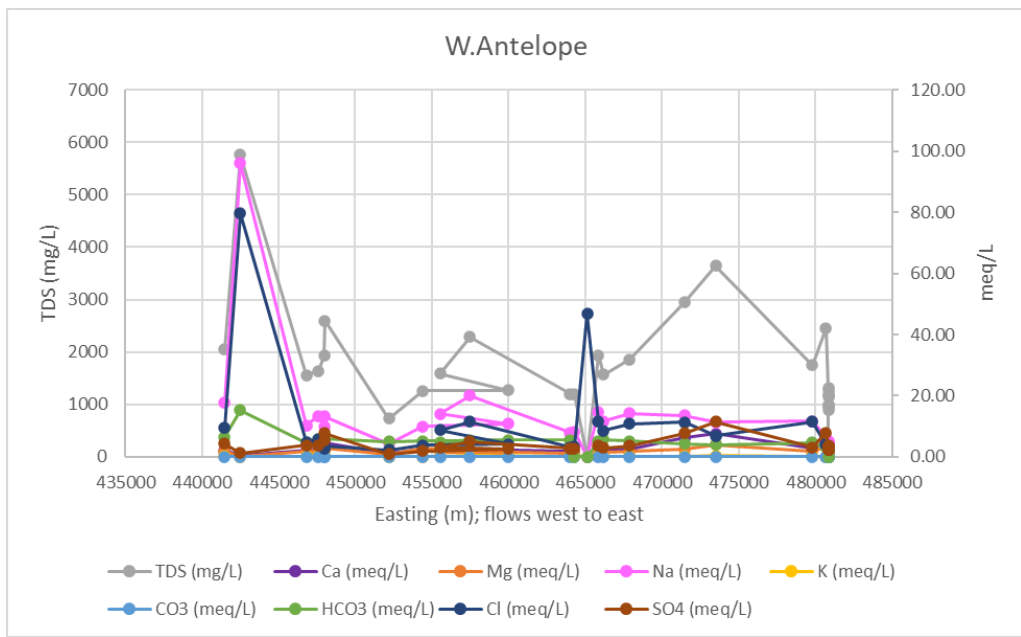


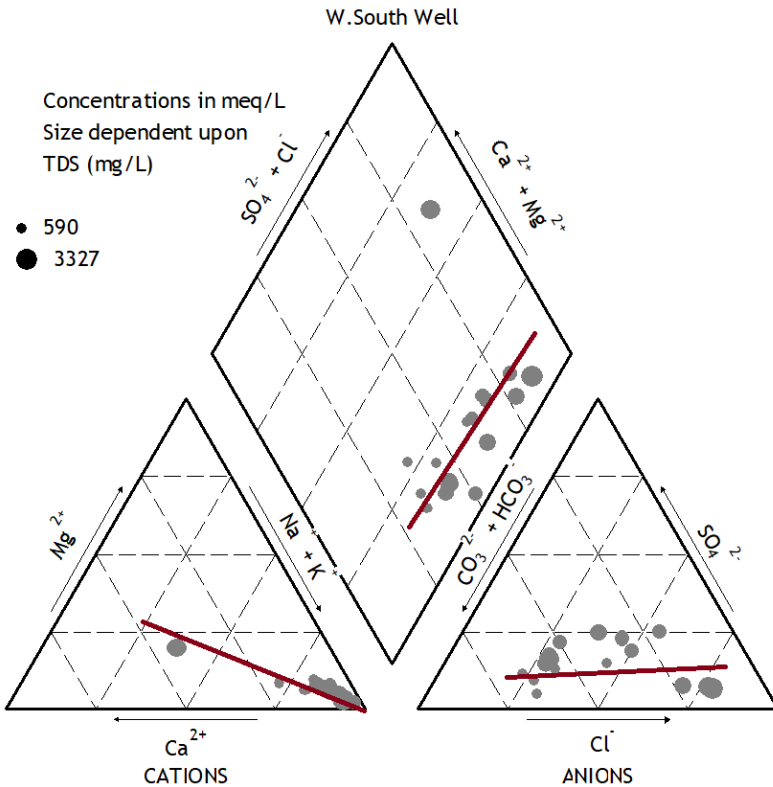
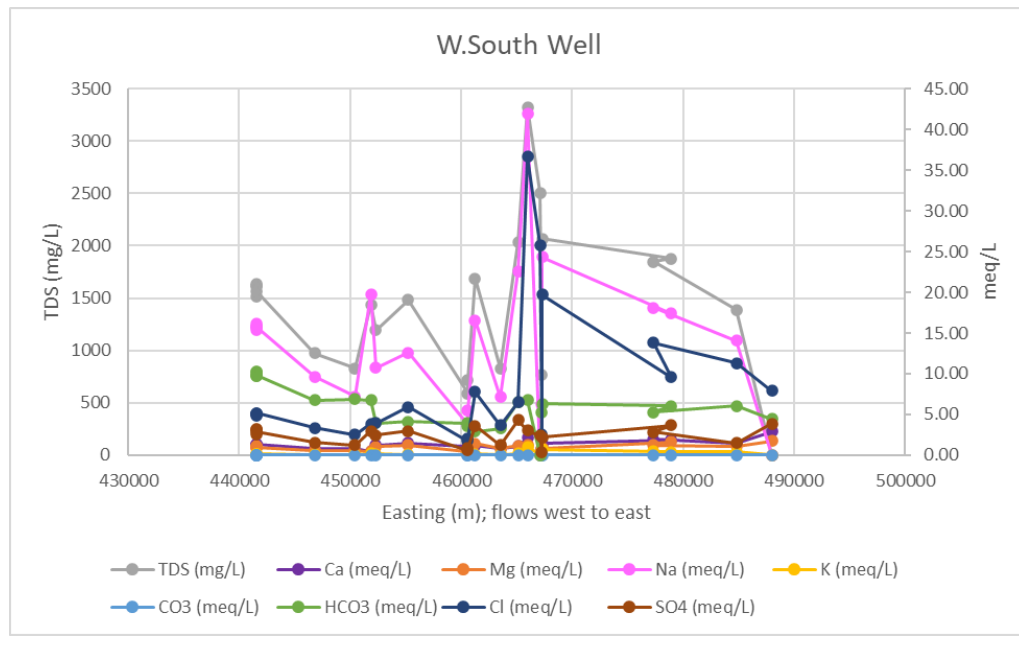
Figure 3.16: NM Carbonates corrected radiocarbon ages, using Sigstedt, 2010 dedolomitization correction method [14]

PointID	^{14}C (pmC)	Ca/Na (mmol/L)	f	$^{14}\text{C}_y^*$	t new (years)
SB-0406	4.84	0.66	0.06	13.2	16730
SB-0407	4.34	0.68	0.06	4.3	25935
SB-0412	5.36	0.25	0.01	73	2602
SB-0416	6.74	0.38	0.03	89.3	933
SB-0418	11.32	0.92	0.08	88.6	996
SB-0419	5.99	1.34	0.13	17.5	14402
SB-0459a	9.56	0.98	0.09	63.1	3809

Table 3.3: Mixing radiocarbon correction equation results with Salt Basin carbon points; Point ID and data from Appendix A.1; f is correction factor; $^{14}\text{C}_y^*$ is the corrected initial radiocarbon activity; t new is the corrected radiocarbon age from the mixing equation



(a) Figure 3.17a W.Antelope Draw: Chemistry changes along flow path from west to east and corresponding Piper diagram; all concentrations are in meq/L, with the exception of TDS (mg/L); points on the Piper diagram are sized by TDS; lines on Piper diagram designate general trends in chemistry



(a) Figure 3.18a W.South Well Draw: Chemistry changes along flow path from west to east and corresponding Piper diagram; all concentrations are in meq/L, with the exception of TDS (mg/L); points on the Piper diagram are sized by TDS; lines on Piper diagram designate general trends in chemistry

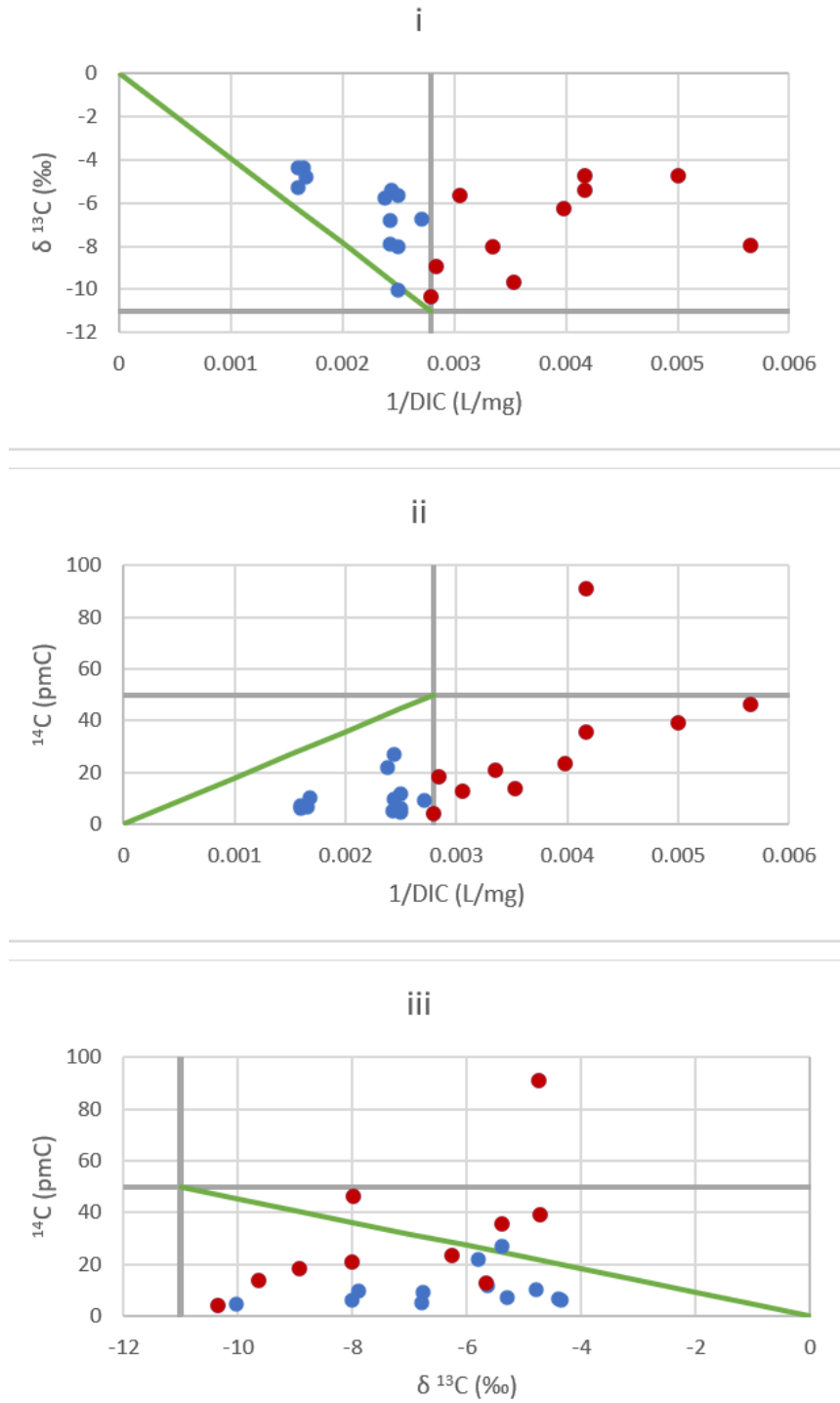


Figure 3.19: TX Cretaceous carbon data plotted onto three carbon data interpretation graphs, to match Han et al., 2012 [2]

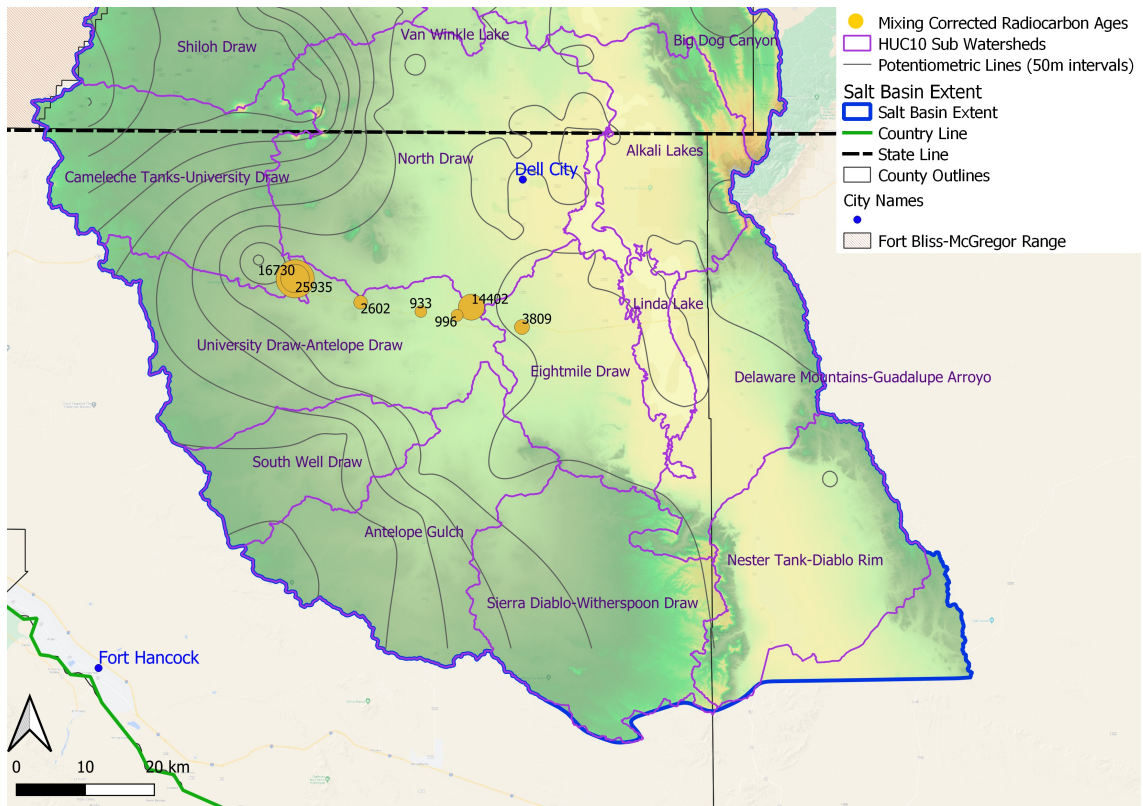


Figure 3.20: Salt Basin corrected radiocarbon ages using mixing equation with data from Table 3.3; size of the point is dependent upon the corrected age (larger points correspond to older corrected ages)

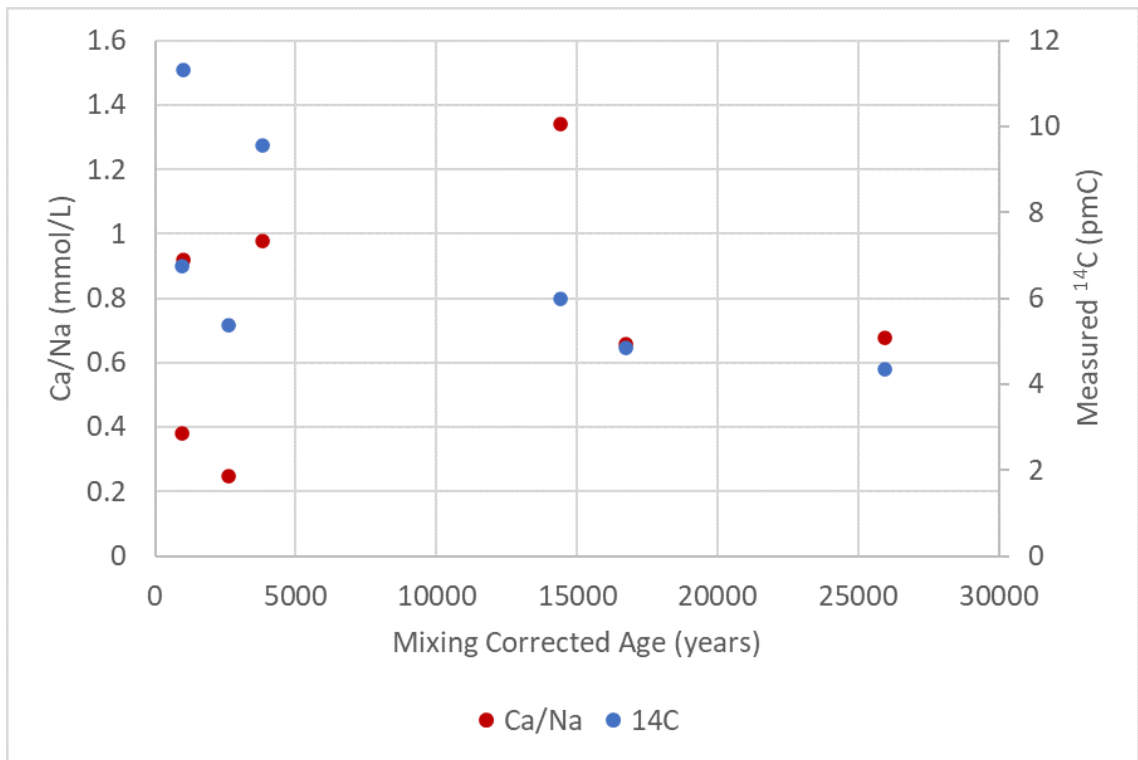
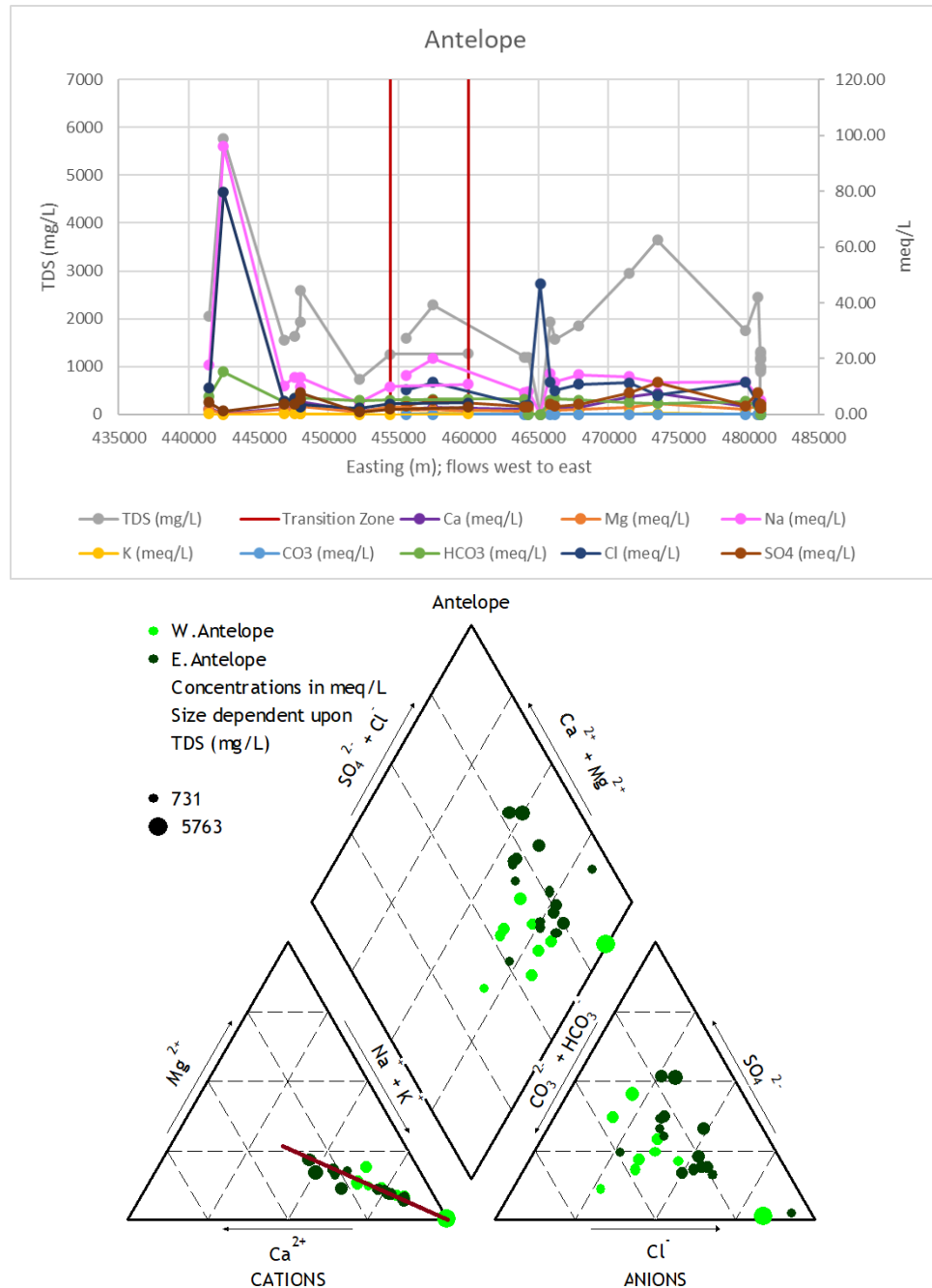
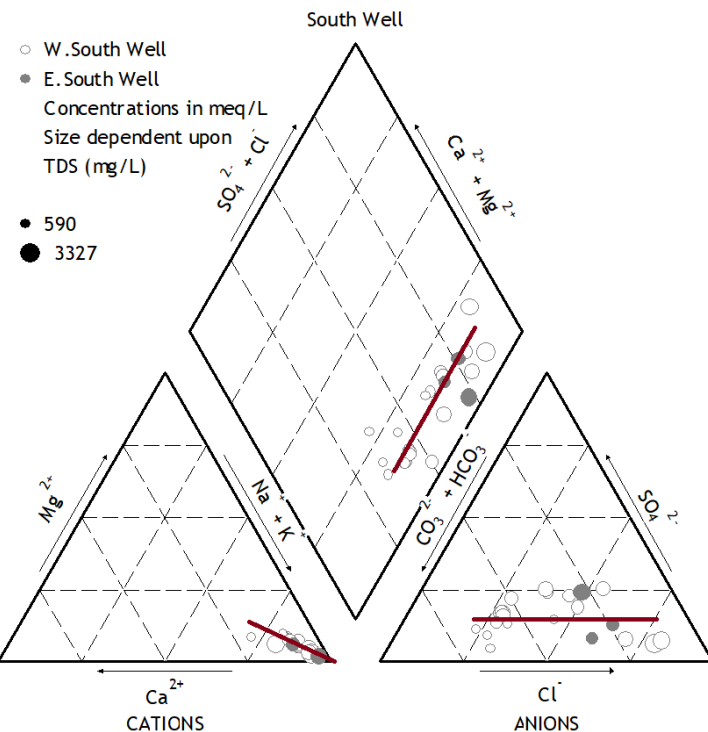
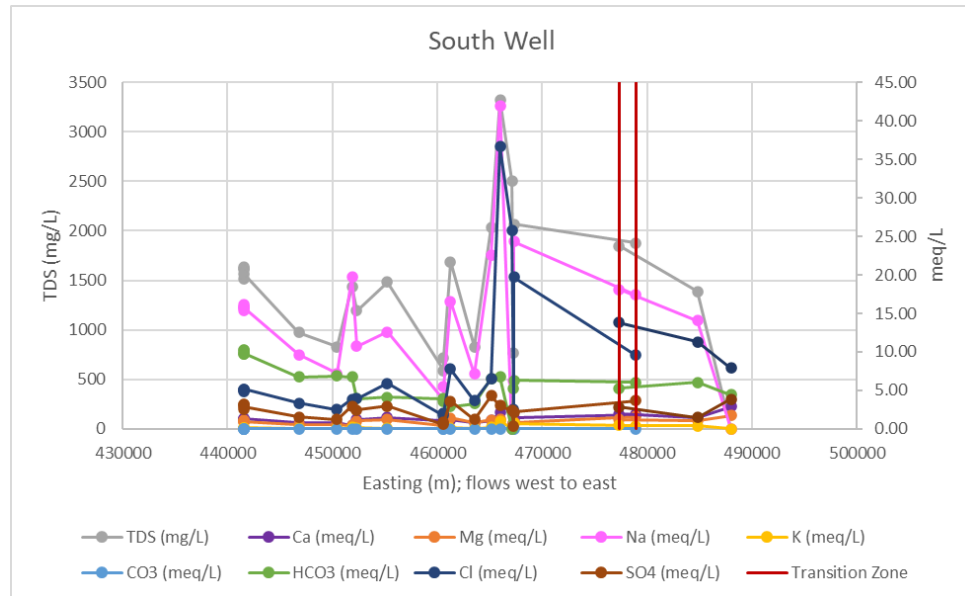


Figure 3.21: Mixing corrected radiocarbon ages with respect to calcium-to-sodium ratios and measured radiocarbon activities of groundwater samples along Antelope Draw



(a) Figure 3.22a Antelope Draw: Chemistry changes along flow path from west to east and corresponding Piper diagram; red vertical lines on components plot designate transition zone moving from Cretaceous geologic province into the Victorio Peak geologic province; Piper diagram points are color-coded to distinguish W.Antelope (light green) and E.Antelope (dark green); all concentrations are in meq/L, with the exception of TDS (mg/L); points on the Piper diagram are sized by TDS; lines on Piper diagram designate general trends in chemistry



(a) Figure 3.23a South Well Draw: Chemistry changes along flow path from west to east and corresponding Piper diagram; red vertical lines on components plot designate transition zone moving from Cretaceous geologic province into the Victorio Peak geologic province; Piper diagram points are color-coded to distinguish W.South Well (white with gray outline) and E.South Well (gray); all concentrations are in meq/L, with the exception of TDS (mg/L); points on the Piper diagram are sized by TDS; lines on Piper diagram designate general trends in chemistry

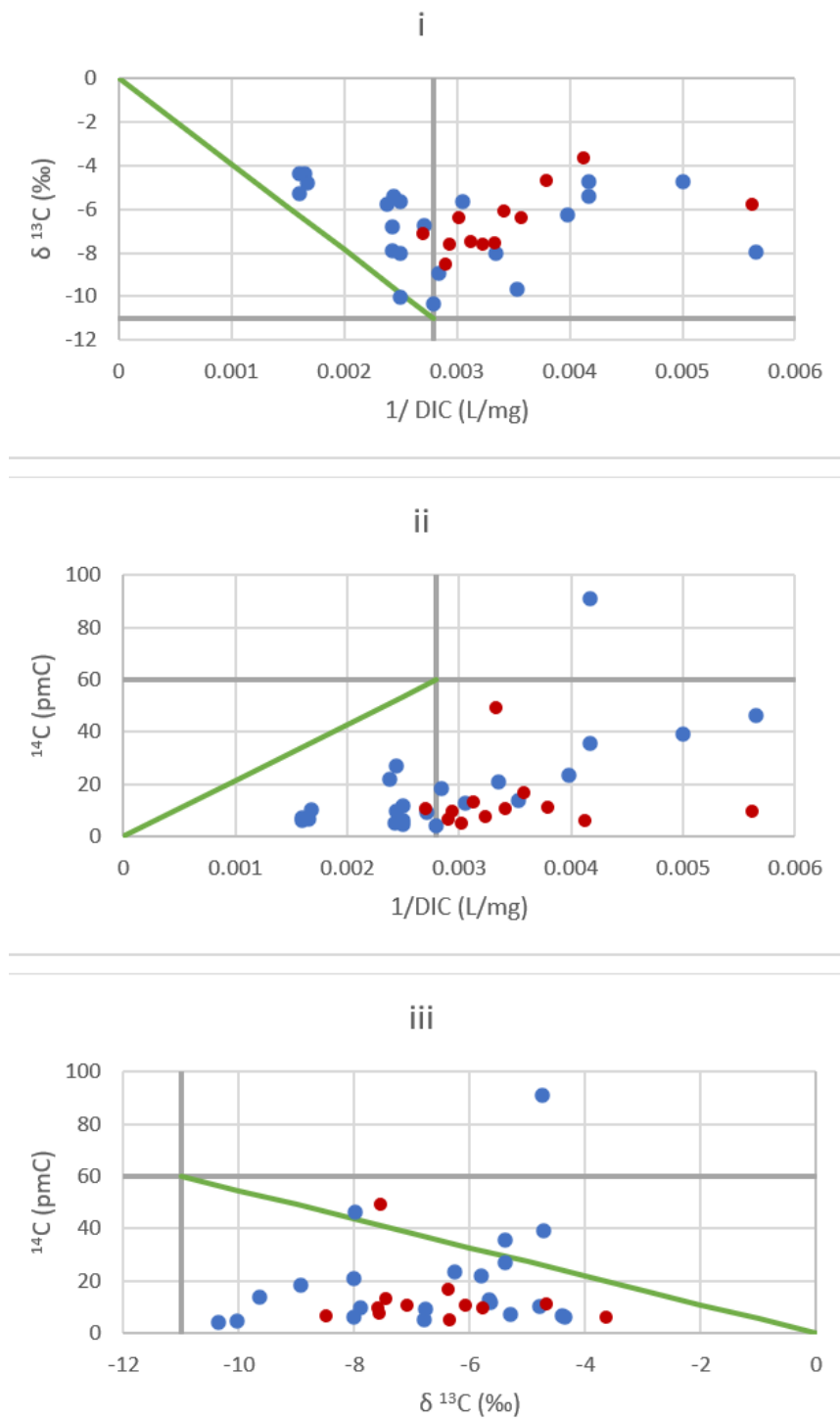
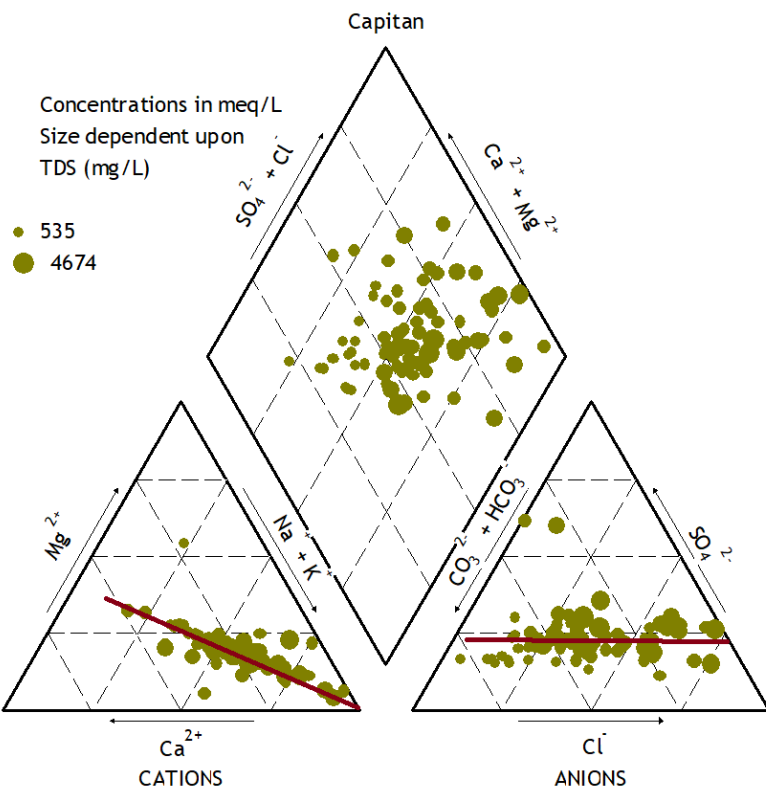
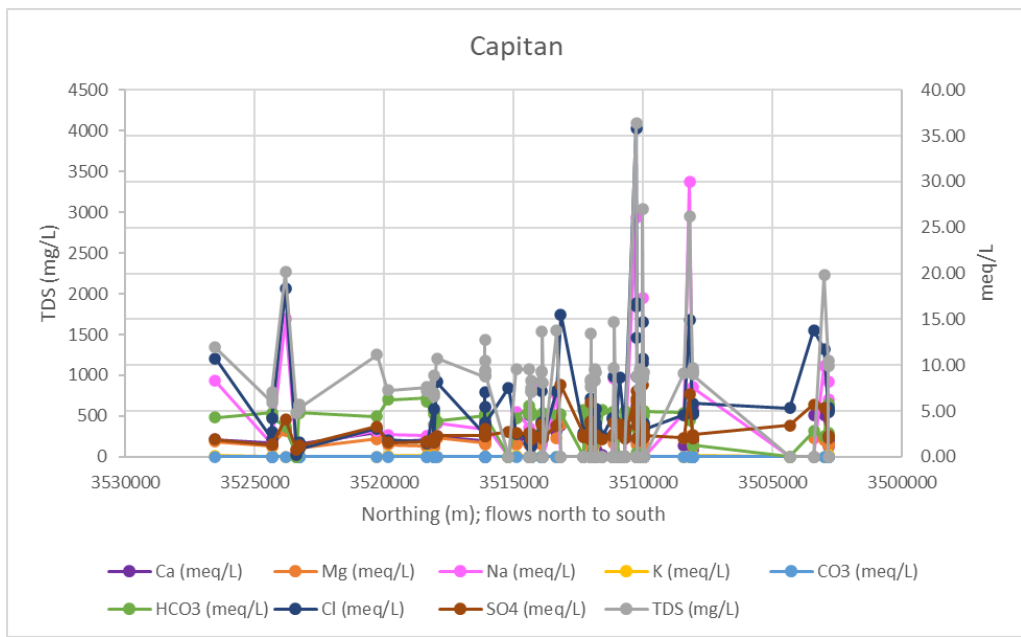


Figure 3.24: TX Victorio Peak carbon data plotted onto three carbon data interpretation graphs, to match Han et al., 2012 [2]



(a) Figure 3.25a Capitan Reef: Chemistry changes along flow path from north to south and corresponding Piper diagram; all concentrations are in meq/L, with the exception of TDS (mg/L); points on the Piper diagram are sized by TDS; lines on Piper diagram designate general trends in chemistry

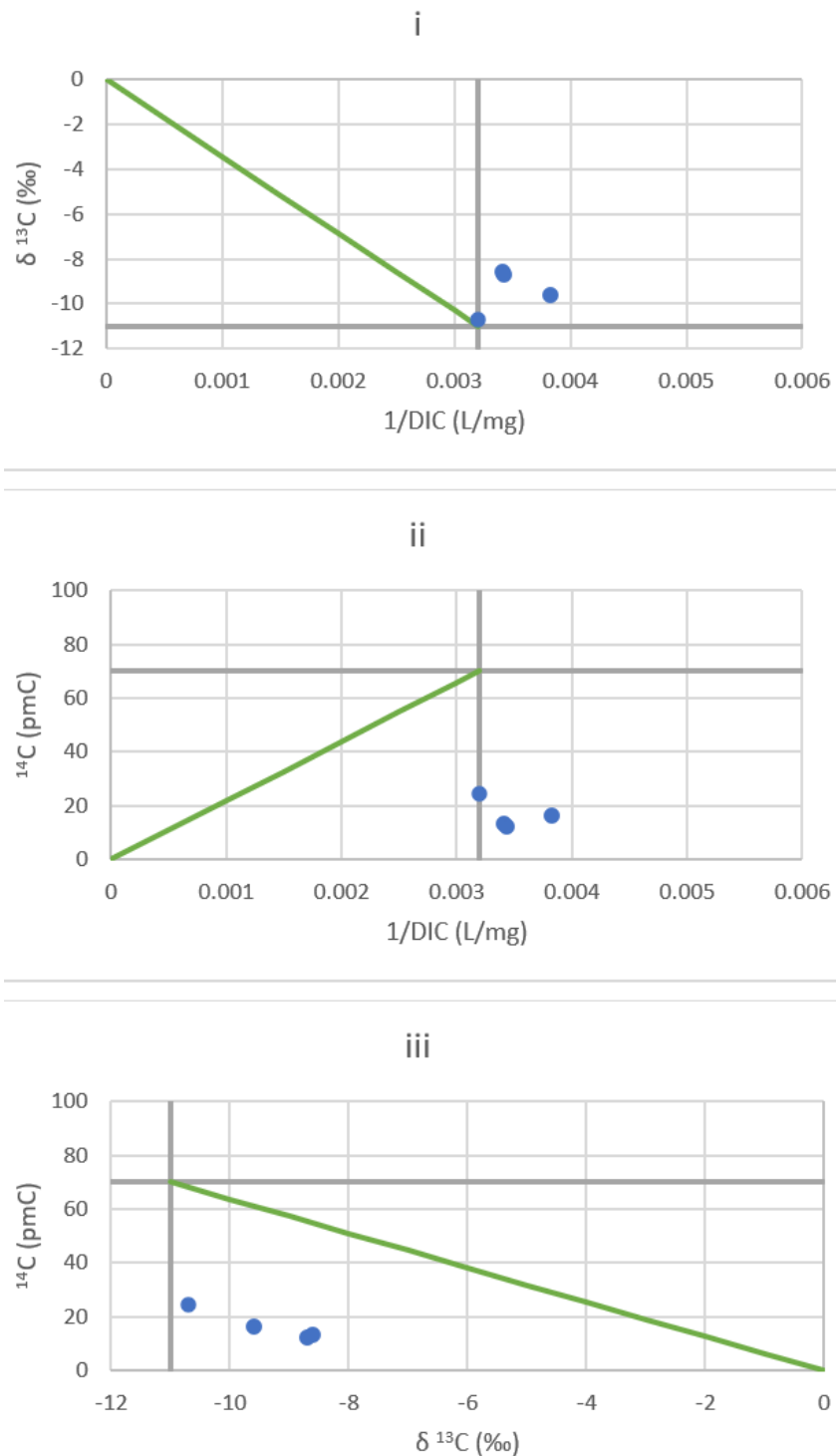
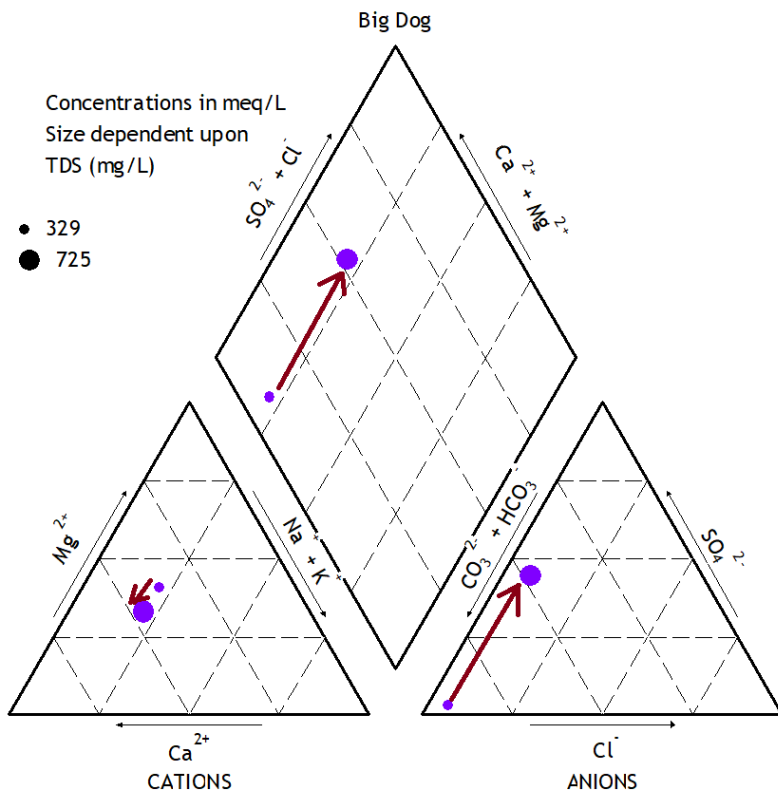
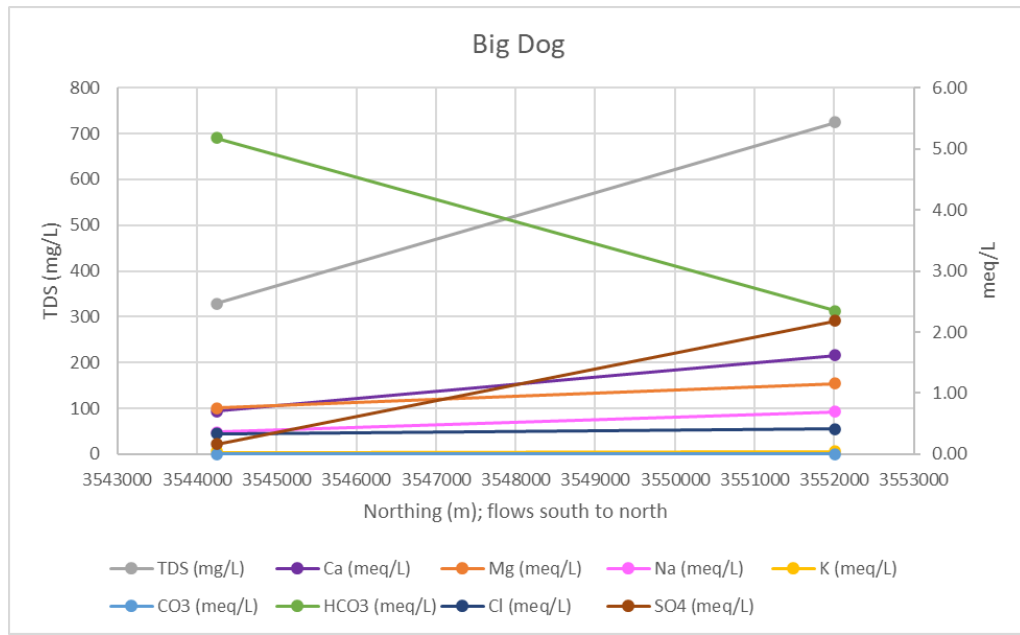
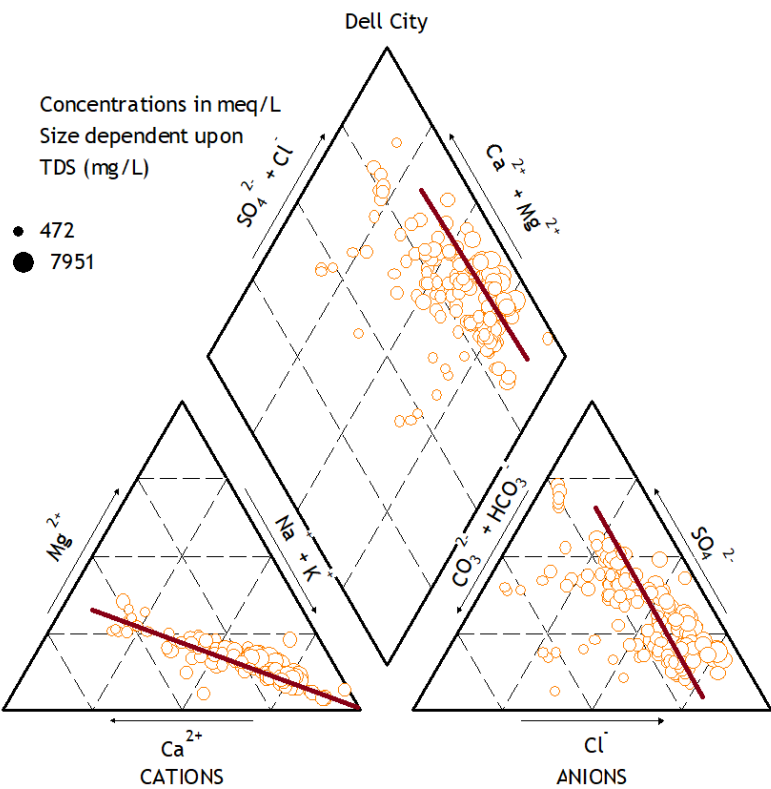
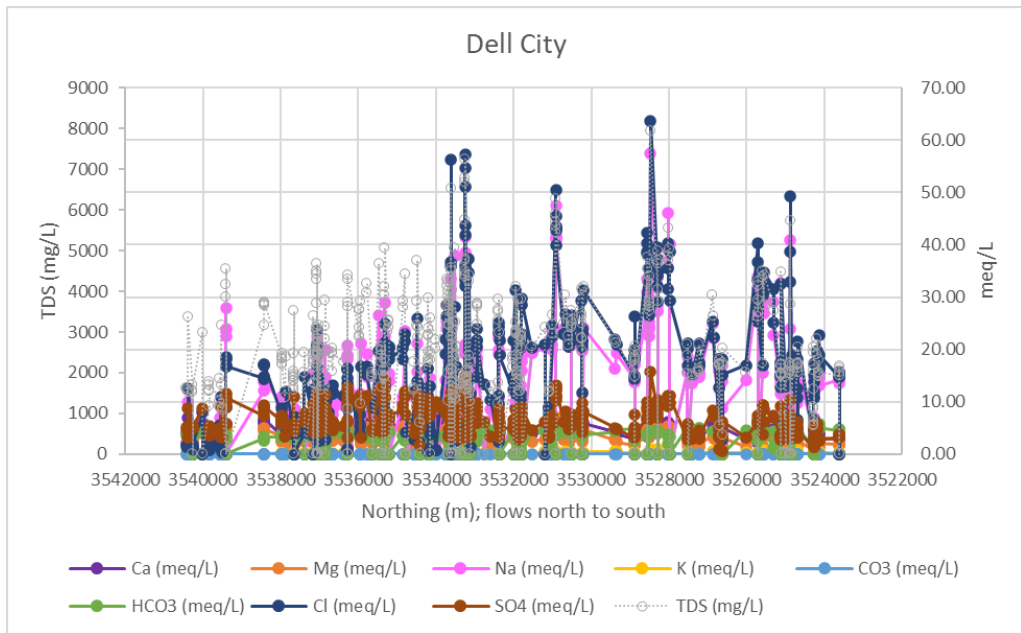


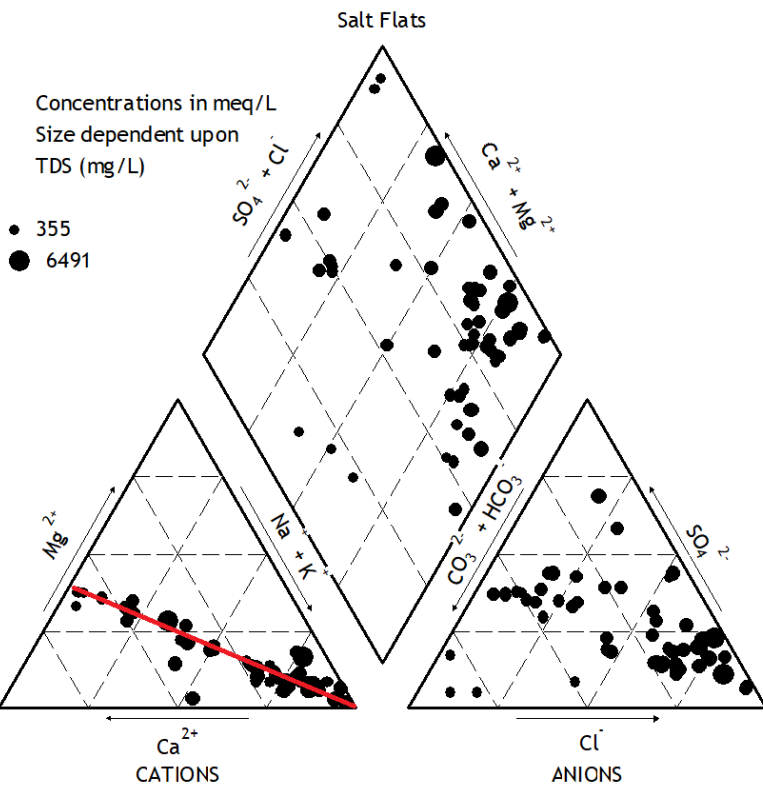
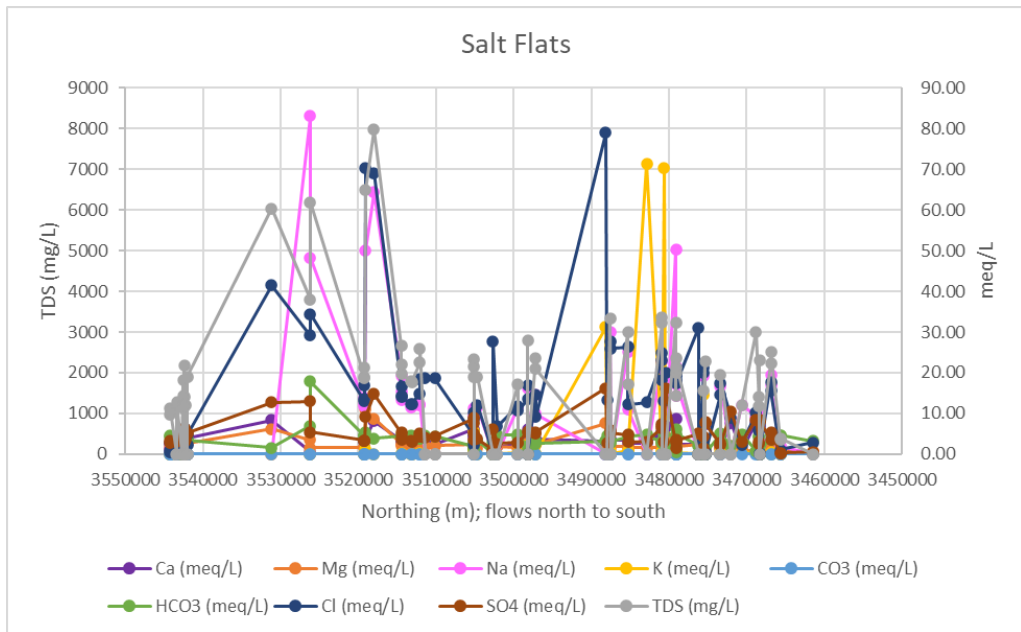
Figure 3.26: TX Capitan Reef carbon data plotted onto three carbon data interpretation graphs, to match Han et al., 2012 [2]



(a) Figure 3.27a Big Dog Canyon: Chemistry changes along flow path from south to north and corresponding Piper diagram; all concentrations are in meq/L, with the exception of TDS (mg/L); points on the Piper diagram are sized by TDS; lines on Piper diagram designate general trends in chemistry



(a) Figure 3.28a Dell City,TX: Chemistry changes along flow path from north to south and corresponding Piper diagram; all concentrations are in meq/L, with the exception of TDS (mg/L); points on the Piper diagram are sized by TDS; lines on Piper diagram designate general trends in chemistry



(a) Figure 3.29a TX Salt Flats: Chemistry changes along flow path from north to south and corresponding Piper diagram; all concentrations are in meq/L, with the exception of TDS (mg/L); points on the Piper diagram are sized by TDS; lines on Piper diagram designate general trends in chemistry

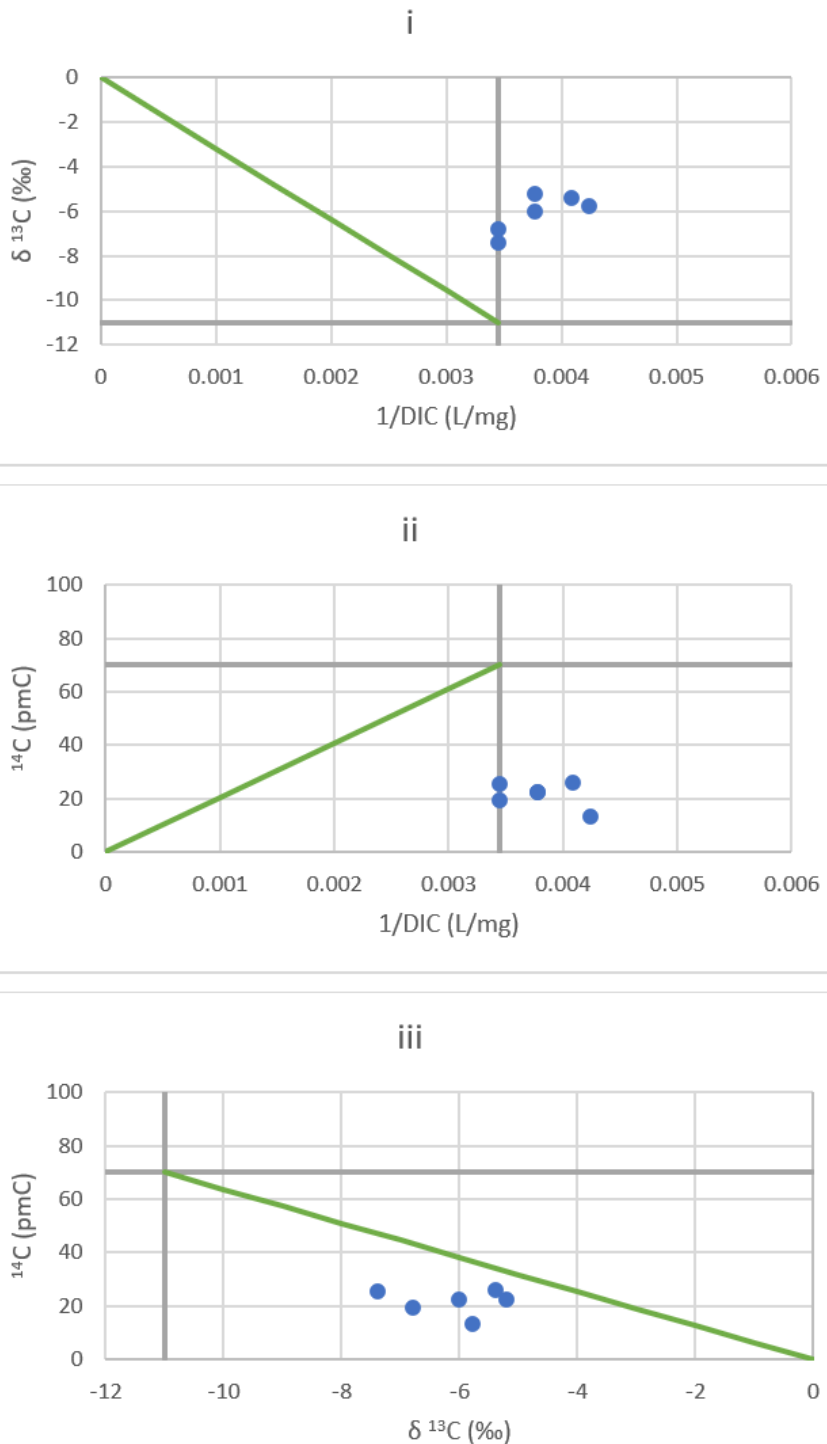


Figure 3.30: TX Salt Flats carbon data plotted onto three carbon data interpretation graphs, to match Han et al., 2012 [2]

CHAPTER 4

GROUNDWATER CHEMISTRY DISCUSSION

4.1 NM Carbonates Chemistry Trends

Chemical evolutionary trends in the northern Salt Basin, specifically for the Piñon Creek flow path, matched those previously established (Figure 4.1a; [14]). The Piñon Creek, Sacramento River, and Cornucopia Draw generally follow an expected increase in constituents nearer to Dell City and the playas discharge area. The exception to this trend is a plateauing ratio of one-to-one magnesium to calcium that is associated with dedolomitization (Figure 3.4). There is also a decrease in bicarbonate, constant chloride, and increasing sulfate. The increasing dominance of sulfate due to gypsum dissolution as part of dedolomitization is shown in Figure 3.3. Calcium is being released with gypsum dissolution, but reconstituted into calcite. Additional calcium and magnesium are released with dolomite dissolution. Figure 3.5 shows the dominance of magnesium instead of sodium. The bicarbonate is incorporated into the precipitated calcite and the sulfate is released from the dissolution of gypsum.

The Han plots for the NM Carbonates geologic province also show the dedolomitization trend with the majority of the carbon points plotting within Region 2 and Region 6. Dedolomitization releases carbon-13 from the gypsum and dolomite minerals and incorporates heavier carbon-12 into the precipitating calcite. This process results in the trend of enriching $\delta^{13}\text{C}$, decreasing radiocarbon percent modern carbon, and a decrease in dissolved inorganic carbon (an increase in 1/DIC) shown by the red trend lines in Figure 4.2. The few points that are outside of Region 2 and Region 6 still align with the general dedolomitization trend and further suggest a mixing of groundwater sources. This mixing of sources is due to the multiple flow paths with carbon data within the NM Carbonate geologic province. The majority of the carbon points from within this geologic province are along Piñon Creek, but there are a few carbon data points within Cornucopia Draw and Shiloh Draw.

Sigstedt (2010) [14] concluded dedolomitization was the dominant process in New Mexico carbonates and made a radiocarbon correction specific to that process. Since the chemistry analyzed in this study corroborates dedolomitization as a dominant process, the correction radiocarbon ages from Sigstedt (2010) [14] are likely more accurate than the general Fontes and Garnier correction method applied in this study. The Fontes and Garnier correction method accounts for

isotopic exchange, but does not account of incongruent dissolution associated with dedolomitization. Isotopic exchange switches carbon-13 for carbon-12 in the minerals. The released carbon-13 will produce a slightly enriched groundwater that suggests a small initial radiocarbon activity and thus, a younger groundwater. The incongruent dissolution dissolves out carbon-13 and precipitates carbon-12, which produces a carbon-13 enriched groundwater. This enriched groundwater would suggest a higher initial radiocarbon activity that has decayed over a longer time span. Hence, incongruent dissolution would produce older groundwaters than just isotopic exchange will estimate. Consequently, the F&G corrections are likely underestimates of groundwater age and the dedolomitization correction performed by Sigstedt (2010) [14] is more reliable.

The groundwaters of the Sacramento River, Piñon Creek, and Cornucopia Draw converge and discharge into Dell City, TX before reaching the Salt Flats. This convergence is evident in the Piper diagram of the three flow paths' data points with a few of the northern Dell City data points (Figure 4.3). The Dell City points are constrained at the end of the dedolomitization chemical evolution pathway with a low bicarbonate, low chloride, high sulfate, and a near one-to-one ratio of magnesium to calcium. The dedolomitization evolutionary pathway is added onto Figure 4.3 as arrows.

The Shiloh Draw is the last flow path within the NM Carbonate geologic province. This flow path is separated out due to the variability in constituents, which is likely due to the Cornudas Mountains. The Piper diagram of Shiloh Draw appears to have a loose dedolomitization trend, but has a distribution of calcium and sulfate concentrations. Figure 4.4 highlights this overall dedolomitization trend and potential mixing lines due to the Cornudas Mountains groundwater. This mixing trend line has constant bicarbonate, increasing chloride and decreasing sulfate. The Cornudas Mountains create potentiometric highs that redirect the Shiloh Draw flow path and introduce recently recharged, silicious waters with low calcium concentrations. The igneous rocks of the Cornudas Mountains, phonolite and syenite, are mafic silicate rocks. Consequently, dissolution of this igneous rock would contribute magnesium and silica to the Shiloh Draw groundwater. A contribution of magnesium and silica from the mountains dilutes the calcium and sulfate from dissolution of the carbonate aquifer and interbedded gypsums. This mixture of waters is difficult to quantify because the silicious end member resides in the Cornudas Mountains where there are no groundwater wells. This is a possible future expansion of this project. If the Cornudas Mountain silicious end member was known, then a mixing model could be applied to the Shiloh Draw data points. This would contribute to a more complete groundwater chemical analysis.

4.2 TX Cretaceous Chemistry Trends

The Antelope Draw and South Well Draw begin in the southwestern Salt Basin in the Cretaceous geologic province. This area is underlaid by the coarsely

fractured Cretaceous limestone and rhyolite. These fractures produce a small amount of fractured flow, but the spacing between fractures in general is too large to create a preferential flow system. Based on this fracture network, Kreitler (1986) [54] suggested that there would be no prevalent chemical evolutionary trends. This idea is supported by the seemingly random constituents' trends of Figure 3.22a and Figure 3.23a and variable total dissolved solid concentrations.

The radiocarbon ages of the Cretaceous geologic province fail to align with any given flow path with the Fontes and Garnier radiocarbon correction and mixing correction. Older waters tend to have slightly more TDS in comparison to the younger waters. It is expected that younger waters have higher tritium concentrations due to more recent recharge. However, the tritium data of these data points has no such pattern (Figure 4.5). The carbon data points in the Antelope Draw and South Well Draw were collected in 1986 by Kreitler. This is early enough that bomb tritium from 1950's stratospheric nuclear bomb testing contributed additional radiocarbon and tritium to the groundwaters. Following this logic would explain the disconnect between radiocarbon and tritium patterns as the two peaks were not identical [77]. The point with anomalously high radiocarbon activity in Figure 4.6 is likely due to bomb pulse radiocarbon.

The chemical randomness aligns with the explanation of a mixing of waters through different pathways. In one major group of flow paths, groundwater gets trapped in the aquifer matrix blocks between fractures and chemically evolves in-place, resulting in high TDS. In an alternative flow path group, groundwater is recharged through fractures where it quickly moves through the system without much chemical evolution, resulting in low TDS. These waters are mixed naturally as the high TDS water diffuses into the fractures, and are also mixed anthropogenically as groundwater is extracted through water wells, lowering head and driving water from the matrix.

This fracture mixing is unique to the Texas portion of the Salt Basin, but the tectonic fractures extend throughout the basin. Mayer (1995) [40] analyzes the role of fractures in the groundwater flow system within the northern Salt Basin. That study concluded that the Otero Break fracture network acts as a conduit for recharge from the Sacramento Mountains to Dell City, TX. The high volume of water being transported along the Otero Break induces karstification and high conductivity flow paths [40]. This phenomenon cannot be replicated in Antelope Draw and South Well Draw due to the small volumes that recharge in this area. Both of these draws are included in the Texas-wide polygon used in the chloride-mass-balance method with PyRANA, which will be discussed in further detail later. The estimated recharge density is not large enough to force the Antelope Draw and South Well Draw system from a fracture-matrix mixing system to a purely fracture-controlled system, as in the northern Salt Basin.

The two-water mixing contains additional chemical processes within the aquifer matrix. Figure 4.6 shows two additional trends on the Han plots for the Cretaceous geologic province. As shown in the NM Carbonate geologic province, the red line designates the incongruent dissolution dedolomitization trend within the Cretaceous geologic province. The carbon data points along the red trend

line are within Region 2 and Region 6. Dedolomitization releases carbon-13 from the gypsum and dolomite minerals and incorporates heavier carbon-12 into the precipitating calcite. This process results in the trend of enriching $\delta^{13}\text{C}$, decreasing radiocarbon percent modern carbon, and a decrease in dissolved inorganic carbon (an increase in 1/DIC). Figure 3.4 also supports minor dedolomitization by showing a calcium-to-magnesium ratio of one-to-one.

A loose dedolomitization trend, with lower calcium and magnesium concentrations, and the calcium-to-magnesium one-to-one ratio trend are also highlighted on the W.Antelope and W.South Well Draw Piper diagram (Figure 4.7). There is a general trend towards decreasing bicarbonate, increasing chloride, constant sulfate, increasing calcium, increasing magnesium, and decreasing sodium and potassium. Due to the lack of calcium and magnesium, dedolomitization is a minor process in the Cretaceous geologic province.

The second trend on the Han plots for the Cretaceous geologic province is highlighted in graph i and graph ii with the blue circle around the carbon data points (Figure 4.6). These points are along the vertical axis, which suggest a mixing of carbon sources. This mixing is more prominent in the Cretaceous geologic province carbon data in comparison to the mixing of sources within the NM Carbonate geologic province. The mixing of sources is consistent with the two-waters mixing system described to be within this province. The older waters with low radiocarbon activities tend to be enriched in $\delta^{13}\text{C}$. The younger waters with higher radiocarbon activities tend to be depleted in $\delta^{13}\text{C}$. Each water has similar dissolved inorganic carbon. These two waters mix and produce a range of $\delta^{13}\text{C}$ for the constant 1/DIC.

4.3 TX Victorio Peak Chemistry Trends

The Victorio Peak geologic province is to the east of the Cretaceous geologic province, but shares the same groundwater flow paths. Therefore, the chemistry trends of the Cretaceous geologic province transition into the chemistry trends of the TX Victorio Peak geologic province. Figure 4.8 highlights the dedolomitization trend and mixing grouping from the Cretaceous geologic province on the combined Han plots for the Cretaceous geologic province and the Victorio Peak geologic province. Figure 3.3, Figure 3.4, and Figure 3.5 show a dominance of gypsum-derived sulfate, a one-to-one ratio of calcium-to-magnesium, and a dominance of dolomite-derived magnesium, respectively. The Victorio Peak geologic province carbon data points align with these trends from the Cretaceous geologic province. Hence, dedolomitization, incongruent dissolution, and mixing of carbon sources continues into the Victorio Peak carbonate. However, the additional carbonate dissolution within the Victorio Peak geologic province further enriches the groundwater in $\delta^{13}\text{C}$. Despite this enrichment from the dissolution of carbonate, gypsum, and dolomite, the precipitation of calcite removes some carbon-12 from the groundwater. Hence, the dissolved inorganic carbon remains

relatively constant in comparison to the Cretaceous geologic province carbon data points. The larger distribution of points within the blue mixing circles is expected as two-water mixing system from the Cretaceous mixes with groundwater affected by Victorio Peak carbonate dissolution.

Since the radiocarbon corrections using the Fontes and Garnier method and mixing method in the Cretaceous geologic province failed to produce a flow path with age trends, there is no age trend within the TX Victorio Peak geologic province. Groundwater with different ages propagated from the Cretaceous two-water mixing system into the Victorio Peak geologic province.

Like the Piper diagram of the western flow paths, Figure 4.9 shows a loose dedolomitization trend continuing into the Victorio Peak geologic province from the Cretaceous. The one-to-one ratio of calcium-to-magnesium is also continued and designated with a trend line on the Piper diagram. Due to the overall lack of calcium and magnesium, dedolomitization is a minor process in the Victorio Peak geologic province. The transition from geologic provinces has an overall lower bicarbonate, higher chloride, higher sulfate, lower calcium, lower magnesium, and higher sodium and potassium. This trend could be explained with additional precipitation of calcite removing more bicarbonate and calcium, more dissolution of gypsum contributing more sulfate, and less dissolution of dolomite contributing bicarbonate, calcium, and magnesium. The chloride and sodium are likely due to halite dissolution and/or mixing with Salt Flat brines along the eastern margin of the Victorio Peak geologic province.

4.4 TX Capitan Reef Chemistry Trends

Along the eastern margin of the Salt Basin, the Capitan geologic province and corresponding flow path is a limestone system that is juxtaposed with the Salt Flats to the west. The location of the carbon points on the Capitan geologic province Han plots are in Region 2 and Region 6. These regions are associated with dedolomitization. Figure 3.3, Figure 3.4, and Figure 3.5 show a dominance of gypsum-derived sulfate, a one-to-one ratio of calcium-to-magnesium, and a dominance of dolomite-derived magnesium, respectively. Since the carbon points tend to be closer to the vertical axis on graph i and graph ii, it is likely that this dedolomitization trend is also representative of a mixing of carbon sources in the Capitan geologic province. Figure 4.10 highlights the general dedolomitization and mixing trend on the Han plots. The mixing of carbon sources is likely due to groundwaters originating in the Guadalupe Mountains/Brokeoff Mountains and flowing through either the Big Dog Canyon or Capitan flow paths. There is not a singular headwater for the Capitan flow path through the Capitan geologic province.

The four carbon data points within the Capitan geologic province have corrected radiocarbon ages. These ages were found using the Fontes and Garnier method to corrected for isotopic exchange. The corrected radiocarbon ages follow

an expected trend of increasing age further southwards. It is expected that once a groundwater becomes isolated from the atmosphere, the radiocarbon will decay at a constant rate. Further down the flow path, there should be less radiocarbon to coincide with an older groundwater age.

Despite the range of constituents in the Capitan geologic province, there is a slight dedolomitization trend with lower-than-expected calcium and magnesium (Figure 4.11). There is a general trend towards decreasing bicarbonate with increasing chloride and constant sulfate. The calcium-to-magnesium ratio is a one-to-one ratio, as expected for dedolomitization. Due to the lack of calcium and magnesium, dedolomitization is a minor process in the Capitan geologic province. Like the Victorio Peak geologic province, there is a trend of increased chloride with increased sodium and potassium. This is likely due to halite dissolution and/or brine mixing from the Salt Flats along the western and southern margin of the Capitan geologic province.

4.5 NM Artesia Group Chemistry Trends

The Big Dog Canyon within the Artesia Group geologic province has two representative points, thus making chemical evolutionary trends difficult to formulate. Due to the chemistry context of the rest of the Salt Basin and based on the location of the two data points on the Piper diagram, it is likely that there is dedolomitization occurring in the Artesia Group geologic province (Figure 4.12). Figure 3.3 supports the dedolomitization trend as it shows an increasing dominance of sulfate. However, it is possible that these two points do not represent dedolomitization along a flow path and rather represent gypsum dissolution within the Big Dog Canyon flow path. This would explain the decrease in bicarbonate, decrease in chloride, increase in sulfate, increase in calcium, decrease in magnesium, and no change in sodium and potassium. Figure 3.4 support this gypsum dissolution as it shows a dominance of calcium, rather than a one-to-one ratio of calcium-to-magnesium. Further, Figure 3.5 shows a dominance of sodium, which suggests a minimal amount of magnesium. This small concentration of magnesium is counter to the expected dedolomitization trend. Nonetheless, conclusions drawn from two data points have minimal certainty.

4.6 Dell City, TX Chemistry Trends

Dell City, Texas is located adjacent to the discharge area of the northern Salt Basin, and thus has a similar chemistry as Piñon Creek, Cornucopia Draw, and Sacramento River. As shown previously in Figure 4.3, the Dell City groundwaters are at the end of the dedolomitization trend associated with the end of the Piñon Creek, Cornucopia Draw, and Sacramento River flow paths. Figure 3.4 supports this end-of-dedolomitization trend with a calcium-to-magnesium ratio within Dell City of one-to-one.

Within Dell City, there is an increase in chloride with a decrease in sulfate as the groundwater moves southwards towards the Salt Flats (Figure 3.3). This trend is consistent with active irrigation and evapotranspiration in Dell City concentrating the chloride through irrigation return flow and a mixing with saline waters from the Salt Flats. This same brine mixing trend was highlighted in the Victorio Peak and Capitan geologic provinces. Figure 3.5 shows a shift from magnesium-dominated groundwaters, due to dedolomitization in the NM Carbonates geologic province, into sodium-dominated groundwaters, due to ET and Salt Flats brine mixing. The Piper diagram of Dell City (Figure 3.28a) is dominated by chloride and sulfate with a range of cations. Sodium and potassium are the most dominant cation, followed by calcium, and then magnesium.

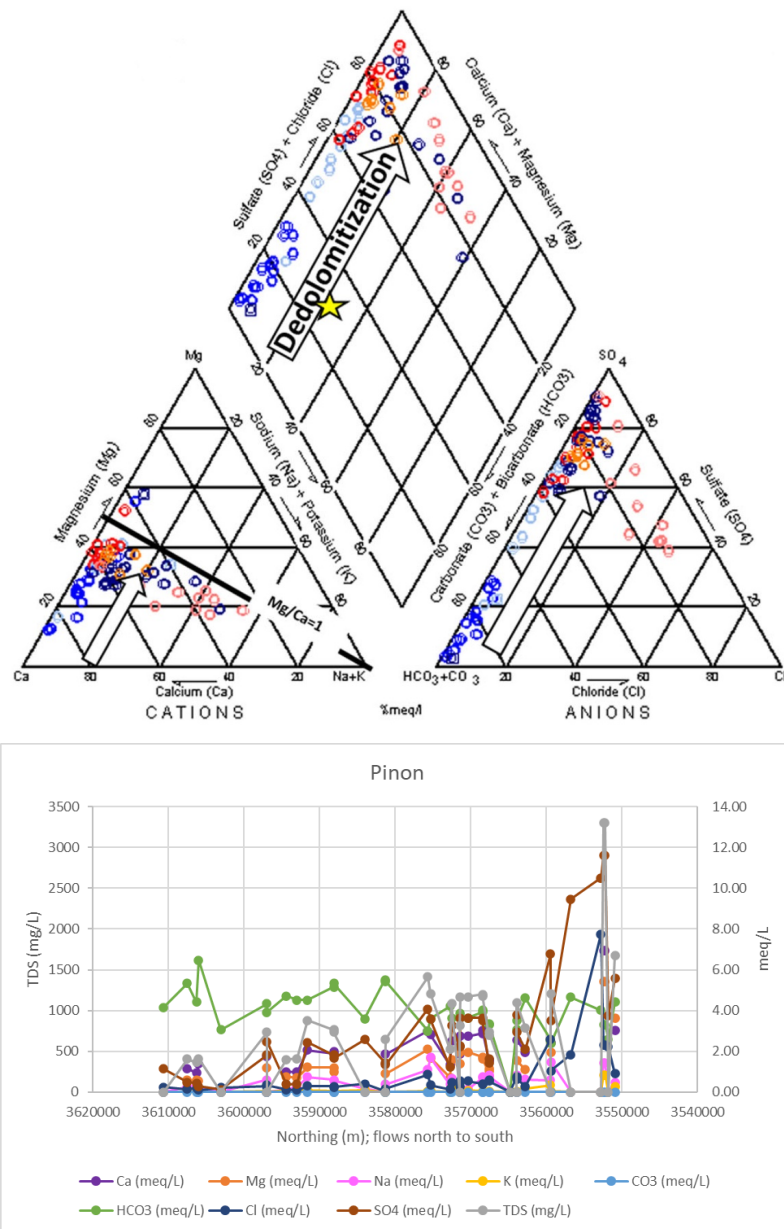
4.7 TX Salt Flats Chemistry Trends

The Salt Flats are the culmination of all of the flow paths throughout the Salt Basin. Hence, the chemistry of the Salt Flats should appear similar to the chemistry of all of the other geologic provinces. Figure 4.13 shows the Salt Flats' carbon data with respect to all of the Salt Basin carbon data grayed out behind it. The Salt Flats points are amongst the other carbon points from the rest of the Salt Basin within Region 2 and Region 6. For the Salt Flats, there is a dedolomitization trend that continues from the carbonate aquifers. Figure 3.4 has the continued one-to-one ratio of calcium-to-magnesium. Dedolomitization releases carbon-13 from the gypsum and dolomite minerals and incorporates heavier carbon-12 into the precipitating calcite. This process results in the trend of enriching $\delta^{13}\text{C}$, decreasing radiocarbon percent modern carbon, and a decrease in dissolved inorganic carbon (an increase in 1/DIC). There is a range of dissolved inorganic carbon concentrations due to the convergence of multiple groundwater sources into the Salt Flats. The highlighted carbon data best align with the diamond points in Figure 4.13. These symbols designate carbon data from the NM Carbonate geologic province. The dominance of the NM Carbonate geologic province in the cumulative chemistry of the Salt Flats suggests that the flow paths through the NM Carbonate geologic province carry the largest volume of groundwater. These flow paths would be the Piñon Creek, Cornucopia Draw, Sacramento River, and Shiloh Draw.

Due to the active agriculture and irrigation of the Dell City area, the radiocarbon system is not fully closed within the playas to the northeast of Dell City. Instead, the groundwater is partially aerated and radiocarbon is reintroduced into the groundwater through irrigation return flow. Because of this process, the radiocarbon activities with the northern Salt Flats correspond to relatively young groundwater ages (Figure 3.9). High activities of radiocarbon in the system that has not decayed suggests an overall younger water that was recently recharged into the groundwater system and isolated from the atmosphere. Starting with this young water in the north, the southern Salt Flats have older waters that have decayed over the length of the flow path. The seemingly anomalous younger

radiocarbon age in the southern Salt Flats may be due to mixing of younger waters from the Cretaceous and Victorio Peak geologic provinces.

As expected, the chemistry of the Salt Flats reflects the combination of the other flow paths through different geologic provinces (Figure 4.14). The Piper diagram of the Salt Flats shows the same calcium-to-magnesium one-to-one ratio seen throughout the Salt Basin. The anions of the Salt Flats have a slight trend of increasing chloride with decreasing bicarbonate and decreasing sulfate. Figure 3.3 also shows this dominance of chloride with respect to sulfate. This trend is consistent with the production of evaporites such as gypsum and dolomite on the playa surface. The salts are carried upwards to the surface from the groundwater via capillary rise. Once near the surface, the water is evaporated away and leaves behind the salts. Due to the high concentrations of chloride and sodium in the Salt Flats groundwater, it is likely that halite is not a common evaporite on the playa surface. Instead, the chloride and sodium remain in solution as a brine. Figure 3.5 shows the dominance of sodium with respect to magnesium in the Salt Flats. This brine extends outwards from the Salt Flats and mixes with groundwater in the Victorio Peak, Capitan, and Dell City geologic provinces.



(a) Figure 4.1a Comparison between Piñon Creek Piper diagram from this study (also in Figure 3.11a) and from Sigstedt (2010) [14]; right: linear trend indicating increasing magnesium and sulfate concentrations indicative of dedolomitization [14]

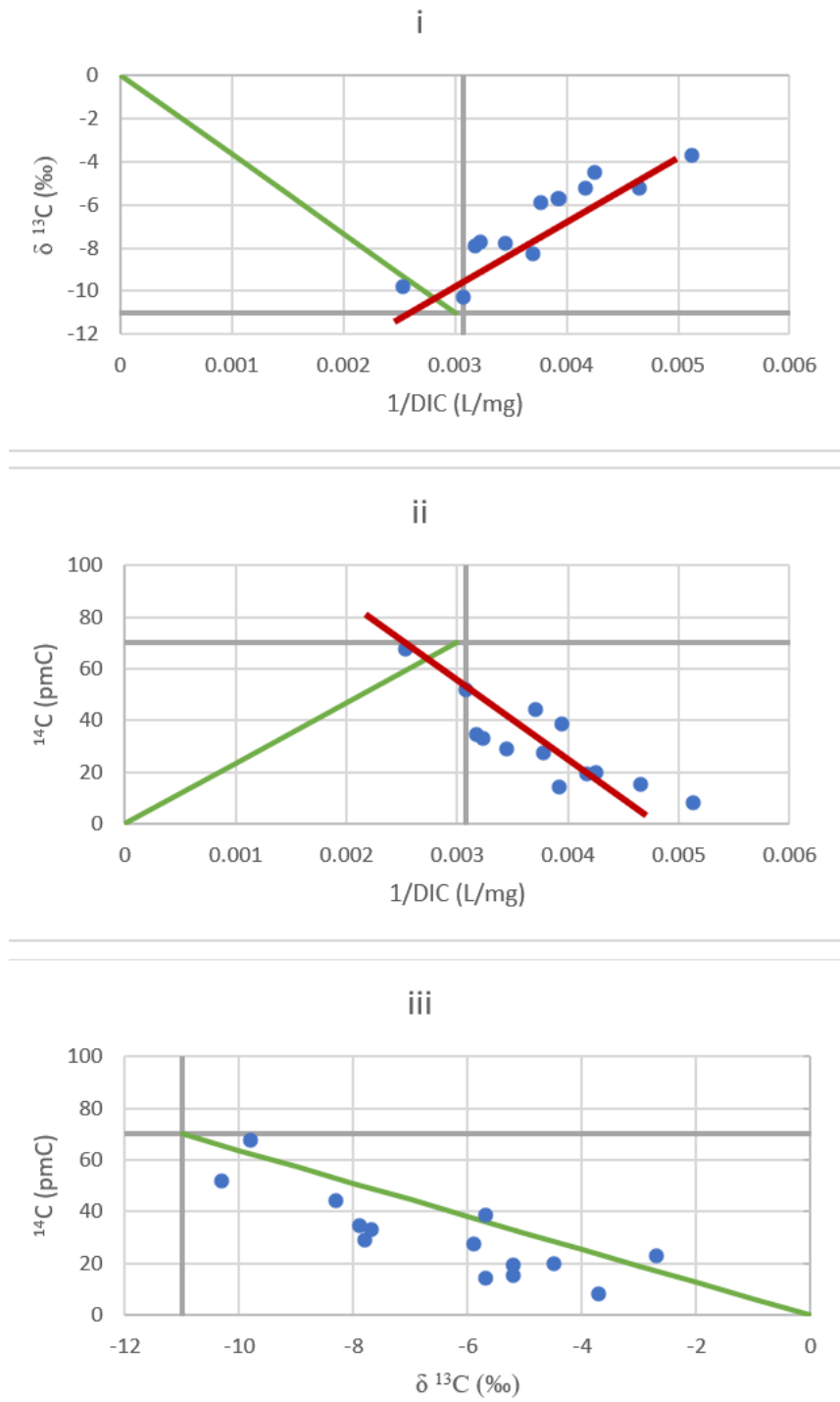


Figure 4.2: NM Carbonates carbon data plotted onto three carbon data interpretation graphs, to match Han et al., 2012 [2]; red trend lines designate dedolomitization trend

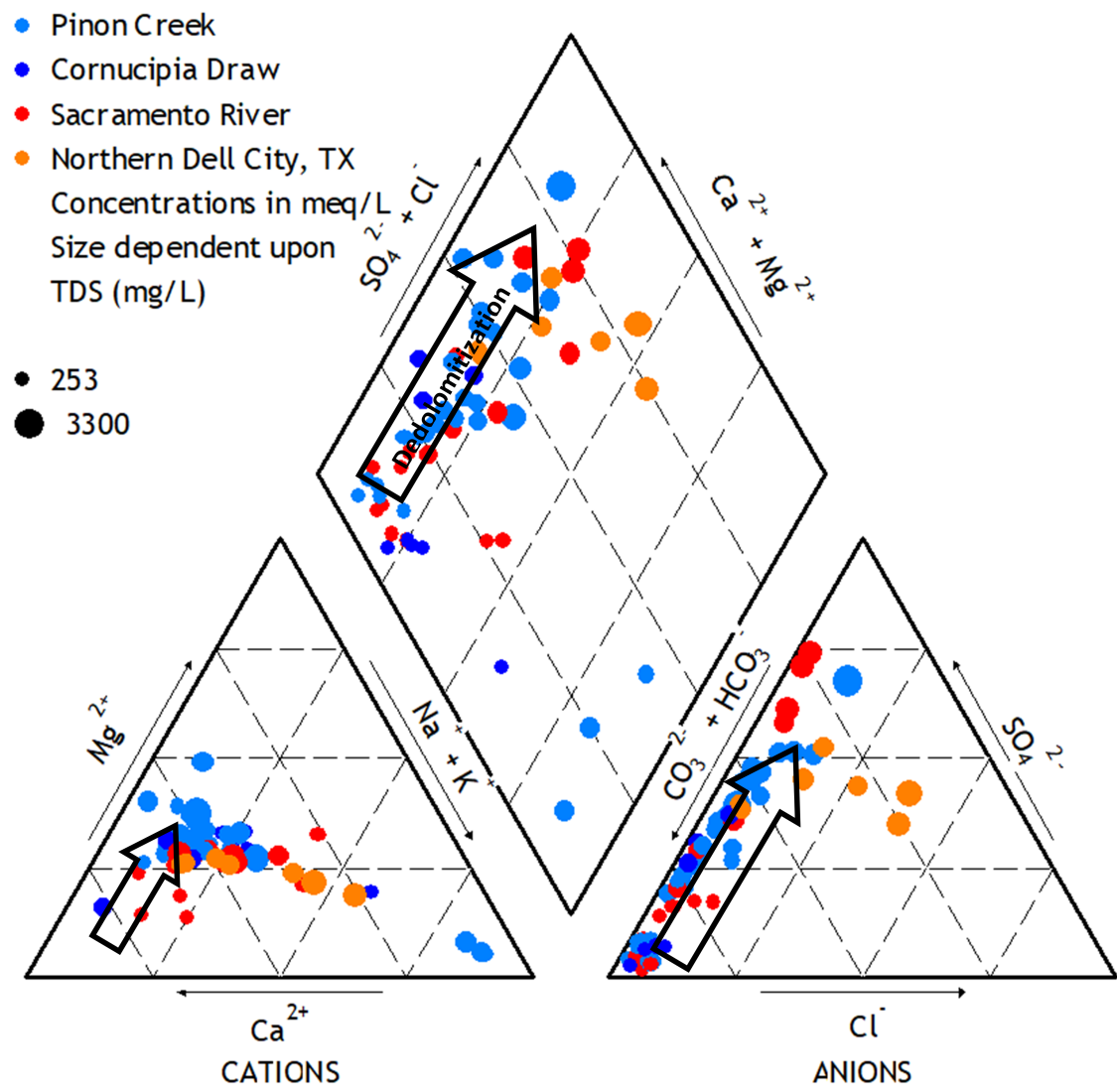


Figure 4.3: Piper diagram of chemistry points from Piñon Creek, Cornucopia Draw, Sacramento River, and northern Dell City, TX, as denoted by color; size of the point is scaled by TDS concentration; arrows show direction of dedolomitization trend as described in Back (1983) [75]

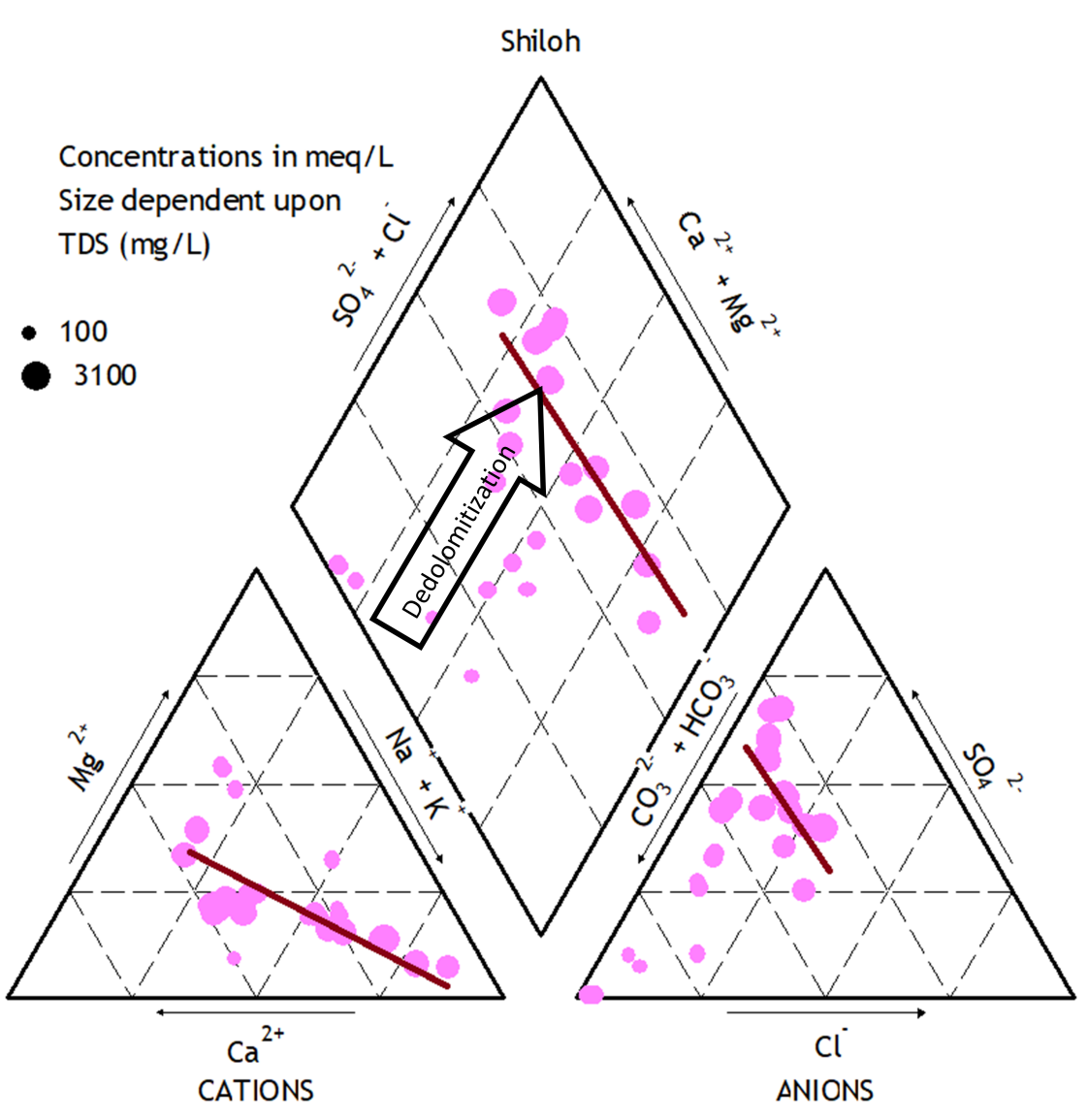


Figure 4.4: Piper diagram of chemistry points from Shiloh Draw (also in Figure 3.14a); size of the point is scaled by TDS concentration; arrow is indicative of dedolomitization; red lines suggest mixing with siliceous waters from the Cornudas Mountains

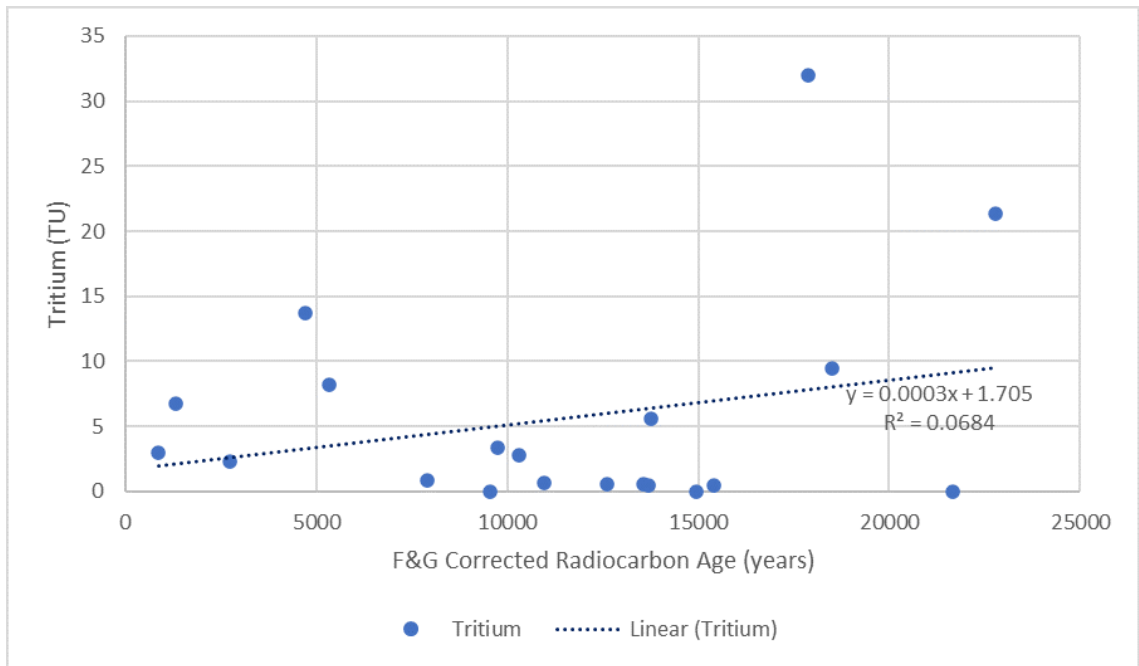


Figure 4.5: Tritium concentrations with respect to Fontes and Garnier corrected radiocarbon ages for Cretaceous geologic province; tritium in Tritium Units (TU); R value and equation for linear trend line of tritium points provided

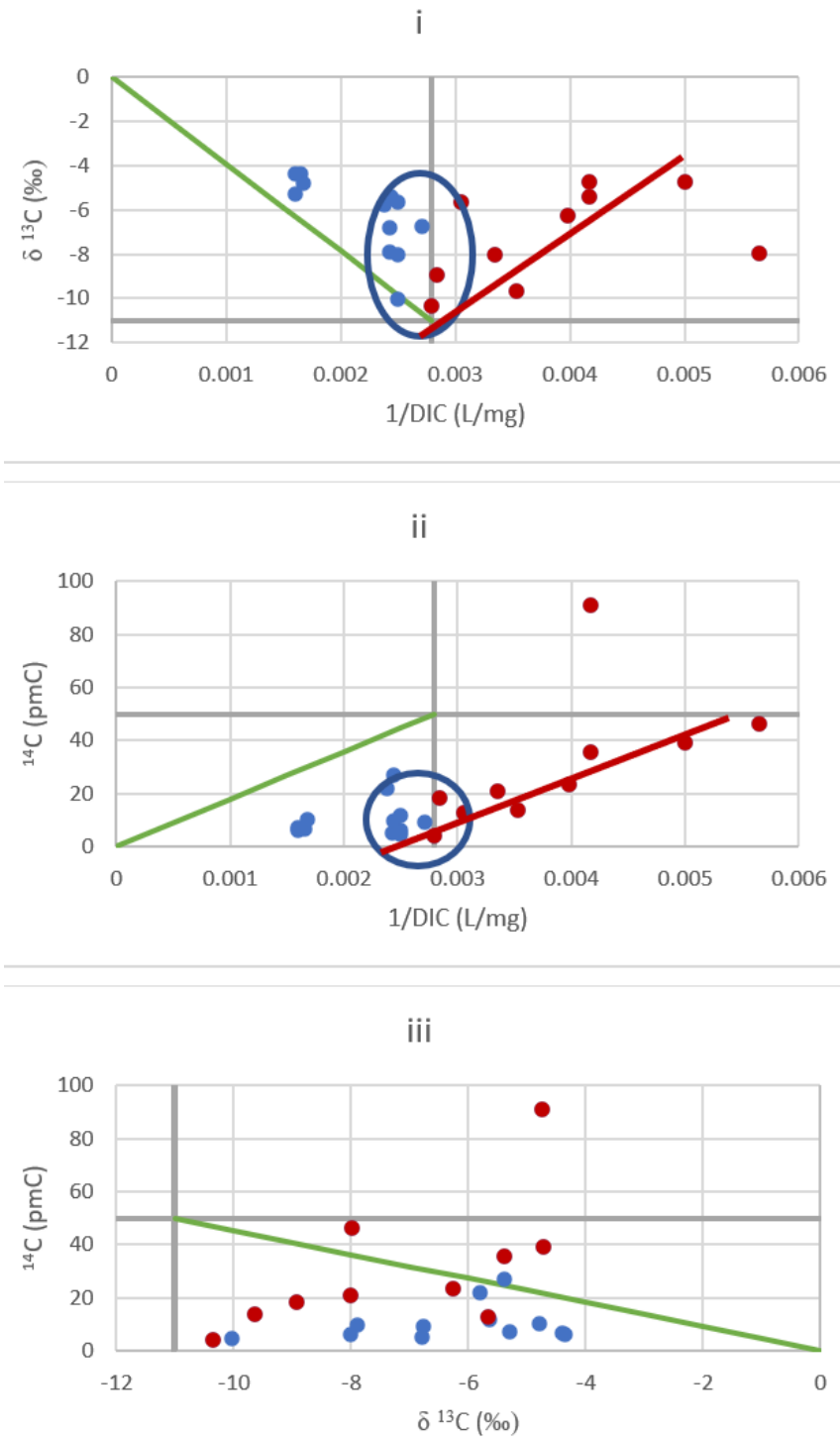


Figure 4.6: TX Cretaceous carbon data plotted onto three carbon data interpretation graphs, to match Han et al., 2012 [2]; red trend lines designate dedolomitization trend; blue circles designate mixing of carbon sources

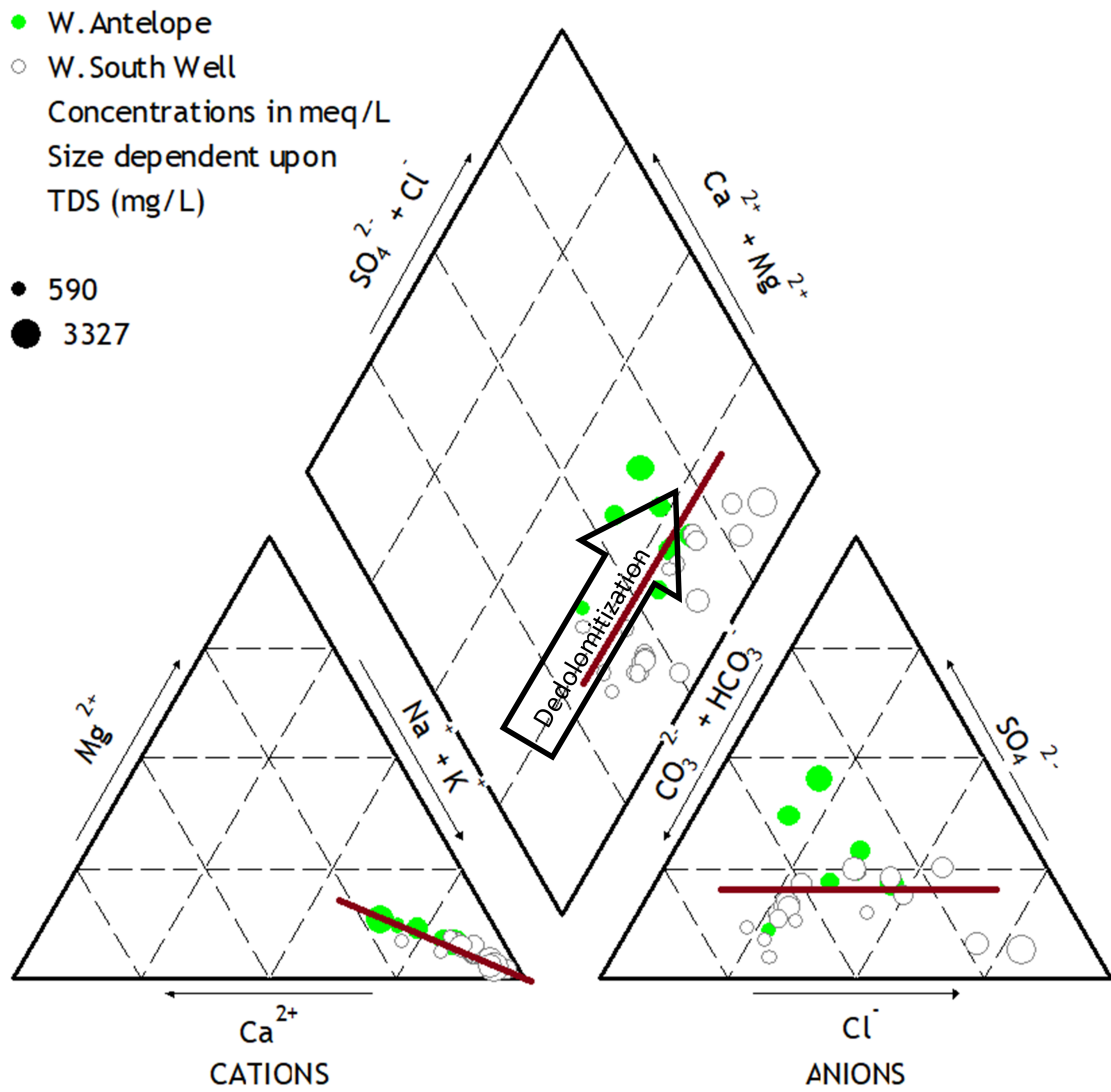


Figure 4.7: Piper diagram of chemistry points from Cretaceous; size of the point is scaled by TDS concentration; arrow is indicative of dedolomitization; red lines suggest mixing with Salt Flats brine

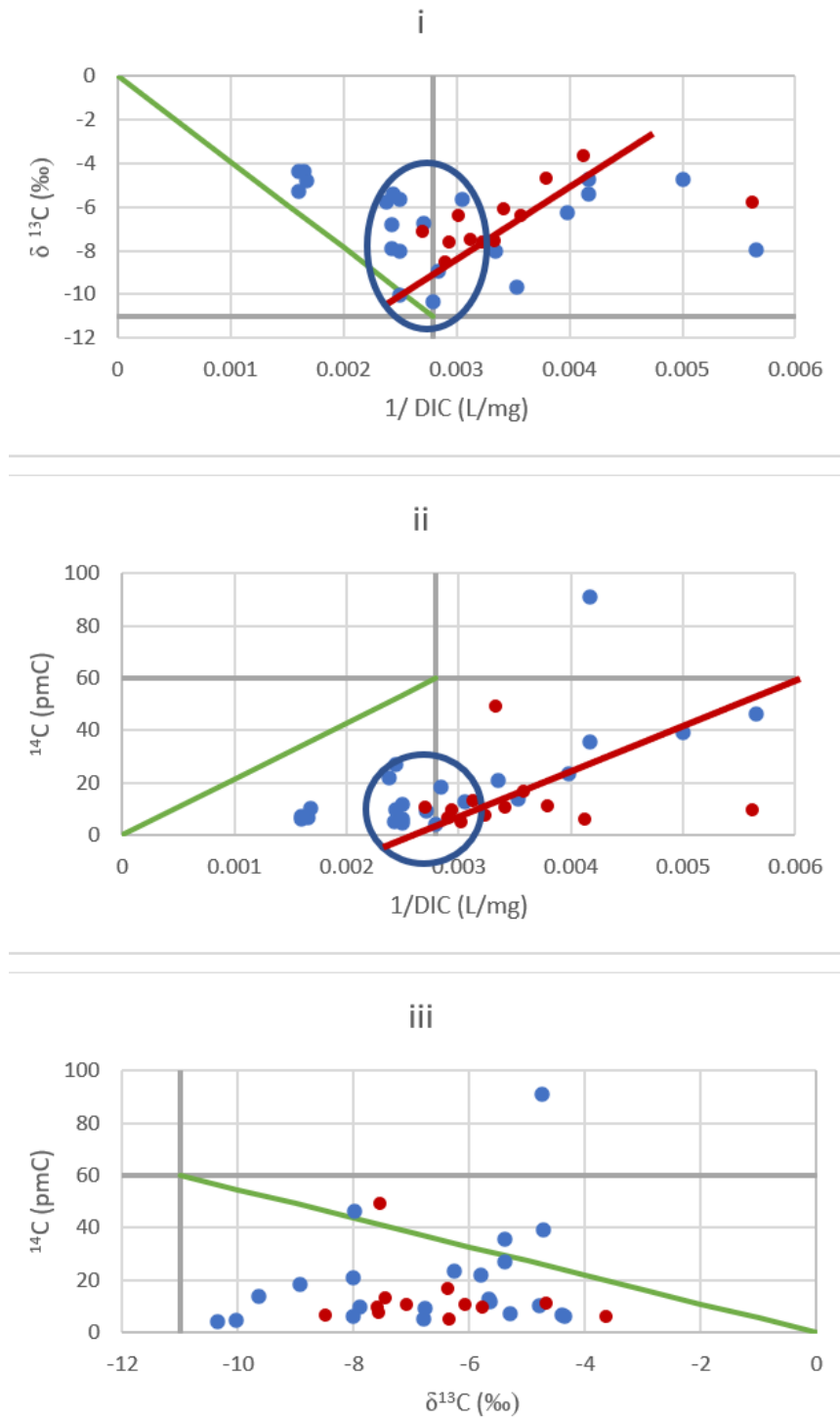


Figure 4.8: TX Victorio Peak carbon data plotted onto three carbon data interpretation graphs, to match Han et al., 2012 [2]; red trend lines designate dedolomitization trend; blue circles designate mixing of carbon sources

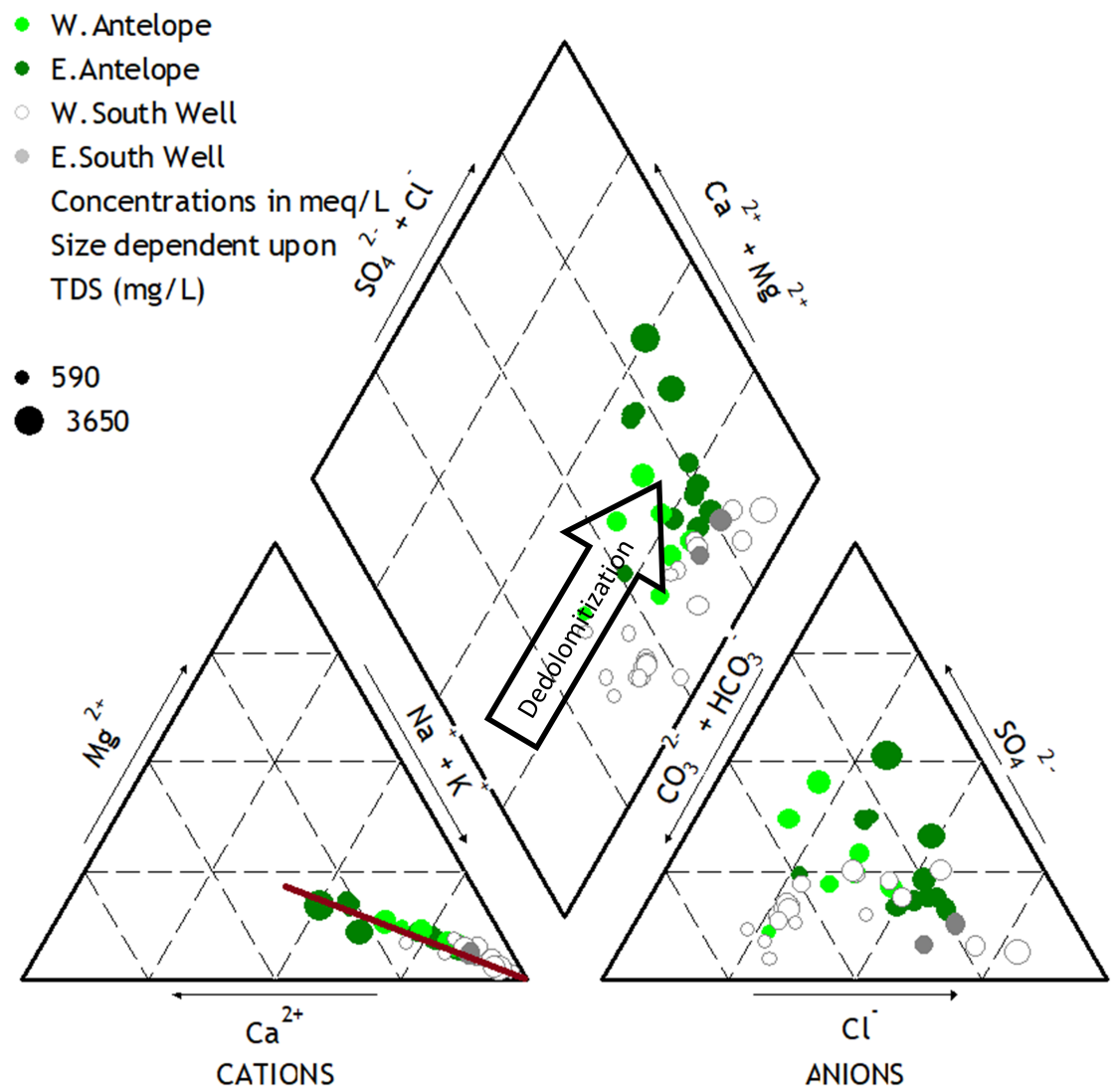


Figure 4.9: Piper diagram of chemistry points from Victorio Peak; size of the point is scaled by TDS concentration; arrow is indicative of dedolomitization; red lines suggest mixing with Salt Flats brine

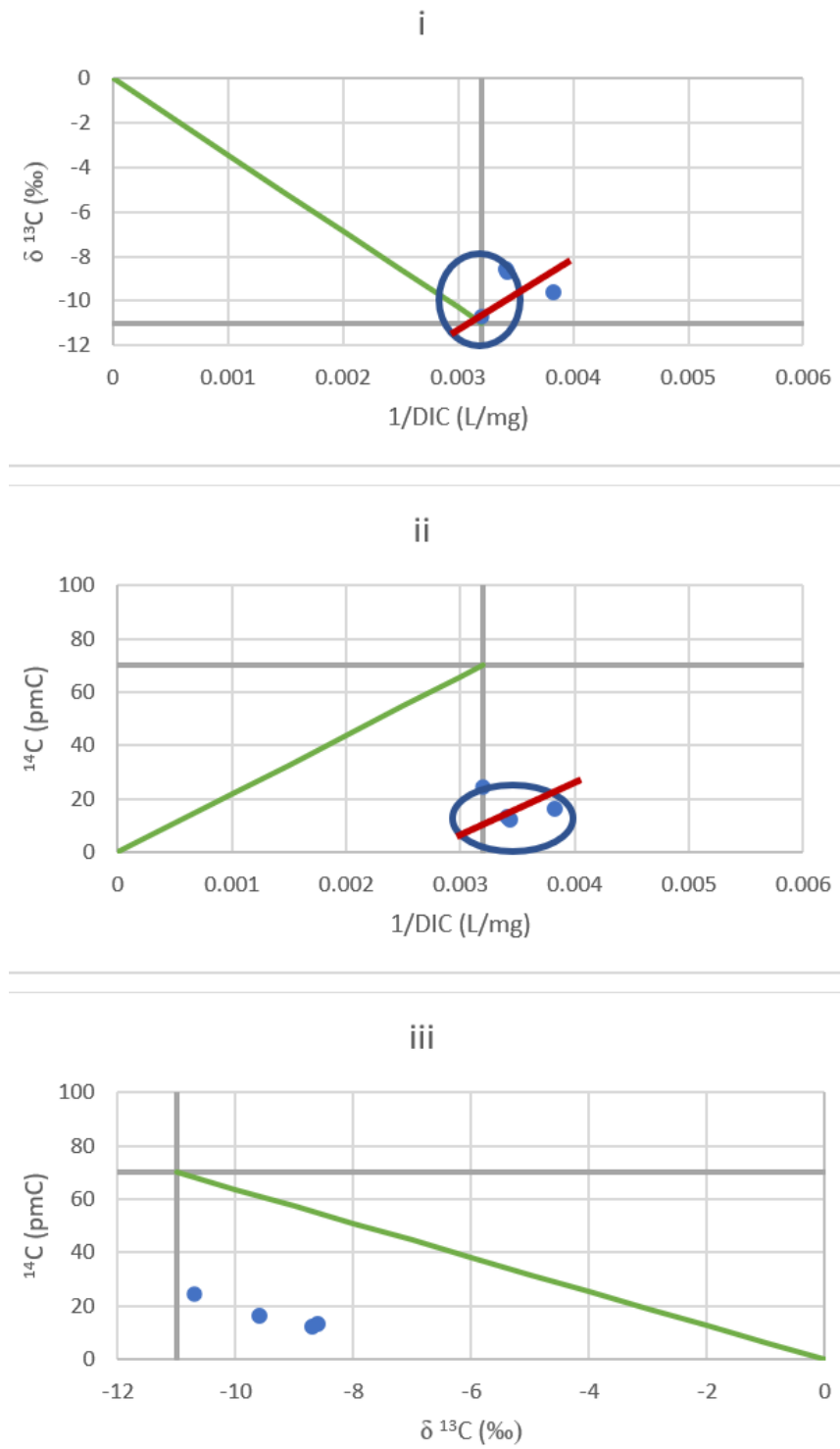


Figure 4.10: TX Capitan Reef carbon data plotted onto three carbon data interpretation graphs, to match Han et al., 2012 [2]; red trend lines designate dedolomitization trend; blue circles designate mixing of carbon sources

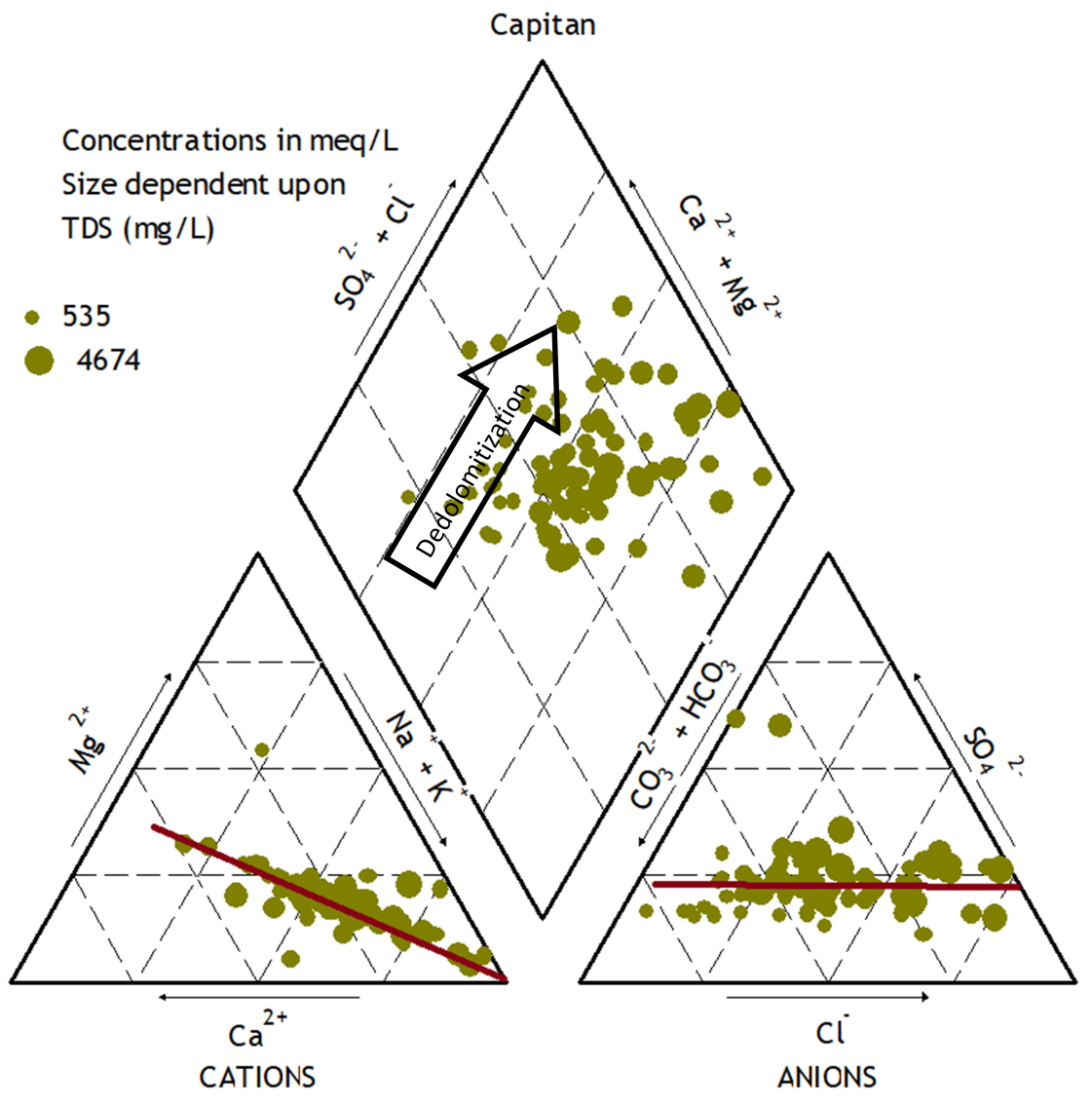


Figure 4.11: Piper diagram of chemistry points from Capitan Reef; size of the point is scaled by TDS concentration; arrow is indicative of dedolomitization; red lines suggest mixing with Salt Flats brine

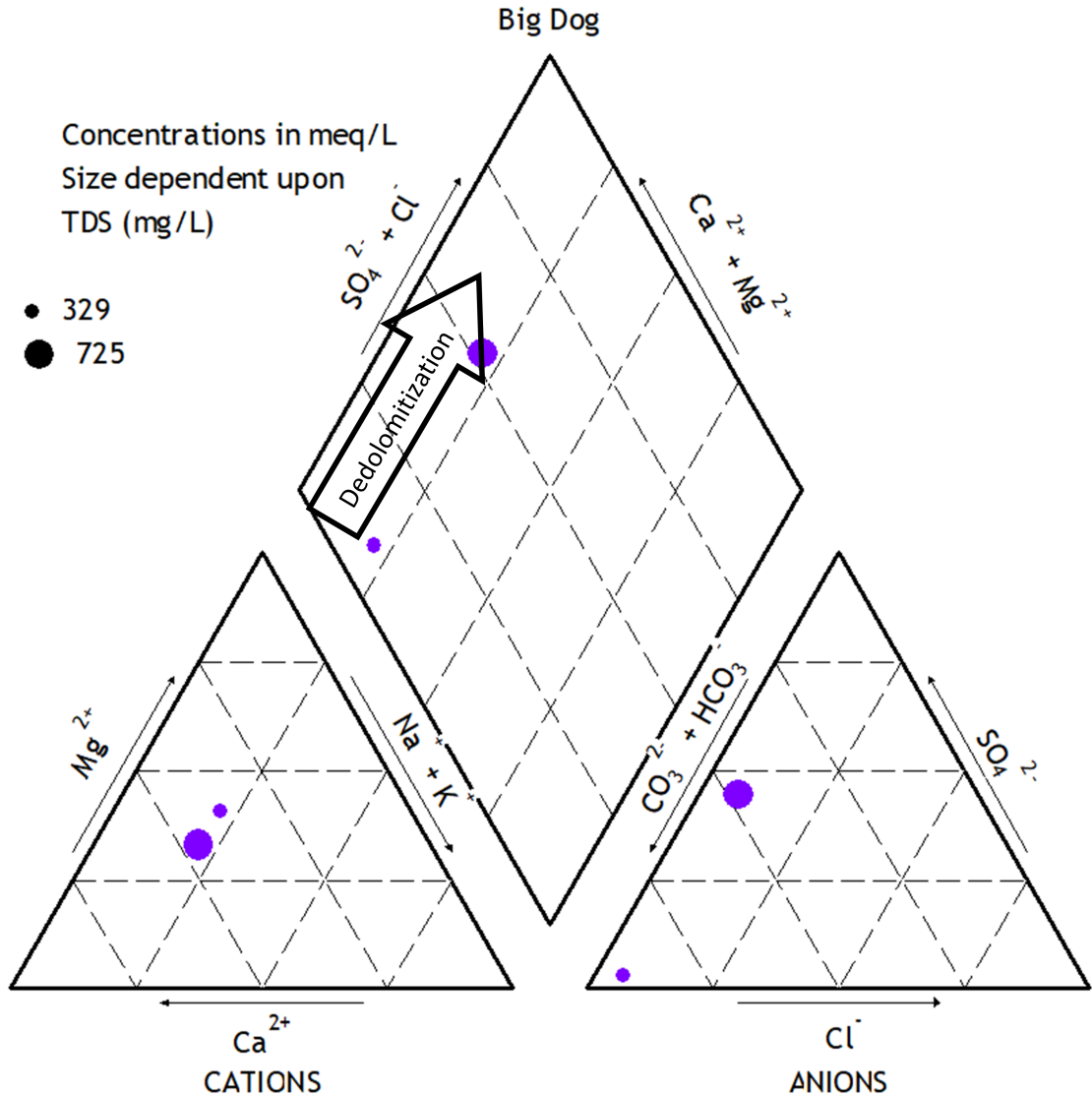


Figure 4.12: Piper diagram of chemistry points from Artesia Group; size of the point is scaled by TDS concentration; arrow is indicative of dedolomitization

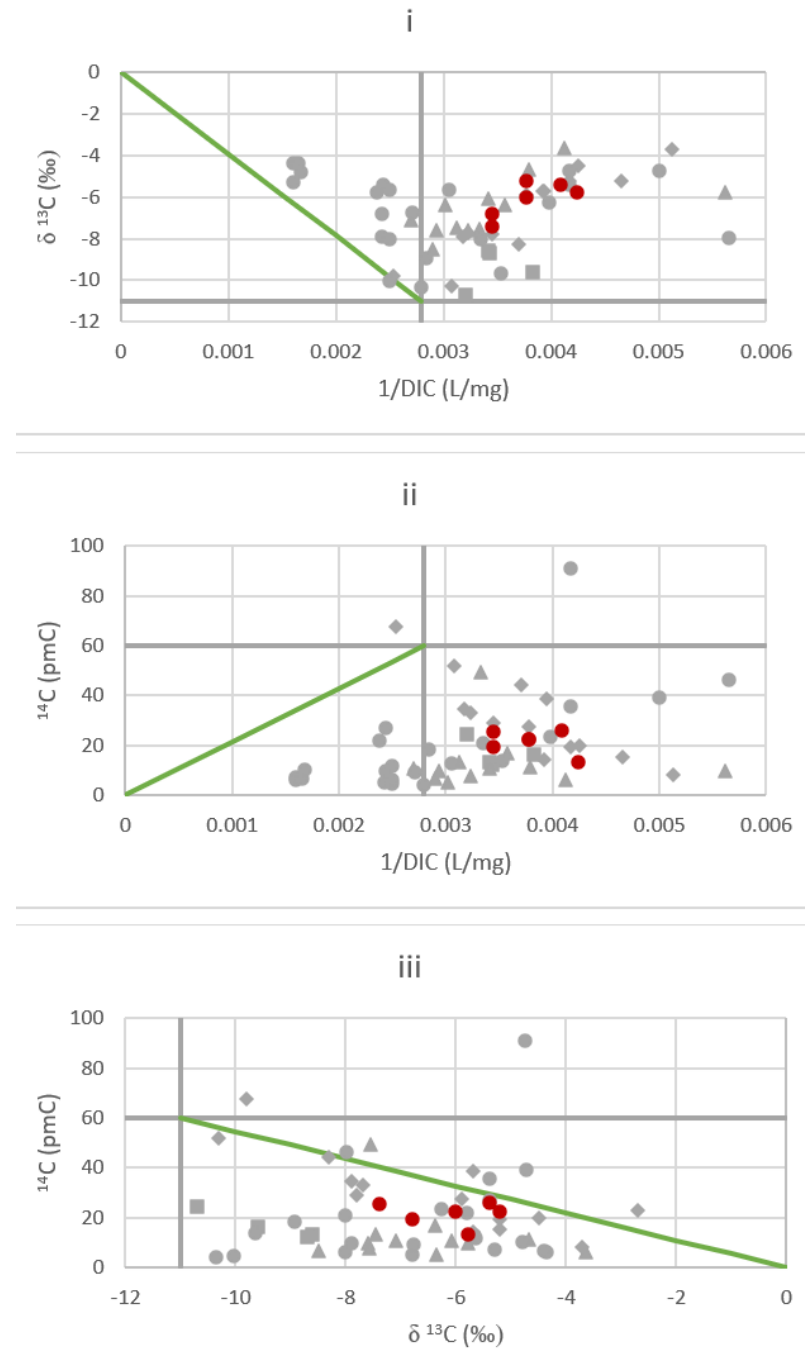


Figure 4.13: TX Salt Flats carbon data plotted onto three carbon data interpretation graphs, to match Han et al., 2012 [2]; red circles = Salt Flats, gray diamonds = Carbonates, gray circles = Cretaceous, gray triangles = Victorio Peak, gray squares = Capitan

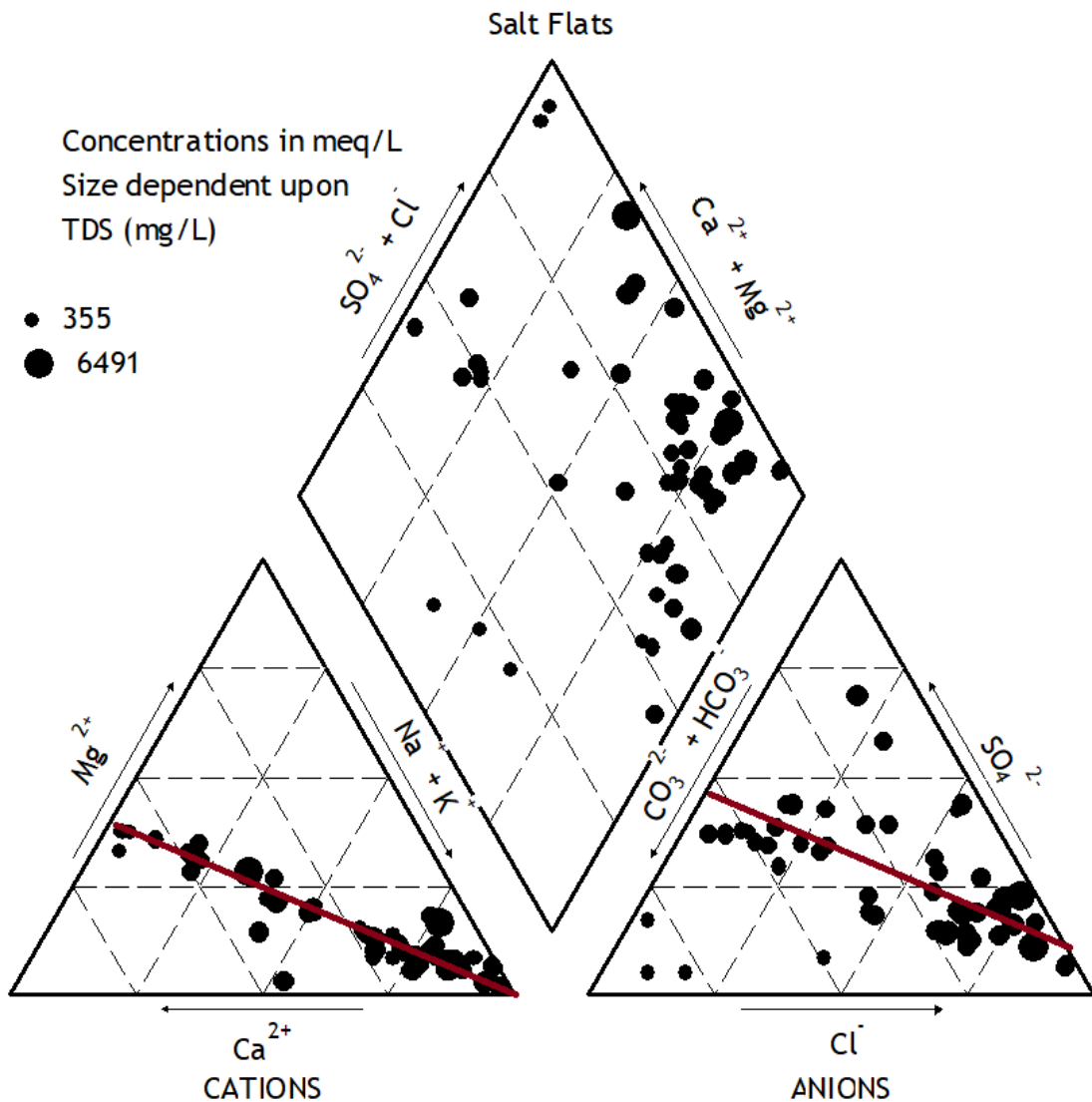


Figure 4.14: Piper diagram of chemistry points from Salt Flats; size of the point is scaled by TDS concentration; trend lines are indicative of mixing with halite from the playa surface

CHAPTER 5

WATER-BUDGET METHODS

5.1 NDVI Agricultural Evapotranspiration

Google Earth Engine (GEE) is a cloud-based platform that provides access geospatial databases and simplifies geospatial analyses using high-performance parallel computing [78]. This platform was utilized to estimate an effective pumping rate from the groundwater in agricultural areas, mostly around Dell City agricultural district. This water is pumped from the aquifer to irrigate agricultural fields, either by flood or pivot irrigation. Some amount of that irrigation water would then return to the groundwater [23, 40]. The net withdrawal amount of water that was pumped out, but did not return to the aquifer is the effective pumping amount. Before making the estimation, it was required to determine the surface area where agriculture was active. This active agricultural area can be identified from a normalized difference vegetation index (NDVI) map, where it contrasts strongly with the rest of the relatively barren Salt Basin.

The data catalog connected to GEE contains image collections from Landsat missions, dating back to 1972 [79]. Within the Landsat data catalog, the “Tier 1, 8-day NDVI composite” images from Landsat 5, 7, and 8 were colorized and used to visualize the NDVI for the Salt Basin over 35 years from 1984 to 2019. The beginning of the date range was established to align with the launch of Landsat 5 in March 1984 [80]. Landsat 5 data was utilized for analyses prior to 2012, when the satellite was nearing the end of its mission that officially terminated in January 2013. Landsat 7 was used to supplement Landsat 5 for 2012. However, Landsat 7 experienced a Scan Line Corrector (SLC) failure on May 31st, 2003 [81]. Hence, geospatial data from Landsat 7 was only used for 2012 before Landsat 8 was launched in February 2013. The remaining years from 2013 to 2019 used Landsat 8 data.

The image collections from Landsat 5, 7, and 8 were filtered to a specific date range from June 1st to August 31st of each year. This date range was selected as the “peak growing season” for agriculture within the Salt Basin based on visual inspection of monthly NDVI data (Figure 5.1, Figure 5.2, Figure 5.3) and the time between characteristic planting and harvesting dates for cotton and alfalfa in New Mexico [44]. These two crops are the most common agricultural product of Dell City [41, 44]. This date range is not fully representative of the full growing season of March to October, but rather represents the peak season from June to August

where it was assumed that agricultural greenness is maximized. Hence, Landsat images collected during this time range were filtered for the 85th percentile NDVI value to produce a singular active agricultural area for each year. This statistical approach reduced the noise from transient events, such as harvesting, cloudiness, or poor image quality, while maintaining the ability to detect differences between well-watered crops and weeds, desert vegetation, or poorly irrigated areas with little to no vegetation.

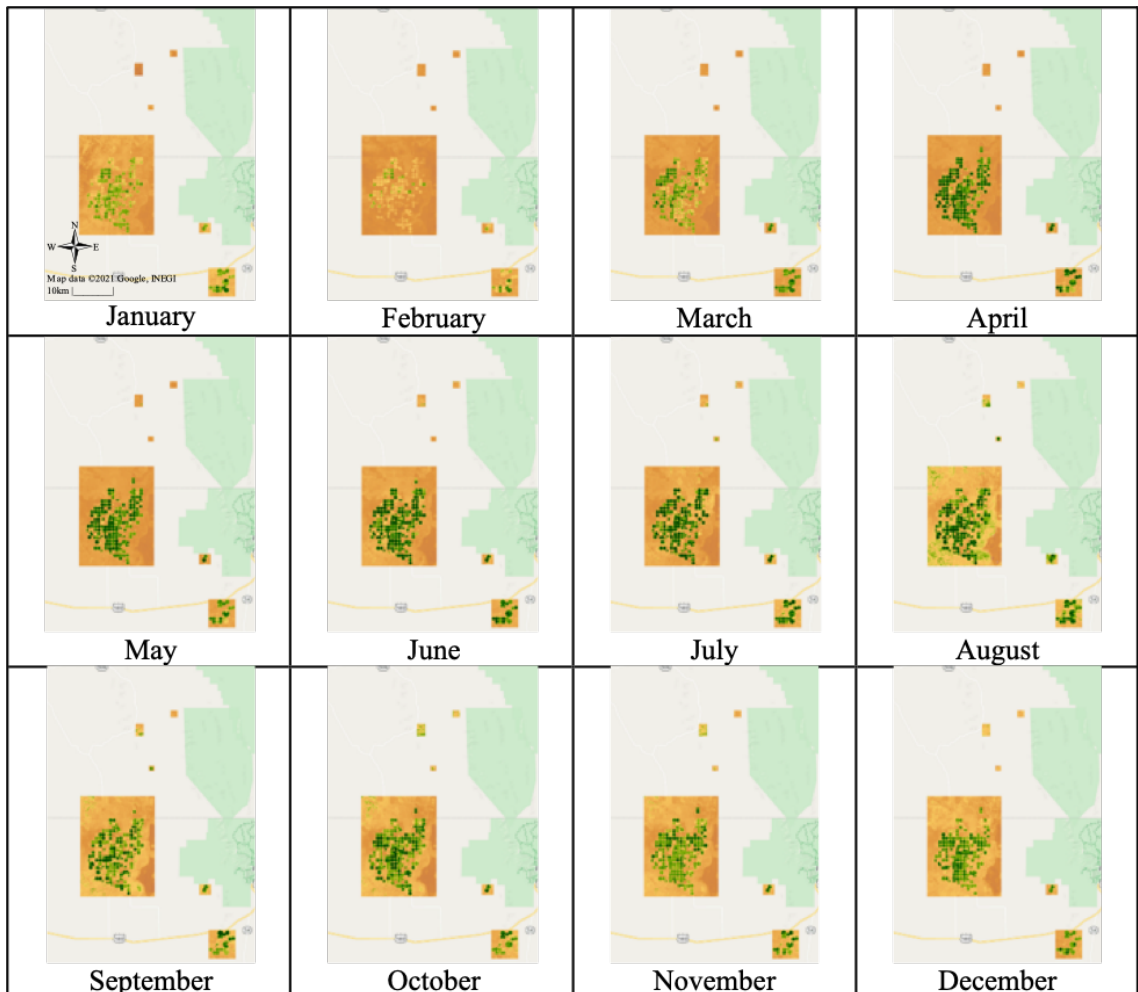


Figure 5.1: Monthly Google Earth Engine images of active agricultural greenness in the Dell City irrigation district and surrounding areas of the Salt Basin to show increase in greenness from March to October, with the peak greenness occurring between June and August; images are from 2017, which is considered a ‘wet’ year due to the large aerial extent of greenness; image data from Landsat 5, 7, and 8 and extracted using Appendix B.1 code

The NDVI image collection was reduced to show the top 85th percentile NDVI value at each pixel. If the pixel value exceeded a threshold that we set to 0.5, then

it was considered to be within the agricultural areas of the Salt Basin. Justification of this 85th percentile compared the resulting annual average active agricultural area to the active agricultural area values calculated by Groeneveld and Baugh (2002) [43]. Percentile values of 75 and 90 shifted the total area of active irrigation down or up, respectively, without changing the relative temporal pattern of the time series of annual irrigation acreage. The threshold of 0.5 was chosen to be equal to the NDVI of a manually selected green cell within the Salt Basin domain that was identified to be an active agricultural field with low-to-average greenness (Figure 5.4). Any greenness below this threshold was not included in the total annual active greenness. Below the percentile and threshold limit, greenness of the landscape could be attributed to natural flora that surround the agricultural fields, but use no irrigation. The only areas that were utilized for this geospatial analysis had visually identified active agriculture, such as pivot circles and unnatural, man-made rectangles of green. This reduced the possibility of including native flora greenness in the agricultural greenness calculations.

This process of reducing the NDVI Landsat 5, 7, and 8 image collections to a specific growing season date range, using a specific percentile to include, and over specified agricultural area produces an “active ag cells” JSON for each year in hectares. Refer to Appendix B.1 for an example year’s code to perform these refinements and produce an area where agriculture was likely being actively irrigated due to the level of NDVI greenness. In order to create an outline of whatever Google Earth Engine counted as an active agricultural cell, there is an additional piece of code that exports an image of the counted cells’ outline to the Google Drive. This outlining was used to visualize the active cells throughout the Dell City agricultural district, so it was only done every 4-6 years (1985, 1991, 1995, 2000, 2005, 2010, 2015, and 2019).

Once Google Earth Engine produced an area where there was active agriculture and thus active irrigation, the Blaney-Criddle method was used to calculate a reference crop evapotranspiration (ET_o) and then an effective irrigation pumping rate. This method was chosen because it is commonly used by New Mexico Office of the State Engineer (NMOSE) to estimate evapotranspiration [82]. The Blaney-Criddle is a theoretical method that requires a minimum and maximum monthly average temperature in Celsius. The equation for this method is given as

$$ET_o = p(0.46T_{mean} + 8) \quad (5.1)$$

with the reference crop evapotranspiration (ET_o) being a function of mean daily percentage of annual daytime hours (p) and the mean daily temperature (T_{mean}) in Celsius. The maximum and minimum temperature data, to calculate a mean daily temperature, was taken from a weather station in Dell City, TX with daily data for January 1, 1984 to December 31, 2019 [38]. The atmospheric water vapor pressure deficit, which is influenced by air temperature, influences a crop to shrink or expand its stomata in order to regulate internal water vapor. An increase in temperature results in stomatal closure to limit the amount of water the plant can lose to the atmosphere due to transpiration [83]. Further, a warmer air temperature will likely evaporate more water from the soil surface.

Within the Blaney-Criddle equation, there is also an estimated p-value from Table 5.1 [82]. This p-value represents the mean daily percentage of annual daytime hours for a given latitude during a given month. Sunlight throughout the day often correlates to warmer air temperatures and thus, an increase in evapotranspiration potential. Since the majority of the agricultural fields in the Salt Basin are located around Dell City, TX, the latitude of Dell City was used to choose monthly p-values for March through October (Latitude of 31.9387°N = p-value of 0.32, 0.31, 0.3, etc. 5.1). Together, the method estimates how much water is theoretically being lost to the atmosphere through evapotranspiration from the reference crop of grass/alfalfa and the surrounding soil based on the average temperature and amount of sunlight. This resulting reference ET_o is produced monthly, but was averaged over the eight months between March 1st and October 31st that are considered to be representative of the peak growing season.

Latitude	Jan	Feb	Mar	Apr	May	June	July	Aug	Sept	Oct	Nov	Dec
60°	0.15	0.2	0.26	0.32	0.38	0.41	0.4	0.34	0.28	0.22	0.17	0.13
55	0.17	0.21	0.26	0.32	0.36	0.39	0.38	0.33	0.28	0.23	0.18	0.16
50	0.19	0.23	0.27	0.31	0.34	0.36	0.35	0.32	0.28	0.24	0.2	0.18
45	0.2	0.23	0.27	0.3	0.34	0.35	0.34	0.32	0.28	0.24	0.21	0.2
40	0.22	0.24	0.27	0.3	0.32	0.34	0.33	0.31	0.28	0.25	0.22	0.21
35	0.23	0.25	0.27	0.29	0.31	0.32	0.32	0.3	0.28	0.25	0.23	0.22
30	0.24	0.25	0.27	0.29	0.31	0.32	0.31	0.3	0.28	0.26	0.24	0.23
25	0.24	0.26	0.27	0.29	0.3	0.31	0.31	0.29	0.28	0.26	0.25	0.24
20	0.25	0.26	0.27	0.28	0.29	0.3	0.3	0.29	0.28	0.26	0.25	0.25
15	0.26	0.26	0.27	0.28	0.29	0.29	0.29	0.28	0.28	0.27	0.26	0.25
10	0.26	0.27	0.27	0.28	0.28	0.29	0.29	0.28	0.28	0.27	0.26	0.26
5	0.27	0.27	0.27	0.28	0.28	0.28	0.28	0.28	0.28	0.27	0.27	0.27
0	0.27	0.27	0.27	0.27	0.27	0.27	0.27	0.27	0.27	0.27	0.27	0.27

Table 5.1: Blaney-Criddle mean daily percentage of annual daytime hours for different northern hemisphere latitudes; p-value for Blaney-Criddle equation [82]

While the Blaney-Criddle method is not dependent upon the NDVI, the two are connected in estimating a volume of evapotranspired water from the active agricultural fields in the Dell City agricultural district. The reference crop evapotranspiration rate was applied to the annual active agricultural surface area defined from GEE to estimate a volumetric rate of water leaving the system due to ET. That volumetric rate of ET was lastly multiplied by the number days in the growing season [March 1 to October 31 = 245 days] to produce a result of annual average volume evapotranspired in acre-feet per year during the months of March to October.

5.2 Chloride-Mass-Balance Approach

It is possible to create a groundwater recharge estimate based on chloride and bromide concentrations using the chloride-mass-balance method. Because chloride is non-reactive and stays in solution, chloride concentrations increase linearly as water is evaporated from a solution. Given an initial and final concentration, the fraction of water evaporated from the system (or alternative, the fraction of water remaining) can be calculated. With a large hydrochemical database, this method was useful to estimate an independent groundwater recharge rate for the Salt Basin. This method differentiates atmospheric chloride and chloride from mineral dissolution within the aquifer by effectively making a mixing model between a deep basin brine and fresh precipitation. Atmospheric chloride is deposited on the surface as wet deposition within precipitation and as dry deposition within dust [84]. The atmospheric deposition rate is dependent upon the atmospheric conditions, and consequently it varied from the Pleistocene to Holocene [85]. For the Holocene (less than 12,000 years ago), the steady-state atmospheric chloride deposition flux in precipitation in the study area is 0.55 mg/L [22].

The following chloride-mass-balance with bromide-correction methodology was modified from Rawling and Newton (2016) [22]. The bromide correction factor was utilized to mitigate the influence of chloride in the system due to mineral dissolution. Geologic chloride is associated with higher bromide concentrations than atmospheric chloride. The chloride mixing model creates a curve between two end members with corresponding chloride and bromide concentrations; one end member was freshwater/precipitation and the other end member was chloride brine. The freshwater end member has chloride concentrations of 0.55 mg/L, as determined by Rawling and Newton (2016) [22]. This was the lowest value of chloride that could be used to produce a usable curve with the Salt Basin data. Bromide concentration for the freshwater is 0.00846 mg/L. This value was calculated using the lowest Cl/Br ratio of 65 groundwater samples that was found within the Sacramento Mountains [22]. An unpublished report, referenced in Rawling and Newton (2016) [22] as "Street and Peery, 2007", found a brine in Cloudcroft, NM with very high chloride (130,000 mg/L) and bromide below the detection limit. The resulting chloride-to-bromide ratio would be higher than 1,000 (mg/L)/(mg/L). Though Cloudcroft, NM is not within the Salt Basin domain, it is within the Yeso formation within the Sacramento Mountains. These characteristics overlap into the Salt Basin. Hence, the Cloudcroft brine is considered representative of deep basin brines within the Yeso formation and within the Salt Basin. For the brine end member, the specific values were less important. Rather than having the measured brine as the end member, the chloride concentration was set to 10,000 mg/L, the Cl/Br ratio was set to be 9,000, and thus the bromide concentration was set to 1.1 mg/L [22].

$$Cl_{model} = [F - 0.00001](Cl_{freshwater}) + (1 - [F - 0.00001])(Cl_{brine}) \quad (5.2)$$

with a 0.00001 decrease with each consecutive proportion and 'F' equal to the prior result of the bracketed amount starting with F=1. This bracketed amount

represents the incremental decrease in the fraction of fresh water with respect to an equal increase in fraction of brine. The modeled concentrations of chloride and bromide use freshwater and brine concentrations of chloride and bromide. Figure 5.5 shows that resulting chloride-mass-balance mixing curve.

For the Salt Basin data, the chloride-to-bromide ratios were calculated and compared against the mixing curve to find the most likely chloride concentration from the modeled mixing between the freshwater and brine. This ‘most likely’ chloride concentration is designated as the ‘mixed’ chloride concentration and is representative of the total chloride concentration due to a modeled mixture of precipitation and brine that produces the measured chloride-to-bromide ratio. Consequently, the mixed chloride concentration includes the mixing ratio between fresh precipitation and brine waters. From this mixture chloride concentration, the corrected amount of atmospheric chloride was calculated using the following equation:

$$Cl_{corrected} = \frac{Cl_{measured}}{Cl_{brine}} \times 0.55mg/L \quad (5.3)$$

, where the 0.55 mg/L is the steady-state atmospheric chloride deposition flux in precipitation in the study area [22]. The corrected chloride concentration reflects the amount of atmospheric chloride in the groundwater sample with respect to the appropriate mixing ratio between fresh precipitation and brine water. All of this atmospheric chloride was deposited at the steady-state depositional rate and recharged to the groundwater with precipitation. Hence, the recharge amount as a fraction of total precipitation is equal to the steady-state depositional flux divided by the corrected chloride concentration. To ultimately get a recharge rate for the entire Salt Basin to compare to historic values, this fraction recharge amount was multiplied by total precipitation rates. The overall equation for the resulting recharge fraction from the chloride-mass-balance method is as follows:

$$Recharge\ fraction = \frac{0.55mg/L}{\left(\frac{Cl_{measured}}{Cl_{mixed}}\right) \times 0.55mg/L} \quad (5.4)$$

Rather than applying a singular average corrected recharge rate to the entire Salt Basin, recharge polygons were delineated using the HUC 10-digit watersheds and the spatial distribution of the corrected recharge rates. This separation resulted in two types of polygons: high, mountainous polygons and lowland polygons. The mountainous polygons used the total precipitation rate as potential recharge, altered by vegetation interception. This interception amount was applied only to the mountainous polygons and used code from Appendix B.1, which will be explained in further detail later. Simply, the code calculated a ratio of highly vegetated area versus total polygon area. This ratio became the interception ratio and was multiplied by the total precipitation to get a total precipitation amount reaching the surface. The precipitation amount that reached the surface was then multiplied by the fraction recharge to estimate total recharge rate for the mountainous polygons. For the lowland polygons, the total precipitation rate

was not useful, due to the semiarid nature of the Salt Basin. Therefore, the runoff values for each lowland polygon were calculated by PyRANA, which will be explained in further detail later. The runoff rates were multiplied by the fraction recharge rate to estimate total recharge rates for the lowland polygons. The total recharge rate from the chloride-mass-balance method is the sum of the recharge rates from each polygon.

5.3 Python Recharge Assessment for New Mexico Aquifers (PyRANA)

Groundwater recharge estimation independent from chemistry uses Python Recharge Assessment for New Mexico Aquifers (PyRANA). Originally called the Evapotranspiration and Recharge Model (ETRM), this distributed-parameter soil-water-balance model was developed at New Mexico Tech in 2016 by David Ketchum, Peter ReVelle, Esther Xu, Jake Ross, and Talon Newton [26–28, 86]. PyRANA quantifies recharge separately as diffuse recharge and focused recharge. Diffuse recharge is precipitation that infiltrates where it meets the ground surface and becomes recharge. In our study area, this diffuse recharge is found within high elevation areas, associated with the Ponderosa pine forests of the high Sacramento Mountains and Guadalupe Mountains. Focused recharge is the result of overland flow concentrating runoff into ephemeral channels in the lowlands, where it can then infiltrate through the channel bed or into a terminal playa. In both cases, water must infiltrate below the effective rooting depth of the surface vegetation, or the wicking depth of evaporation in bare ground, in order to be considered recharge. This fraction of runoff that becomes recharge is a modifier that is multiplied to the PyRANA results at the end.

PyRANA estimates evapotranspiration, runoff, and thus recharge based on multiple input parameters. For these calculations, PyRANA requires surface elevation/digital elevation model (DEM), Parameter-elevation on Independent Slopes Model (PRISM) precipitation, climate data, Gridded Atmospheric Data Downscaling Evapotranspiration Tools (GADGET), vegetation coverage/normalized difference vegetation index (NDVI) from Moderate Resolution Imaging Spectroradiometer (MODIS), soil characteristics from Natural Resources Conservation Service (NRCS), rooting depth, and root capture efficiency, as well as additional parameters defined in Ketchum (2016) [26]. The rooting depth and root capture efficiency are set based on the type of vegetation and characteristic soil thickness within the diffuse recharge areas. The vegetation cover within the Salt Basin was divided into 9 categories with corresponding rooting depths: 1) bare, 2) shrub, 3) grasses, 4) Piñon-Juniper, 5) Ponderosa pine and mixed conifer, 6) mountain grasses/meadow, 7) Riparian wetlands, 8) prairie, 9) Creosote. Within these variables, PyRANA applies modification factors that limit winter evaporation and corrects for monsoonal precipitation [26–28, 86]. A water stress coefficient comes from Allen et al.(2011) [87].

In order to calculate evapotranspiration from the input parameters, PyRANA utilizes a modified version of Food and Agriculture Organization's

(FAO) Penman-Monteith equation from Allen et al. (2011) [26–28, 86, 87]. This methodology uses a dual crop coefficient, soil-water-balance, and energy balance in order to quantify the net effect of the input variables and ascertain the amount of recharge in the system. As a qualitative output, PyRANA produces spatial distribution maps of vegetation, diffuse recharge areas, and channels of probable focused recharge. Runoff in the Salt Basin is calculated by PyRANA using a non-linear regression relationship established by Xu (2018) [27]. This relationship is between daily precipitation rates and runoff measured in Walnut Gulch, Arizona. For every intensity of precipitation, there is a different amount of runoff estimated that changes non-linearly. Walnut Gulch has comparable climate and vegetation to the Salt Basin and is well monitored [27]. With the similar climate, Walnut Gulch also experiences monsoons. Hence, the monsoonal season has a different regression than that for the winter months.

As denoted by the name, PyRANA was developed for New Mexico aquifers. The original inputs for PyRANA were limited to New Mexico. Because the model physics of PyRANA are universal, the model outputs were extended southwards to cover the Texas portion of the Salt Basin using a linear regression using the lowlands of the New Mexico Salt Basin as a reference. Using R statistical software [88], the PRISM gridded annual average precipitation produce and elevation data from the USGS were used as predictors from the PyRANA derived average annual runoff gridded output. Once the model was fit using runoff estimates from New Mexico, an annual runoff grid for the Texas portion of the basin was produced. Diffuse recharge was not well predicted by PRISM precipitation and elevation, so no regression estimate of diffuse recharge was produced for Texas. However, given that diffuse recharge was only predicted by PyRANA in the Ponderosa pine portion of the northern Salt Basin, we are confident that the model would not have predicted any diffuse recharge in the creosote and grass dominated southern portion of the basin. The input datasets for PyRANA have not been processed for the Texas portion of the study area, so model outputs are limited to the New Mexico side. Within areas of the New Mexico Salt Basin where laterally flowing groundwater serves as an additional source of soil moisture (i.e., salt playas), PyRANA has difficulty estimating the amount of evaporation for the surface because it is a one-dimensional (i.e., vertical) model. PyRANA input data have only been processes for the period January 1, 2000 to December 31, 2013, limiting results reported here to an average of the years 2002-2013. The first two years, 2000-2001, are considered unreliable due to the need to spin up the model to balance soil moisture storage values. PyRANA has further potential for uncertainty since runoff is estimated based on a precipitation intensity and duration regression calibrated using data from Walnut Gulch, AZ [27, 28].

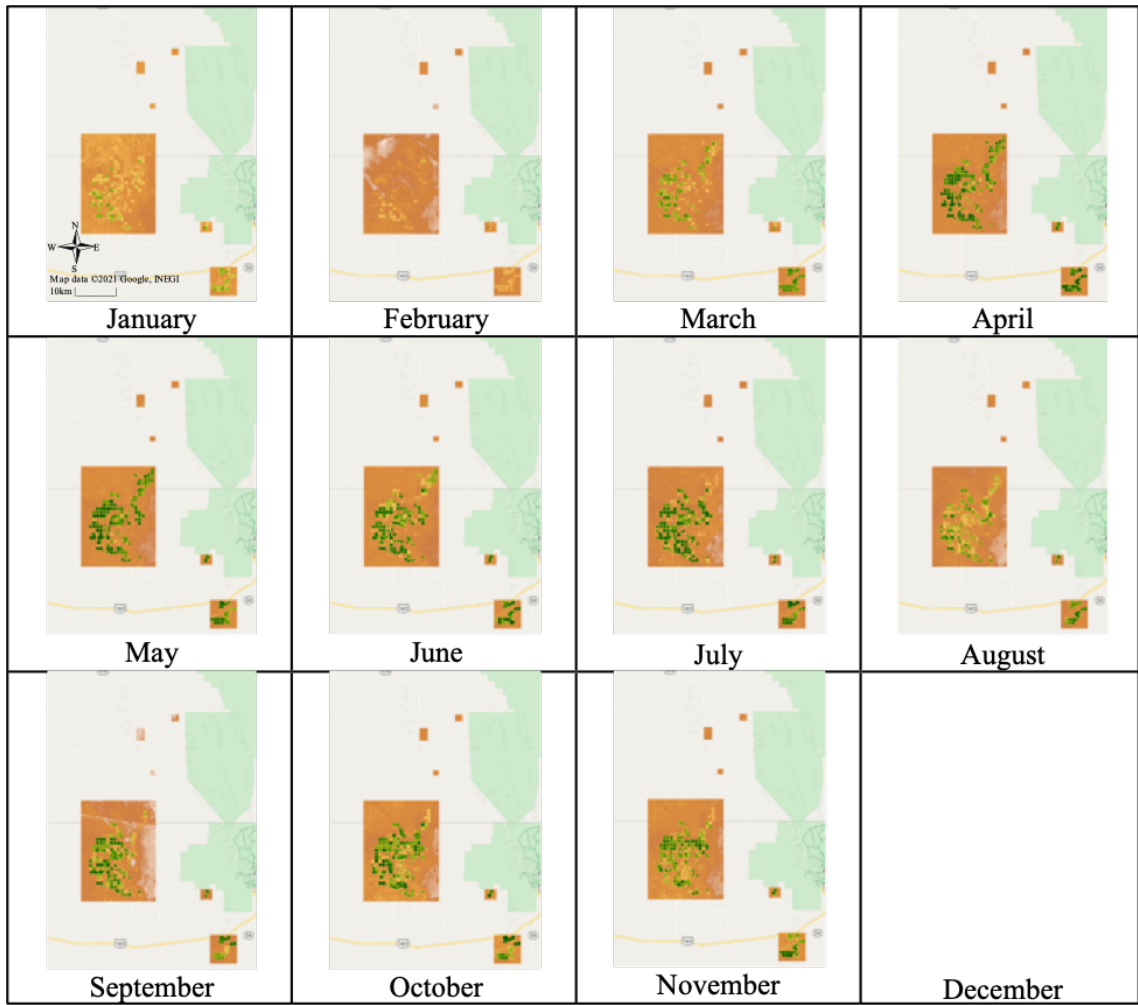


Figure 5.2: Monthly Google Earth Engine images of active agricultural greenness in the Dell City irrigation district and surrounding areas of the Salt Basin to show increase in greenness from March to October, with the peak greenness occurring between June and August; images are from 2011, which is considered an 'intermediate' year due to the average aerial extent of greenness; image data from Landsat 5, 7, and 8 and extracted using Appendix B.1 code; December data is omitted due to poor image quality

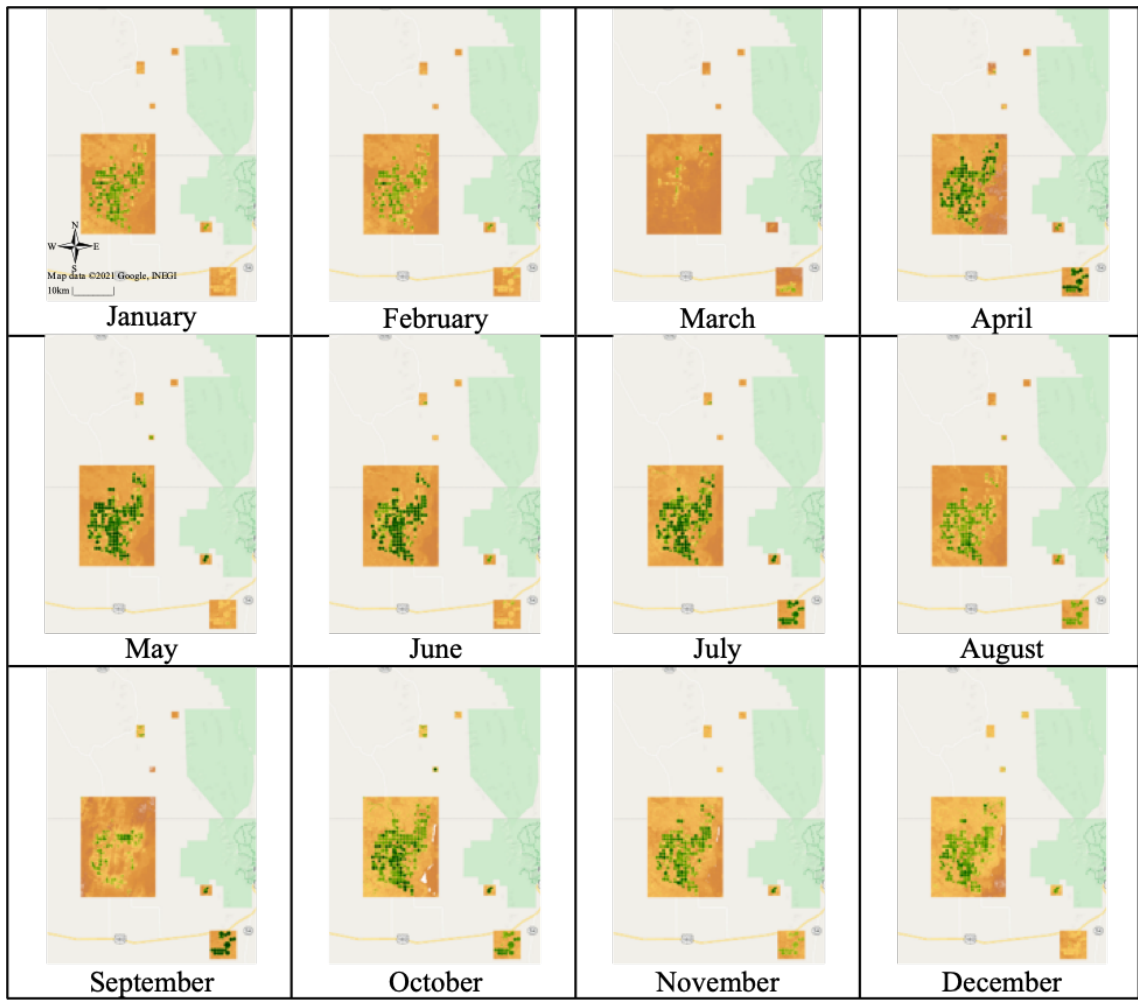


Figure 5.3: Monthly Google Earth Engine images of active agricultural greenness in the Dell City irrigation district and surrounding areas of the Salt Basin to show increase in greenness from March to October, with the peak greenness occurring between June and August; images are from 2019, which is considered a 'dry' year due to the small aerial extent of greenness; image data from Landsat 5, 7, and 8 and extracted using Appendix B.1 code



Figure 5.4: Google Earth Engine average active agricultural greenness threshold set to 0.5, based on greenness of highlighted cell within Dell City irrigation district; image from 2016; image data from Landsat 5, 7, and 8 and extracted using Appendix B.1 code

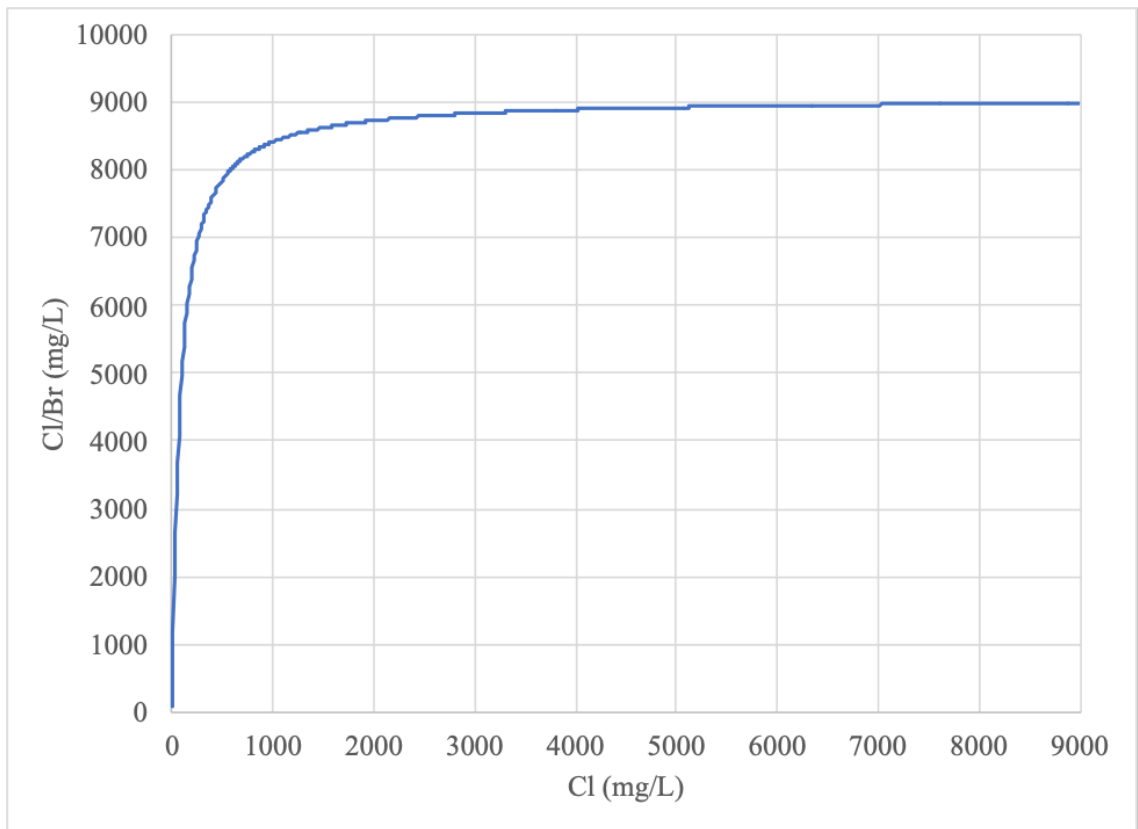


Figure 5.5: Modeled chloride mixing curve showing ratio of chloride to bromide versus concentration of chloride, made using chloride-mass-balance mixing equation and explanation from [22]

CHAPTER 6

WATER-BUDGET RESULTS

6.1 Blaney-Criddle Consumptive Use

Using daily temperature maximum and minimum for Dell City, TX, the average maximum and minimum were calculated, and from those values, the mean temperature for each month was calculated (Appendix C.1). Using the Blaney-Criddle approach equation and the respective p value for each month from Table 5.1, the monthly reference evapotranspiration values were calculated. Google Earth Engine was used to define annual active agricultural cells throughout the Salt Basin. Figure 6.1 shows an example of this active agricultural aerial extent that contributes water lose due to evapotranspiration, as specified by Google Earth Engine and specified greenness thresholds. The result of this analysis was an annual consumptive use rate of water for the irrigation district with active agriculture around Dell City, TX. Table 6.1 has these final consumptive use measurements, using values provided in Appendix C.1. The maximum annual consumptive use for Dell City was 95,758 acre-feet per year in 2014. The minimum annual consumptive use was 26,722 acre-feet per year in 1990. There is a general temporal trend of increasing consumptive use nearing modern, as shown in Figure 6.2.

6.2 Chloride-Mass-Balance

The chloride-mass-balance method used 139 groundwater well samples that contained chloride and bromide. Figure 6.3 presents the Salt Basin data points with respect to the chloride mixing model curve. Since the measured points are under the curve, the mixing model is applicable to the Salt Basin. Figure 6.4 shows the spatial distribution of the samples, as well as the corrected chloride recharge fractions. Plotting the corrected against the uncorrected recharge fractions for each polygon, it is evident that the chloride-mass-balance corrections affect the waters that originated from the Sacramento Mountains the most: Piñon Creek, Sacramento River, and Sacramento Mountains (Figure 6.5). These polygons with Sacramento Mountain groundwater change a maximum of 0.3 (30%), moving from 0.07 (7%) to 0.37 (37%). The remainder of the Salt Basin chloride points change a maximum of 0.07 (7%), moving from 0.01 (1%) to 0.08 (8%). Additionally, assuming

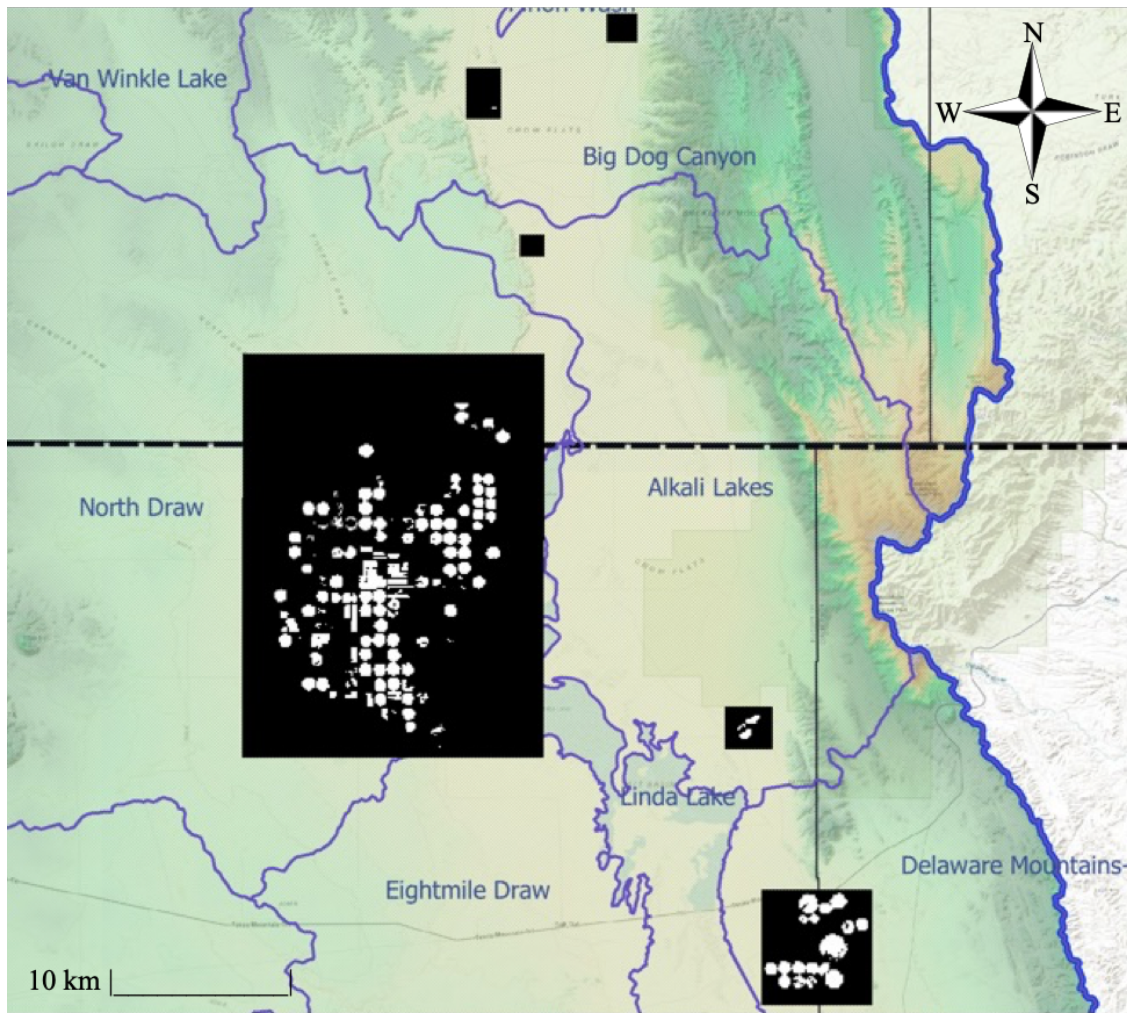


Figure 6.1: Aerial extent of active agricultural greenness from Google Earth Engine for 2019 is highlighted in white; black background designates area where there was potential for agricultural greenness

the majority of recharge occurs in the Sacramento Mountains, the chloride mixing curve corrections are justified for the Salt Basin chloride data points.

Using this distribution, the Salt Basin was separated into 8 recharge polygons. The polygons were primarily based on the HUC 10-digit watersheds of the Salt Basin, and were modified to group similar initial recharge values, as well as grouping watersheds within the same general groundwater flow path according to observed hydraulic head (Figure 1.8). Two additional polygons were established to align with mountainous diffuse recharge areas from PyRANA, which will be discussed in further detail later. An average corrected recharge fraction over the aerial extent of each polygon was then calculated. This average corrected recharge value represents the proportion of average precipitation that becomes recharge

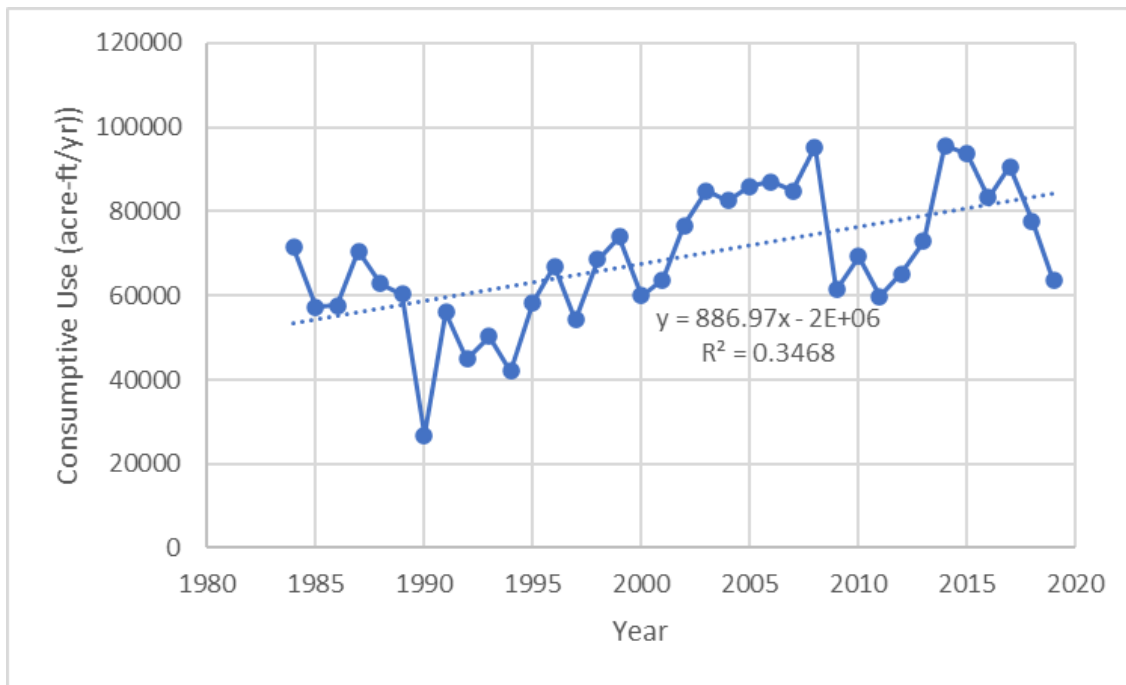


Figure 6.2: Annual Consumptive Use from Blaney-Criddle for Dell City irrigation district; consumptive use in acre-feet per year; data from Table 6.1; equation and R squared value for trend line provided

and was calculated by averaging all of the corrected recharge values within each polygon (Table 6.2). For the polygons around the Sacramento Mountains and Guadalupe Mountains, all of the annual precipitation was considered as the source water for potential recharge. For the other 6 polygons spread throughout the lowlands of the Salt Basin, only the runoff amount from PyRANA was considered as the potential recharge source. This stipulation was added to reflect the semiarid nature of the lowland basin where the majority of precipitation was evaporated or transpired from the soil, leaving an accumulation of chloride in the root zone. Our conceptual model of these areas only includes focused recharge along ephemeral channels, so the source water that should be considered was only the runoff that accumulates there in flow events. Focused recharge in the lowlands creates an irregular pattern in the groundwater isotopes by mixing locally-sourced water with water that followed a longer flow path from the headwaters. Since Figure 3.7 shows this irregular pattern of $\delta^{18}\text{O}$, there is likely focused recharge occurring in the lowlands. Table 6.2 provides the areas, runoff amount (or total precipitation for mountain polygons), average corrected recharge, and recharge volume for the recharge polygons shown in Figure 6.4.

For the lowland polygons, the corrected recharge rates from the chloride-mass-balance method ranged from 169 acre-feet per year (for Shiloh Draw) to 2,338 acre-feet per year (for Piñon Creek). These recharge amounts were overshadowed

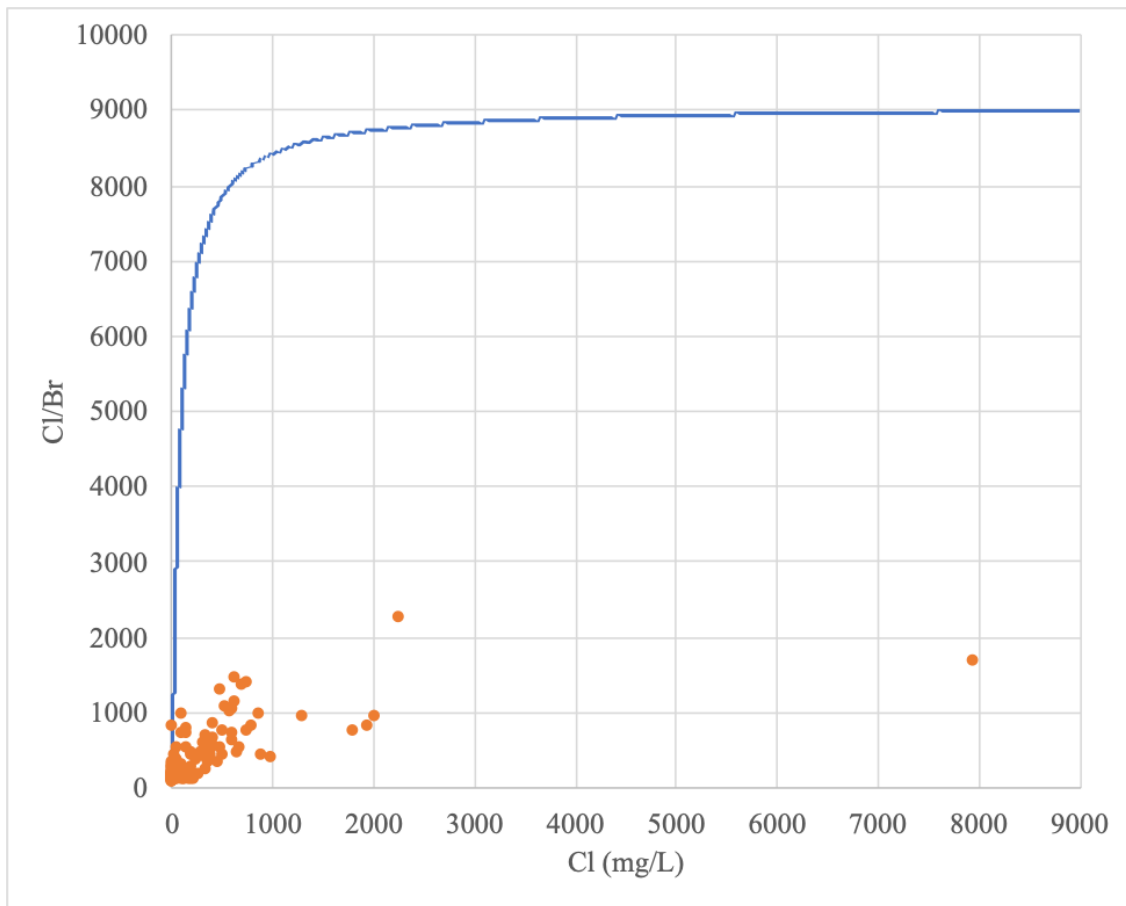


Figure 6.3: Salt Basin chloride and bromide data points against modeled chloride mixing curve showing ratio of chloride to bromide versus concentration of chloride, made using the chloride-mass-balance mixing equation and explanation from [22]; data concentrations from Appendix A.1

by the recharge rates from the Sacramento Mountains of 22,078 acre-feet per year and the Guadalupe Mountains of 4,628 acre-feet per year. The cumulative recharge rate for the chloride-mass-balance method is 31,562 acre-feet per year.

6.3 PyRANA Runoff Recharge

PyRANA calculates the diffused and focused recharge separately, due to the differences in the processes. Diffuse recharge in the Salt Basin is isolated to the high elevations of the Sacramento Mountains (Figure 6.6). This figure shows PyRANA estimating diffuse recharge for the Salt Flats. Due to the evaporative nature of the Salt Flats, there is likely no diffuse recharge occurring in this area. Hence, areas of diffuse recharge outside of the northern Salt Basin are considered

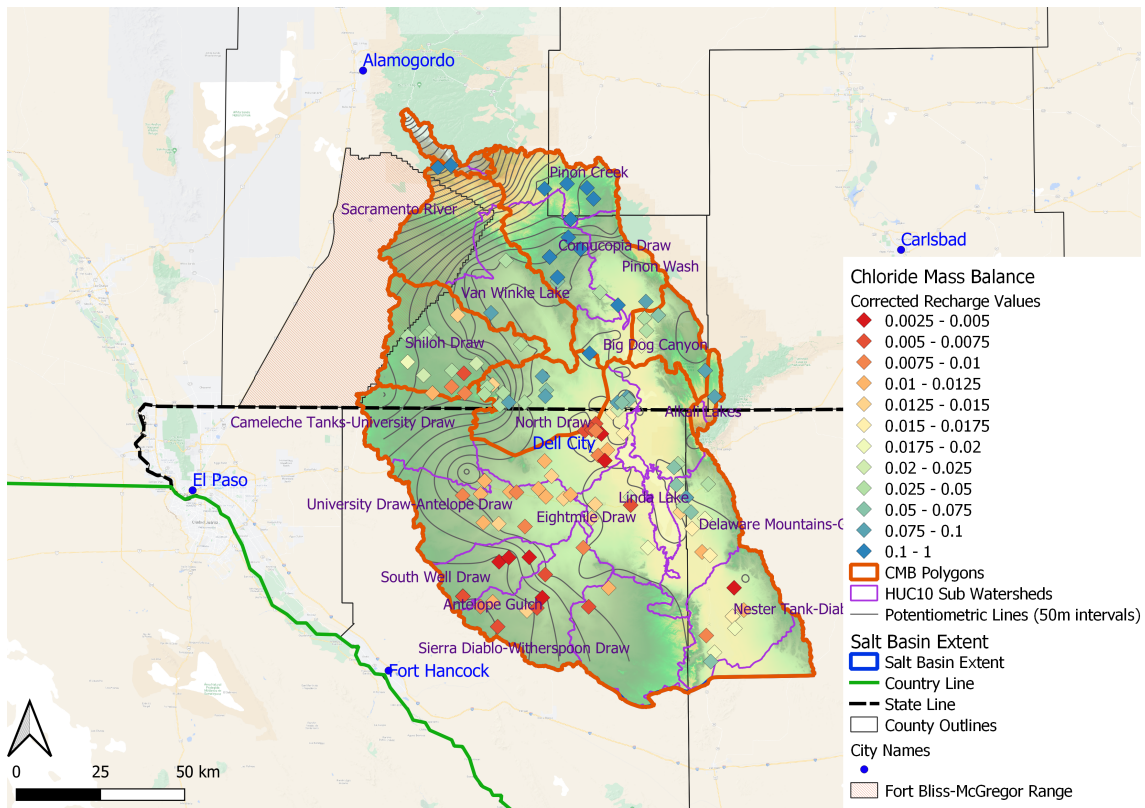


Figure 6.4: Salt Basin data points with chloride and bromide concentrations, denoted by corrected chloride recharge value; color-scaled to uncorrected chloride recharge value (lower uncorrected values are in red); chloride-mass-balance polygons outlined in orange

erroneous. In contrast to diffuse recharge, focused recharge occurs mostly in the foothills and lowlands of the basin. The focused recharge happens primarily along ephemeral flow channels where there is runoff. While this type of runoff is more common in the lowlands, it can also happen in the high elevation mountains. The total recharge estimate from PyRANA includes diffuse recharge in the Sacramento Mountains and focused recharge from mountainous runoff. Focused recharge in the lowlands was calculated as the amount of runoff times the average recharge fraction for each polygon from the chloride-mass-balance method. Hence, there is no independent PyRANA recharge estimate for the lowland polygons. Table 6.3 summarizes the recharge values from PyRANA for the mountainous polygons that includes diffuse and focused recharge from the mountains.

The largest contributor of mountainous recharge from PyRANA is the Sacramento Mountains (5,407 acre-feet per year). Guadalupe Mountains diffuse recharge was the smallest contributor, adding 2,478 acre-feet per year. PyRANA estimated a total recharge from diffuse recharge alone to be 7,885 acre-feet per year. When adding in the lowland polygons recharge from the chloride-mass-balance

method, that used PyRANA runoff amounts, the total recharge from the PyRANA method is 13,000 acre-feet per year.

Year	Annual Average ET_o (m/day)	Annual Average Agriculture	Volume Average Active for m^2	Volume ET-ed (m^3 /day)	Annual ET-ed (acre- feet/day)	Consumptive Use (acre- feet/year)
1984	0.0051	7006	70060000	360050.95	292.01	71543
1985	0.0051	5622	56220000	288063.96	233.63	57239
1986	0.0051	5693	56930000	289976.82	235.18	57619
1987	0.0051	6937	69370000	355272.98	288.14	70594
1988	0.0051	6221.784	62217843	316473.08	256.67	62884
1989	0.0053	5682.922	56829216	303806.06	246.4	60367
1990	0.0052	2584	25840000	134484.6	109.07	26722
1991	0.0051	5518	55180000	281650.55	228.43	55965
1992	0.0052	4315	43150000	225841.92	183.16	44875
1993	0.0053	4806	48060000	253070.51	205.25	50286
1994	0.0054	3930	39300000	211695.63	171.69	42064
1995	0.0053	5555.247	55552471	293347.35	237.91	58289
1996	0.0052	6447.639	64476392	336884.79	273.22	66940
1997	0.0053	5170	51700000	272811.39	221.26	54208
1998	0.0053	6477	64770000	345403.26	280.13	68632
1999	0.0053	7056.275	70562745	372055.99	301.75	73928
2000	0.0054	5573	55730000	302319.13	245.19	60072
2001	0.0054	5969	59690000	320484.71	259.92	63681
2002	0.0054	7085.435	70854353	386092.69	313.13	76718
2003	0.0054	7957	79570000	427654.14	346.84	84976
2004	0.0053	7854.004	78540039	415692.29	337.14	82599
2005	0.0052	8267	82670000	433149.83	351.3	86068
2006	0.0053	8274.639	82746392	437954.36	355.19	87023
2007	0.0053	8086	80860000	427176.27	346.45	84881
2008	0.0052	9199.169	91991686	479599.66	388.97	95298
2009	0.0054	5708	57080000	309342.96	250.89	61467
2010	0.0054	6433.455	64334549	348681	282.79	69284
2011	0.0054	5537	55370000	300998.63	244.12	59809
2012	0.0054	6032	60320000	328021.1	266.03	65179
2013	0.0053	6918	69180000	367125.51	297.75	72949
2014	0.0053	9064.078	90640784	481916.17	390.85	95758
2015	0.0053	8858	88580000	471817.32	382.66	93751
2016	0.0052	8041	80410000	419653.68	340.35	83386
2017	0.0052	8722	87220000	456017.31	369.84	90612
2018	0.0053	7319	73190000	391515.31	317.53	77795
2019	0.0052	6128	61280000	319799.53	259.37	63545

Table 6.1: Resulting annual consumptive use from Dell City irrigation district based on an annual average ET_o from Blaney-Criddle and annual average active greenness hectares from Google Earth Engine using Appendix B.1 code; annual average ET_o for March to October; annual average active greenness hectares for June to August; volume ET-ed is the volume evapotranspired from March to October

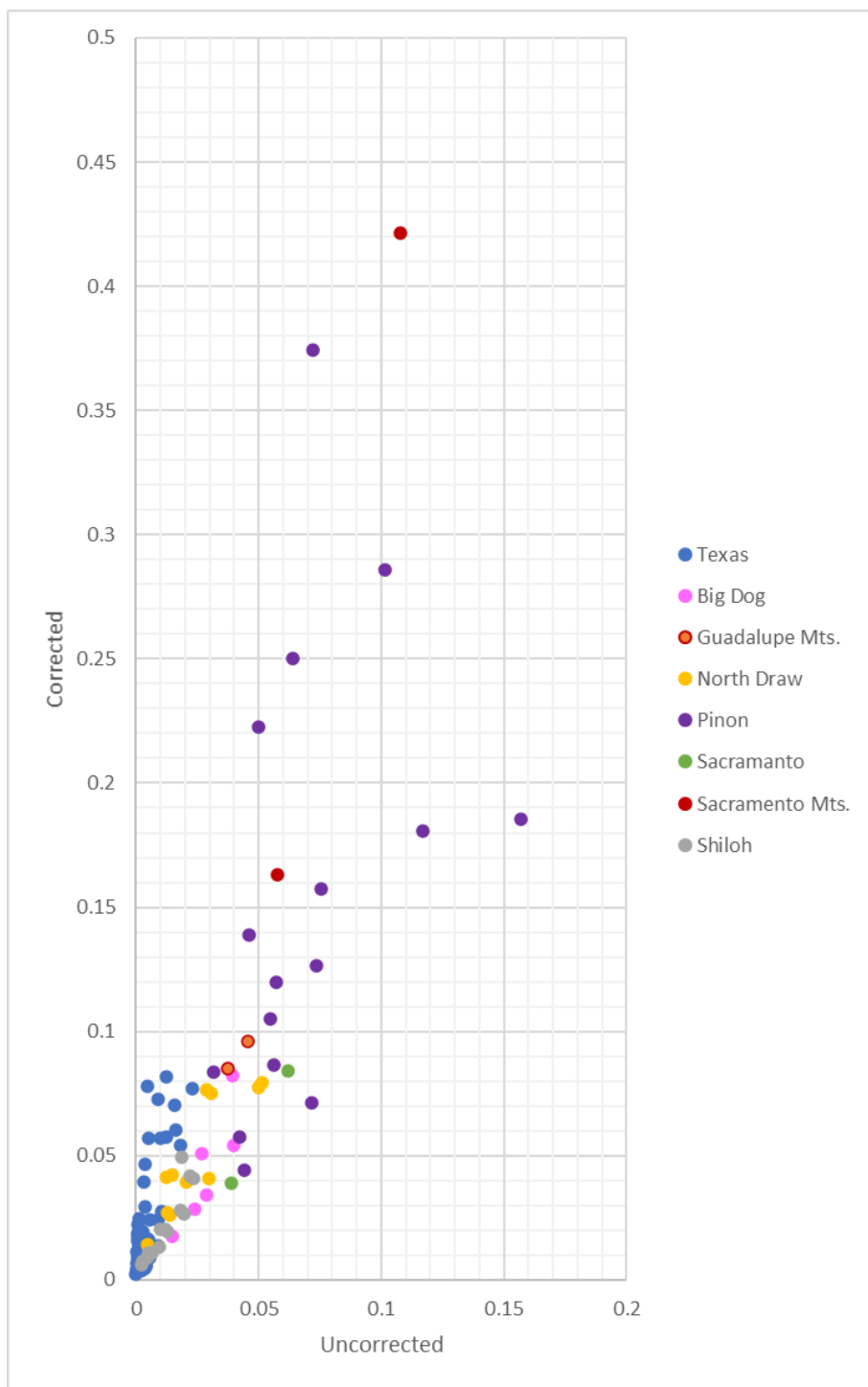


Figure 6.5: Chloride-mass-balance recharge fractions: corrected versus uncorrected to compare significance of correction; points color-coded by CMB polygon

Watershed	Area (m^2)	Area (acres)	Runoff or (acre-ft/yr) or *Total Precip. (acre-ft/yr)	Average corrected recharge value	Recharge Volume (acre-ft/yr)
North Draw	885254542.4	218743.4	4791.56	0.05	235
Piñon Creek	1834422459	453279.58	11678.33	0.2	2338
Sacramento River	1554425795	384093.35	11039.57	0.1	1054
Big Dog Canyon	431356974.2	106586.85	3825.78	0.05	193
Shiloh Draw	1012122889	250092.14	7746.71	0.02	169
Texas	7879196278	1946922.73	46572.14	0.02	867
				Lowland CMB +PyRANA Total	4856
Sacramento Mountains	160332313	39617.57	*76132.57	0.29	22078
Guadalupe Mountains	117850264	29120.4	*48294.62	0.1	4628
				Mountainous Total	26706
				Total	31562

Table 6.2: Resulting recharge volumes from chloride-mass-balance for polygons in Figure 6.4; for Sacramento Mountains and Guadalupe Mountains, total precipitation (acre-feet/year) was used instead of PyRANA runoff, as designated by the asterisk

Watershed	Diffuse Recharge	Mountain Focused recharge	Total recharge from each area
Sacramento Mountains	3194	2213	5407
Guadalupe Mountains		2478	2478
		Mountainous PyRANA Total	7885
		Lowland CMB/PyRANA Total	4856
		Total PyRANA	12741

Table 6.3: Resulting mountainous recharge amounts from PyRANA with diffuse recharge and focused recharge; all values are in acre-feet/year

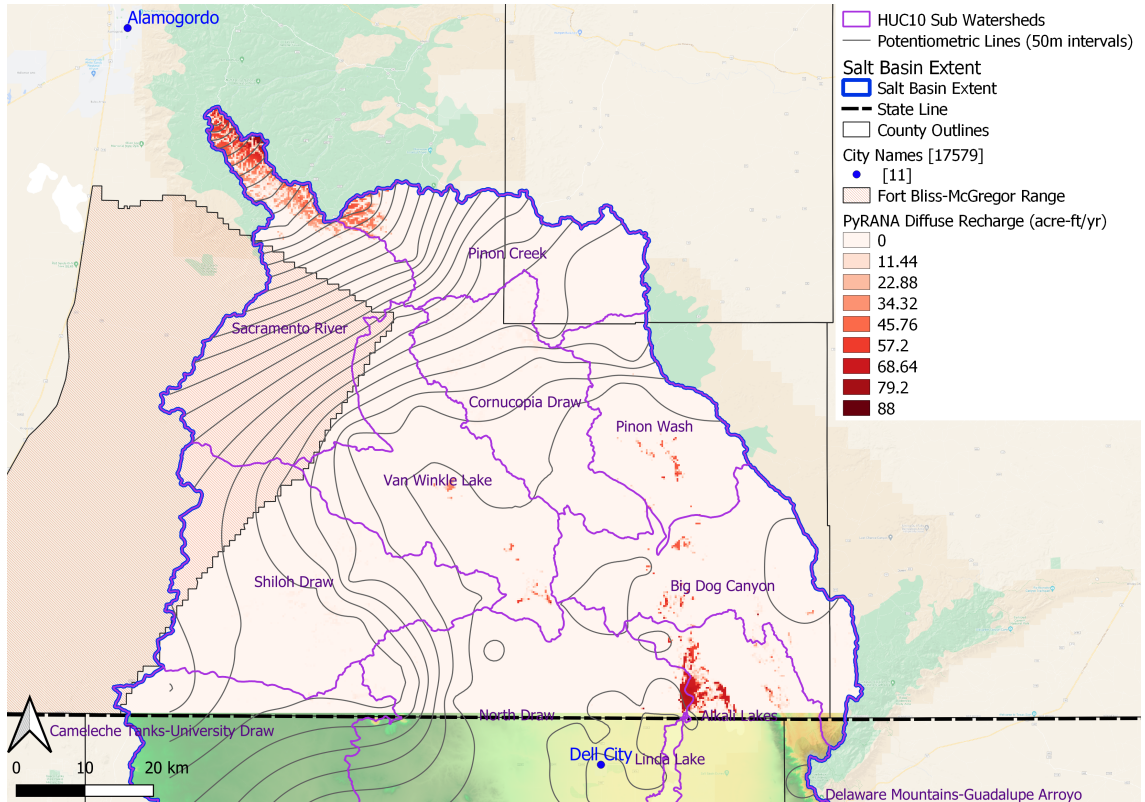


Figure 6.6: Aerial extent of diffuse recharge in the Salt Basin, focused within the high elevations of the Sacramento Mountains; diffuse recharge denoted outside of the northern Salt Basin are considered erroneous measurements from PyRANA

CHAPTER 7

WATER-BUDGET DISCUSSION

7.1 Water-Budget Assessment

The basin-wide water balance includes discharge (i.e., ET) and recharge. The Blaney-Criddle method produced an isolated measurement of discharge from the Dell City irrigation district and surrounding agricultural areas. This method contains inherent uncertainty, specifically due to the empirically defined p-value and the nearly exclusive reliance upon temperature data. In the future, the evapotranspiration from Salt Basin agriculture could be improved to further improve the overall water-budget, for example by using more advanced remote-sensing-based estimates of ET. This consumptive use output was not further used in this analysis, but it is important to note the amount of water leaving the Salt Basin hydrological system through this agriculture. In order to sustain the aquifer, this consumptive use, combined with any trans-basin extractions through pipelines, must remain below the recharge rate. For a further analysis of this sustainability and potential pumping well expansions, refer to Evenocheck (2021) [1].

The chloride-mass-balance method produced a recharge estimate for each polygon subsection of the Salt Basin. The distribution of corrected recharge fractions across the Salt Basin suggests relative volumes of recharge from each polygon. Higher recharge fractions along the northern margin of the Salt Basin suggests a large volume of recharge originating from the Sacramento Mountains. This aligns with the large contribution from the Sacramento Mountains, Piñon Creek, and Sacramento River polygons. The Shiloh Draw polygon contains some low recharge fractions that align with the Cornudas Mountains. Since the Cornudas Mountains are igneous intrusions that do not contain chloride, the chloride-to-bromide correction is likely not applicable in this region. However, there is minimal evidence to suggest that the Cornudas Mountain recharge contributes large volumes of recharge to the Salt Basin groundwater. In contrast, the Capitan Reef geologic province in the Texas-wide polygon has high recharge fractions. These high recharge fractions are likely due to Guadalupe Mountain recharge flushing chloride through the system and producing small chloride-to-bromide ratios. Further, Antelope Draw and South Well Draw have low recharge fractions. This suggests a small recharge volume moving along these draws. The lack of chemical evidence suggesting karstification and a small Texas-wide recharge supports the minimal recharge volume. If the CMB polygons were

separated to include these detailed recharge fractions patterns, the chloride-mass-balance recharge estimate would likely average to the same values; increased recharge from the Guadalupe Mountains counters decreased recharge from the rest of the Texas polygon.

The chloride-mass-balance method is dependent upon the chemistry measurements and assumptions of chloride deposition and assumed volume of source waters (rainfall or runoff). Uncertainty due to the chloride deposition parameter is introduced because we have applied a modern chloride deposition rate, yet it is possible that the groundwaters are older than the Holocene. This old water would likely have a different atmospheric depositional rate of chloride due to different climatic variables. An analysis of the corrected radiocarbon ages for the chloride and bromide data points could help differentiate Holocene and Pleistocene waters so that the appropriate chloride depositional rate could be applied to each groundwater sample. The source water assumptions also introduce uncertainty, because we do not know the actual chloride concentration in the runoff that provides the source of recharge in most of the basin. We assume the same as rainfall, which is consistent with rainfall being the source of runoff, but it is possible that as it runs off the landscape it picks up additional chloride that had been deposited on the soil surface. If the chloride concentration of runoff were higher, this would increase our estimate of the fraction of runoff that becomes recharge in these portions of the basin.

The chloride-mass-balance method and PyRANA soil-water-balance model produce independent recharge estimates for the mountainous polygons. Therefore, the two methods can be easily compared. Table 7.1 has the recharge amounts for each mountainous polygon from the chloride-mass-balance method and from the PyRANA estimate, as well as the total amounts for the lowland polygons from the combined chloride-mass-balance and PyRANA method. The primary polygon of each estimate is the same. The primary contributor to the chloride-mass-balance method is the Sacramento Mountains with 22,000 acre-feet per year, and the primary contributor to the PyRANA estimate is the Sacramento Mountains polygon with 5,500 acre-feet per year. According to the chloride-mass-balance method, a total of 27,000 acre-feet per year of recharge comes from the Sacramento and Guadalupe Mountains. PyRANA has 8,000 acre-feet per year attributed to the same aerial extent.

Due to the assumptions going into each method, we are more confident in the recharge estimate from the chloride-mass-balance method. This method is more robust, since it relies on chloride and bromide concentrations of the groundwater samples. PyRANA relies on multiple parameter assumptions in creating a recharge estimate. Nonetheless, there are possible explanations for the chloride-mass-balance method being valid while the PyRANA estimate is an underestimate or for the chloride-mass-balance method being an overestimate while the PyRANA estimate is valid. For the first scenario of PyRANA underestimating recharge, the soil thickness is the determining factor. The relationship between recharge and soil thickness is non-linear, so a small change in soil thickness would cause a large change in estimated recharge. If PyRANA was underestimating recharge,

Watershed	Total PyRANA Recharge	Total Chloride-Mass-Balance Recharge
North Draw	234	234
Piñon Wash	2337	2337
Sacramento River	1054	1054
Big Dog Canyon	192	192
Shiloh Draw	168	168
Eightmile Draw	867	867
Sacramento Mountains	5407	22078
Guadalupe Mountains	2478	4628
Total	12741	31561

Table 7.1: Recharge amounts for each sub-watershed/polygon from chloride-mass-balance method and PyRANA; lowland polygon recharges were found using combination of CMB and PyRANA; PyRANA mountainous recharge = diffuse recharge + mountain focused recharge

the real soils of the Sacramento Mountains and Guadalupe Mountains are truly thinner than the model input. Hence, there could realistically be more recharge than modeled by PyRANA. Alternatively, if the chloride-mass-balance method is an overestimate of recharge, the averaged recharge fraction for the mountainous polygons was unrepresentative. The two groundwater samples from the Sacramento Mountains and the two samples from the Guadalupe Mountains may contain less chloride than surrounding groundwaters. These are small sample sizes. Additional chloride in the representative groundwater would produce lower recharge rates than estimated by the chloride-mass-balance method.

PyRANA is a relatively new recharge estimation method that requires additional refinement. For this study in particular, a regression against elevation and precipitation was necessary to extend the modeled runoff estimates into Texas. If the soil properties are significantly different in Texas relative to the New Mexico training area, this extrapolation may be incorrect. As mentioned previously, there is a non-linear relationship between recharge and soil thickness. The PRISM precipitation data for Texas was a coarser scale than the precipitation data for New Mexico. This and other assumptions should not significantly alter the effectiveness of the PyRANA model, but it nonetheless adds uncertainty into the resulting soil-water-balance.

The culmination of this study is shown in Table 7.2. The previous eleven recharge estimates had a range of 6,000 to 240,000 acre-feet per year. The additional recharge estimate in association with this overall study is from Evenocheck (2021) [1] and used some of the results from this report. The recharge estimates from this study have a range of 13,000 to 32,000 acre-feet per year. While each method has associated uncertainties, these most recent recharge estimates constrain the historic estimates.

Chloride-Mass-Balance + PyRANA total recharge	12741 to 31561
Pre-devlopement steady-state model recharge [1]	60487
Average recharge from transient model [1]	61259

Table 7.2: Resulting recharge amounts from combined chloride-mass-balance and PyRANA and [1]; transient model run from 1948 to 2020; all values are in acre-feet per year

CHAPTER 8

CONCLUSION

The Salt Basin is a semiarid region shared by southeastern New Mexico and western Texas. This basin and the nearly 1,000 residents are at extreme risk of water supply sustainability over the next 30 years [3]. This study aims to constrain historic groundwater recharge estimates to provide a more specific water balance using hydrogeochemical and water balance analyses. Within the overall Salt Basin resource evaluation project funded by the U.S. Bureau of Reclamation, there is also a groundwater model created that results in an independent recharge estimate of 60,000 acre-feet per year for the pre-development steady state model and 61,000 acre-feet per year for the average transient model [1]. The conclusions of this report and Evenocheck (2021) [1] will potentially be utilized to further basin development.

Historic hydrological studies in the Salt Basin have noted the majority of diffuse groundwater recharge originates in the Sacramento Mountains along the northern Salt Basin margin. Secondary focused recharge occurs with monsoonal flooding of ephemeral channels throughout the remainder of the basin. Since the Salt Basin is a hydrologically closed basin, all of the water that enters the Salt Basin through precipitation or groundwater inflow must become groundwater recharge or evapotranspiration. However, the complex geology of the Salt Basin creates a complex groundwater flow system. The primary and tertiary aquifers are carbonate facies with gypsum and halite species, while the secondary aquifer unit is Quaternary alluvium fill. To separate the effects of each geologic province on the flow paths, the groundwater was analyzed based on geologic province and then on a flow path scale rather than a basin-wide scale. The hydrochemical analyses utilizes a historic chemical database from the U.S. Bureau of Geology and Mineral Resources. There is a data gap in the northwestern Salt Basin that coincides with the Fort Bliss-McGregor Range. The remainder of the Salt Basin is populated by data points, with a distinct concentration in and around Dell City, TX.

Within the New Mexico portion of the Salt Basin, the major flow paths within the New Mexico Carbonates geologic province are the Piñon Creek, Cornucopia Draw, Sacramento River, and Shiloh Draw. The Sacramento River, Piñon Creek, and Cornucopia Draw flow paths flow southwards into playas north of Dell City, TX. These three flow paths show dedolomitization as the dominant chemical process. Hence, Dell City is a chemical combination of end dedolomitization waters from the Sacramento River, Piñon Creek, and Cornucopia Draw. Some of

this groundwater may be due to groundwater inflow from the Peñasco Basin to the northeast. However, the possibility of inflow was not explored in this study. Along the New Mexico-Texas state border, Shiloh Draw flows generally eastwards towards Dell City as well. The Cornudas Mountains igneous intrusions alter the Shiloh Draw flow path by mixing in silicious groundwater and redirecting the flow path around the intrusions. This silicious groundwater is theorized, but not proven due to lack of groundwater samples from the Cornudas Mountains themselves.

Western Texas has the coarsely fractured Cretaceous geologic province that complicate the W.Antelope Draw, W.South Well Draw, and E.Antelope Draw and E.South Well Draw flow paths. The eastern flow paths move into the Victorio Peak geologic province, but the chemistry of the Cretaceous is more dominant. There is a minor trend of dedolomitization within the Cretaceous and Victorio Peak geologic province, but there are no overall dominant chemical trends throughout these flow paths. Instead, there are seemingly random concentrations of TDS, radiocarbon, and tritium throughout the area. The fractures offer an explanation for this variability. There is likely a mixing between fracture water and surrounding matrix waters. Waters within the fractures are mostly low TDS and high radiocarbon, suggesting recent recharge. Waters within the matrix are mostly high TDS and low radiocarbon, suggesting old recharge. These old waters in the matrix are similar to waters along the eastern margin of the Salt Basin, i.e., chemically evolved in-place. In support of this idea, the groundwater age of the groundwater should be reflected in the tritium concentrations. Younger waters should have higher tritium concentrations and high radiocarbon activities. However, this trend is not seen in the data of Antelope Draw and South Well Draw. The lack of tritium trend can be explained by stratospheric nuclear weapons testing of the 1950s. Tritium and radiocarbon both peaked in the 1960s and these groundwater samples were collected in the 1980s. The tritium and radiocarbon peaks were not identical and could produce waters with high radiocarbon and low tritium and vice versa. This is likely the scenario that created the two end member waters of Antelope Draw and South Well Draw. The two waters mix as the old, high TDS waters diffuse out of the matrix and into the fractures. It is also possible that the waters are being mixed anthropogenically due to groundwater pumping forcing the two waters together.

The eastern margin of the Salt Basin is comprised of the Capitan Reef geologic province. The limestone in this area also shows a minor dedolomitization trend with brine mixing in from the adjacent Salt Flats to the west. This chemical alteration is the same dedolomitization seen in the New Mexico portion of the Salt Basin, but a paralleled evolutionary trend with lower overall calcium and magnesium.

Dell City, Texas hydrochemistry is affected by irrigation return flow and Salt Flat brines south of Dell City. There is active pivot and flood irrigation in Dell City that stimulates evapotranspiration. Irrigation water that is not lost to ET or incorporated into the crops returns to the groundwater system. However, this cycle of irrigation pumping, evapotranspiration, and irrigation return flow causes

a concentration of salts as the fresh water is evapotranspired or incorporated. NDVI from Google Earth Engine in combination with the Blaney-Criddle method calculated an average amount of 69,000 acre-feet per year is the consumptive use of the Dell City irrigation district. Additionally, Dell City and the Salt Flats show an increase in chloride with a decrease in sulfate nearer to the Salt Flats.

Since the primary aquifers of the Salt Basin are carbonates, radiocarbon corrections were required to calculate a corrected radiocarbon age for the Salt Basin. Carbon data points that could not be corrected were those with an unknown amount of carbonate dissolution. There were minimal carbon data throughout the Salt Basin that was able to be corrected. The Fontes and Garnier approach corrected the radiocarbon initial activities for isotopic exchange. These corrected ages for the New Mexico portion of the Salt Basin aligned in trend with groundwater ages from Sigstedt (2010) [14]. The corrected ages from Sigstedt (2010) [14] are considered to be more accurate due to the detail added to the radiocarbon correction method. For the data points within the Antelope Draw and South Well Draw, an alternative radiocarbon initial activity correction used a simple mixing model between the two end members, designated by respective calcium to sodium ratios. Both corrections resulted in variable corrected radiocarbon ages throughout the southwestern Salt Basin. This further supported the complex, two-waters flow system. Water balance analyses used the chloride-mass-balance method and PyRANA to estimate groundwater recharge for the Salt Basin. The chloride-mass-balance was modified to reflect the amount of chloride introduced to the system from salt mineral dissolution. This modification used the bromide concentration because chloride from rock-water interactions also releases bromide. Using a deep basin brine found in Cloudcroft, NM as the chloride end member and precipitation as the fresh water end member, the chloride-mass-balance created a mixing model curve. Comparing the curve to Salt Basin data, it was possible to determine the amount of mixing between atmospheric chloride and mineral dissolution chloride for delineated sub-watersheds. This mixing ratio was then converted into corrected recharge rate. For the mountainous polygons, the recharge rate was calculated using the precipitation rate, aerial extent of each sub-watershed, and the estimated mixing ratio for each mountainous polygon. For the lowland polygons, the recharge rate was calculated using the runoff volume for each lowland sub-watershed from PyRANA and the estimated mixing ratio for each lowland polygon. The total amount of recharge from the chloride-mass-balance method for the Salt Basin was 32,000 acre-feet per year.

In comparison to the chloride-mass-balance method mountainous recharge estimate, PyRANA used multiple environmental parameters to estimate a soil-water-balance and thus calculate a range of recharge rates for the mountainous polygons. Diffuse recharge was isolated to the high elevations of the Sacramento Mountains along the northern margin of the Salt Basin. Additional recharge was contributed by focused recharge along ephemeral channels that originated in the mountainous polygons. The resulting total amount of recharge from the PyRANA soil-water-balance model for the Salt Basin was 13,000 acre-feet per year. The recharge estimate from the chloride-mass-balance method is assumed to be more accurate due to the simple chemistry inputs and limited assumptions. PyRANA is

sensitive to input parameters and multiple assumptions going into the recharge estimate.

There are eleven primary historic recharge estimates that range from 6,000 to 240,000 acre-feet per year. Most of these previous estimates used different methods to estimate recharge, each with different associated uncertainties. This study used a groundwater flow model [1], chloride-mass-balance, and PyRANA to estimate recharge. While these three methods also have associated uncertainties, the three recharge estimates constrain the previous recharge estimates to 13,000 to 32,000 acre-feet per year (16,000,000-40,000,000 m³/yr.) for the Salt Basin, NM/TX. I recommend that a water-budget plan be implemented to ensure the groundwater pumping from the semiarid Salt Basin is sustainable.

REFERENCES

- [1] Elizabeth Evenocheck. *Assessment of safe aquifer yields within the Salt Basin in New Mexico and Texas*. Thesis, New Mexico Institute of Mining and Technology, 2021.
- [2] L. F. Han, L. N. Plummer, and P. Aggarwal. A graphical method to evaluate predominant geochemical processes occurring in groundwater systems for radiocarbon dating. *Chemical Geology*, 318:88–112, 2012.
- [3] S. B. Roy, L. Chen, E. H. Girvetz, E. P. Maurer, W. B. Mills, and T. M. Grieb. Projecting water withdrawal and supply for future decades in the us under climate change scenarios. *Environmental science and technology*, 46(5):2545–2556, 2012.
- [4] B. A. Stewart. Dryland farming, 2012.
- [5] Andrew James Love, Daniel Worthing, Simon Fulton, Pauline Rousseau-Gueutin, and Samantha De Ritter. *Groundwater recharge, hydrodynamics and hydrochemistry of the Western Great Artesian Basin*. National Water Commission, 2013.
- [6] A. El-Beltagy and M. Madkour. Impact of climate change on arid lands agriculture. *Agriculture and Food Security*, 1(3):3, 2012.
- [7] G. Konapala, A. K. Mishra, Y. Wada, and M. E. Mann. Climate change will affect global water availability through compounding changes in seasonal precipitation and evaporation. *Nature communications*, 11(1):1–10, 2020.
- [8] A. W. Harbaugh, E. R. Banta, M. C. Hill, and M. G McDonald. Modflow-2000, the u. s. geological survey modular ground-water model-user guide to modularization concepts and the ground-water flow process. *Open-file Report*, U.S.Geological Survey(92):134, 2000.
- [9] Steven T Finch. *Hydrogeologic framework of the salt basin and development of three-dimensional ground-water flow model*. John Shomaker and Associates, Incorporated, 2002.
- [10] William Hutchison. Preliminary groundwater flow model, dell city area, hudspeth and culberson counties, texas. report, El Paso Water Utilities Hydrogeology Report, 2008.

- [11] J. W. Shomaker. Revised hydrogeologic framework and updated groundwater-flow model of the salt basin, new mexico. Final report, John Shomaker and Associates, 2010.
- [12] André Blue Ocean Ritchie. *Hydrogeologic Framework and Development of a Three-dimensional Finite Difference Groundwater Flow Model of the Salt Basin, New Mexico and Texas*. Thesis, New Mexico Institute of Mining and Technology, 2011.
- [13] Jeannette Elise Burgen Chapman. Hydrogeochemistry of the unsaturated zone of a salt flat in hudspeth county, texas, 1984.
- [14] Sophia Carmelita Sigstedt. *Environmental tracers in groundwater of the Salt Basin, New Mexico, and implications for water resources*. Thesis, New Mexico Institute of Mining and Technology, 2010.
- [15] Plummer L. N. and Glynn P. D. Radiocarbon dating in groundwater systems, in isotope methods for dating old groundwater. Journal Article STI/PUB/1587, IAEA (International Atomic Energy Agency), 2013.
- [16] Christopher Eastoe and Ryan Rodney. Isotopes as tracers of water origin in and near a regional carbonate aquifer: the southern sacramento mountains, new mexico. *Water*, 6(2):301–323, 2014.
- [17] Sophia C. Sigstedt, Fred M. Phillips, and Andre B. O. Ritchie. Groundwater flow in an ‘underfit’ carbonate aquifer in a semiarid climate: application of environmental tracers to the salt basin, new mexico (usa). *Hydrogeology Journal*, 24(4):841–863, 2016.
- [18] J. C. Fontes and J. M. Garnier. Determination of the initial ^{14}C activity of the total dissolved carbon: A review of the existing models and a new approach. *Water Resources Research*, 1979.
- [19] L. N. Plummer, E. C. Prestemon, and D. L. Parkhurst. An interactive code (netpath) for modeling net geochemical reactions along a flow path, version 2.0. *Water-Resources Investigations Report*, 94:4169, 1994.
- [20] Jeremiah Thomas Morse. *The Hydrogeology of the Sacramento Mountains Using Environmental Tracers*. M.s. thesis, New Mexico Institute of Mining and Technology, 2010.
- [21] L. F. Han and L. N. Plummer. Revision of fontes and garnier’s model for the initial ^{14}C content of dissolved inorganic carbon used in groundwater dating. *Chemical Geology*, 351:105–114, 2013.
- [22] Geoffrey C Rawling and B Talon Newton. Quantity and location of groundwater recharge in the sacramento mountains, south-central new mexico (usa), and their relation to the adjacent roswell artesian basin. *Hydrogeology Journal*, 24:757–786, 2016.

- [23] John B Ashworth. Ground-water resources of the bone spring-victorio peak aquifer in the dell valley area, texas. Report, Texas Water Development Board, 1995.
- [24] DA Chace and RM Roberts. South-central salt basin groundwater characterization. *Field Guide Book for Otero Mesa Area, New Mexico, El Paso Geological Society, El Paso, TX*, pages 47–61, 2004.
- [25] Daniel B. Stephens and Inc. Associates. Salt basin historical playa evaporation study. Report, Daniel B. Stephens and Associates, Inc., 2010b.
- [26] David Ketchum, B Talon Newton, and F Phillips. *High-resolution estimation of groundwater recharge for the entire state of New Mexico using a soil-water-balance model*. Master's thesis, New Mexico Institute of Mining and Technology, 2016.
- [27] Fei Xu. *Estimation of Focused Recharge for New Mexico Using a Soil-water-balance Model: PyRANA*. Thesis, New Mexico Institute of Mining and Technology, 2018.
- [28] F. Xu, D. Cadol, F. M. Phillips, and B. T. Newton. Focused recharge modeling using statistical stochastic approaches. *AGU Fall Meeting Abstracts*, 2018:H13O-1967, 2018.
- [29] Office of the State Engineer. Water rights division: Water rights statutes, rules, regulations and guidelines, 2020.
- [30] Bureau of Reclamation. About us- mission, 2020.
- [31] S. Kelley, M. Fichera, E. Evenocheck, B.A. Eberle, M. Person, D. Cadol, B.T. Newton, S.Timmons, and C. Pokorny. Assessment of water resources in the salt basin region of new mexico and texas: Data summary report. Open-file report, New Mexico Bureau of Geology and Mineral Resources, 2020.
- [32] United States Census Bureau. Quickfacts: Hudspeth county, texas, 2019a.
- [33] United States Census Bureau. Quickfacts: Otero county, new mexico, 2019b.
- [34] Bureau of Land Management. Mcgregor range, 2021.
- [35] Joseph Spencer Gates, WD Stanley, and HD Ackermann. Availability of fresh and slightly saline ground water in the basins of westernmost texas. Report 2331-1258, US Geological Survey, 1980.
- [36] P.D. Nielson and JM Sharp Jr. Tectonic controls on the hydrogeology of the salt basin, trans-pecos texas. *Structure and Tectonics of Trans-Pecos Texas: West Texas Geological Society Publication*, 85-81:231–234, 1985.
- [37] Edward S Angle. Hydrogeology of the salt basin. *Aquifers of West Texas: Texas Water Development Board Report*, 356:232–247, 2001.
- [38] XmACIS2. Single-station: Daily data listing: Dell city 5ssw, tx: 1984-2019, 2021.

- [39] National Oceanic and Atmospheric. Climatology of the united states no. 81, monthly normals of temperature, precipitation and heating and cooling degree days, 1971–2000, 1971-2000.
- [40] James Roger Mayer. *The role of fractures in regional groundwater flow: field evidence and model results from the basin-and-range of Texas and New Mexico*. Thesis, University of Texas at Austin, 1995.
- [41] LJ Bjorklund. Reconnaissance of ground-water conditions in the crow flats area otero county, new mexico: State of new mexico, state engineer office technical rept, 1957.
- [42] United States Environmental Protection. Ecoregions, 2021.
- [43] D.P. Groeneveld and W.M. Baugh. Mapping and estimating evapotranspiration for dell valley, texas. report, El Paso Water Utilities, 2002.
- [44] New Mexico Manufacturing Extension Partnership. New mexico mep agriculture review, 2018.
- [45] L.C. Pray. Geology of the sacramento mountains escarpment: Otero county, new mexico. *State Bureau of Mines and Mineral Resources, New Mexico Institute of Mining and Technology*, Bulletin 35:144, 1961.
- [46] P.T. Hayes. Geology of the guadalupe mountains new mexico. *United States Geological Survey*, 446:73, 1964.
- [47] James R Mayer and John M Sharp Jr. Fracture control of regional ground-water flow in a carbonate aquifer in a semi-arid region. *Geological Society of America Bulletin*, 110(2):269–283, 1998.
- [48] N.C. Newell, J.K. Rigby, A.G. Fischer, A.J. Whiteman, J.E. Hickox, and J.S. Bradley. The permian reef complex of the guadalupe mountains region, texas and new mexico: A study in paleoecology. *Hafner Publishing Company, Inc.*, New York:236, 1972.
- [49] Glenn F Huff and DA Chace. Knowledge and understanding of the hydrogeology of the salt basin in south-central new mexico and future study needs. Report, United States Geological Survey, Office of the State Engineer Interstate Stream Commission, Sandia National Laboratories, 2006.
- [50] P.H. Masson. Age of igneous rocks at pump station hills, hudspeth county, texas. *Bulletin of the American Association of Petroleum Geologists*, 40:501–518, 1956.
- [51] D.S. Barker. Cenozoic igneous rocks, sierra blanca area, texas. *New Mexico Geological Society Guidebook, Trans-Pecos Region*, 31st Field Conference:219–223, 1977.

- [52] C.J. Nutt, J.M. O'Neill, M.D. Kleinkopf, D.P. Klein, W.R. Miller, B.D. Rodrquez, and V.T. McLemore. Geology and mineral resources of the cornudas mountains, new mexico. *Open-file Report*, U.S.Geological Survey(97-282):46, 1997.
- [53] W.E. King and V.M. Harder. Oil and gas potential of the tularosa basin–otero platform–salt basin graben area, new mexico and texas. *Circular*, 198:48, 1985.
- [54] CW Kreitler, JA Raney, R Nativ, EW Collins, WF Mullican, TC Gustavson, and CD Henry. Siting a low-level radioactive waste disposal facility in texas, volume four-geologic and hydrologic investigations of state of texas and university lands: The university of texas at austin, bureau of economic geology, report prepared for the texas low-level radioactive waste disposal authority under interagency contract no. IAC (86-87), 1986.
- [55] G.J. Wasserburg, G.W. Wetherill, L.T. Siler, and P.T. Flawn. A study of the ages of the precambrian of texas. *Journal of Geophysical Research*, 67(10):4021–4047, 1962.
- [56] D.W. Boyd. Permian sedimentary facies, central guadalupe mountains, new mexico. *State Bureau of Mines and Mineral Resources*, New Mexico Institute of Mining and Technology, 1958.
- [57] V.C. Kelley. Geology of the pecos country, southeastern new mexico. *New Mexico Institute of Mining and Technology*, Memoir(24):88, 1971.
- [58] G.M Friedman. Occurrence and origin of quaternary dolomite of salt flat, west texas. *Journal of Sedimentary Research*, 36(1):263–267, 1966.
- [59] F.M. Byod and C.W. Kreitler. Hydrogeology of a gypsum playa, northern salt basin,texas. *Bureau of Economic Geology Report of Investigations*, 158:37, 1986.
- [60] National Park Service. The el paso salt war, 2015.
- [61] Anne Celeste Tillary. *Estimates of mean-annual streamflow and flow loss for ephemeral channels in the Salt Basin, southeastern New Mexico*, 2009. US Department of the Interior, US Geological Survey, 2011.
- [62] S.J. Mazzullo. Permian stratigraphy and facies, permian basin (texas-new mexico) and adjoining areas in the midcontinent united states. *Sedimentary Basins and Economic Resources*,Spring-Verlag, N.Y., pages 41–60, 1995.
- [63] Philip B King. Geology of the southern guadalupe mountains, texas. *U.S. Geological Survey Professional Paper*, 215:183, 1948.
- [64] Lisa Karen Goetz. Salt basin graben: A basin and range right-lateral transtensional fault zone, some speculations. *Structure and Tectonics of Trans-Pecos Texas: West Texas Geological Society Publication*, pages 165–168, 1985.
- [65] Daniel B. Stephens and Inc. Associates. Recharge modeling study, salt basin of southeastern new mexico. Report, Daniel B. Stephens and Associates, Inc., 2010a.

- [66] BT Newton, GC Rawling, SS Timmons, L Land, PS Johnson, TJ Kludt, and JM Timmons. Sacramento mountains hydrogeology study. *NM Bur Geol Min Resour Open-File Rep*, 543, 2012.
- [67] John M Sharp Jr. Regional ground-water systems in northern trans-pecos texas. *Structure and Stratigraphy of Trans-Pecos Texas: El Paso to Guadalupe Mountains and Big Bend July 20–29, 1989*, 317:123–130, 1989.
- [68] United States Geological Survey. Federal standards and procedures for the national watershed boundary dataset (wbd), 2013.
- [69] Federal User Community. Watershed boundaries, 2021.
- [70] Ralph A Scalapino. *Development of ground water for irrigation in the Dell City area, Hudspeth County, Texas*. Texas Board of Water Engineers, 1950.
- [71] G. B. Maxey and T. E. Eakin. , ground water in wite river valley, white pine, nye, and lincoln counties nevada. Journal article, Nevada State Engineer's Office Water Resources Bulletin, 1949.
- [72] D. B. Stephens and T. Umstot. Development and evaluation of the maxey-eakin recharge method. *Hydrogeology Journal*, 27(2):747–760, 2019.
- [73] CJ Eastoe and BJ Hibbs. Stable and radiogenic isotope evidence relating to regional groundwater flow ssystems originating in the high sacramento mountains, new mexico. In *AGU Fall Meeting Abstracts*, volume 2005, pages H33G–04, 2005.
- [74] William Roger Miller. Environmental geochemistry and processes controlling water chemistry, cornudas mountains, new mexico. Report 2331-1258, US Geological Survey, 1997.
- [75] William Back, Bruce B Hanshaw, L Niel Plummer, Perry H Rahn, Craig T Rightmire, and Meyer Rubin. Process and rate of dedolomitization: mass transfer and 14c dating in a regional carbonate aquifer. *Geological Society of America Bulletin*, 94(12):1415–1429, 1983.
- [76] S. Jasechko. Global isotope hydrogeology- review. *Review of Geophysics*, 57, 2019.
- [77] F. M. Phillips and M. C. Castro. Groundwater dating and residence-time measurements. *Treatise on geochemistry*, 5:605, 2003.
- [78] N. Gorelick, M. Hancher, M. Dixon, S. Ilyushchenko, D. Thau, and R. Moore. Google earth engine: Planetary-scale geospatial analysis for everyone. *Remote Sensing of Environment*, 202:18–27, 2017.
- [79] United States Geological Survey. Landsat missions, 2021a.
- [80] United States Geological Survey. Landsat mission timelines, 2021b.

- [81] United States Geological Survey. What is landsat and etm+ slc-off data?, 2021c.
- [82] Food and Agriculture Organization. Chapter 3: Crop water needs, 1954.
- [83] J. G. Loftfield. The behavior of stomata. *Carnegie Institution of Washingtons*, 1921.
- [84] Warren W Wood. Use and misuse of the chloride-mass balance method in estimating ground water recharge. *Ground Water*, 37:2–3, 1999.
- [85] C. Zhu, J. R. Winterle, and E. I. Love. Late pleistocene and holocene ground-water recharge from the chloride mass balance method and chlorine-36 data. *Water Resources Research*, 39(7), 2003.
- [86] P.M. ReVelle. *Evapotranspiration in mountain terrain- applying topographic-based energy constraints to evaluate the distribution of water-fluxes and effects of vegetation over change*. Thesis, New Mexico Institute of Mining and Technology, 2017.
- [87] Richard G Allen, Luis S Pereira, D Raes, and Martin Smith. Fao irrigation and drainage paper no. 56. *Rome: Food and Agriculture Organization of the United Nations*, 56(97):e156, 1998.
- [88] R Core Team. R: A language and environment for statistical computing. r foundation for statistical computing, 2020.

APPENDIX A

HYDROCHEMISTRY DATABASE

A.1 Chemistry Data from the Assessment of Water Resources in the Salt Basin Region of New Mexico and Texas Data Summary Report (Open-File Report 608)

APPENDIX B

GOOGLE EARTH ENGINE CODE FOR NDVI ACTIVE IRRIGATION ESTIMATE

B.1 Appendix B code is available electronically under supplementary material

APPENDIX C

BLANEY-CRIDDLE TEMPERATURE AND REFERENCE CROP ET

C.1 Appendix C table is available electronically under supplementary material

APPENDIX D

PERMISSIONS

List of borrowed figures:

Figure 1.2, Figure 1.3, Figure 1.4: Kelley et al., 2020 [31]– public domain

Figure 1.5, Figure 1.6, Figure 1.7: Sigstedt, 2010 [14]– New Mexico Tech Thesis

Figure 1.10, Figure 4.1a: Ritchie, 2011 [12]– New Mexico Tech Thesis

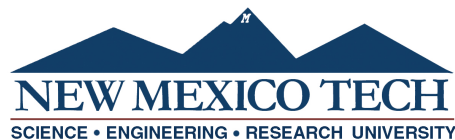
Figure 2.2: Tillery, 2011 [61]– public domain

EVALUATION OF GROUNDWATER RECHARGE IN THE
SALT BASIN, NM/TX

by

Beth Ann Michelle Eberle

Permission to make digital or hard copies of all or part of this work for personal or classroom use is granted without fee provided that copies are not made or distributed for profit or commercial advantage and that copies bear this notice and the full citation on the last page. To copy otherwise, to republish, to post on servers or to redistribute to lists, requires prior specific permission and may require a fee.



ProQuest Number: 28648041

INFORMATION TO ALL USERS

The quality and completeness of this reproduction is dependent on the quality
and completeness of the copy made available to ProQuest.



Distributed by ProQuest LLC (2022).

Copyright of the Dissertation is held by the Author unless otherwise noted.

This work may be used in accordance with the terms of the Creative Commons license
or other rights statement, as indicated in the copyright statement or in the metadata
associated with this work. Unless otherwise specified in the copyright statement
or the metadata, all rights are reserved by the copyright holder.

This work is protected against unauthorized copying under Title 17,
United States Code and other applicable copyright laws.

Microform Edition where available © ProQuest LLC. No reproduction or digitization
of the Microform Edition is authorized without permission of ProQuest LLC.

ProQuest LLC
789 East Eisenhower Parkway
P.O. Box 1346
Ann Arbor, MI 48106 - 1346 USA